Institute of Space and Aeronautical Science, University of Tokyo
Report No. 495, June 1973

The Gyro-Plasma Probe onboard the REXS-DENPA Satellite

(Technical Report of IPS Research Group)

By

Masaki EJIRI*, Hiroshi OYA**, Takehiko ASO**, Kozo MORITA**,
Tatsuzo OBAYASHI*, Shinji URIMOTO*** and Hiroyuki YAMAKI***

Summary: The swept frequency impedance probe IPS, which is designed to measure ionospheric plasma parameters, has been installed on the REXS-DENPA satellite (1972-064A). The IPS consists of an impedance measuring equipment, automatic sample-detection sub-systems and 2 m antenna as a sensor immersed in space plasma. The impedance measuring equipment is known as the gyroplasma probe. Various plasma resonance frequencies are detected and antenna impedance values at several frequencies are measured. Those digitalized data are fed to PCM telemetry through a data sampling system.

The pre-flight operation and plasma-simulation tests were found to be satisfactory; they provided, also, the calibration data on equipment characteristics at different temperature values that can be realized in the flight condition.

The REXS was successfully put into the orbit on August 19, 1972. Measurements of ionospheric plasma parameters, such as electron density and ion composition were made in the altitude range from 240 km to 6570 km over the equatorial orbit (inclination 31°). Observational data have been analysed applying the data handling method aided by digital computers.

Preliminary results obtained for a period of three-days observation are summarized for following items; i) electron density profiles in the topside ionosphere over the sub-tropical latitudes, ii) mean ion composition in the topside ionosphere and iii) the antenna potential control effect due to photomission from metalic antenna surface.

CONTENTS

---

* Institute of Space and Aeronautical Science, University of Tokyo.
** Ionosphere Research Laboratory, Kyoto University,
*** Meguro Laboratory, Meisei Electric Co., Tokyo.
Kozo Morita is now at Nippon Telegraph and Telephone Public Co., Tokyo.

I. INTRODUCTION

On August 19, 1972, REXS (designated as DENPA after injection into the orbit) was launched to observe space plasma parameters, VLF plasma waves and geomagnetic field in the orbit with the perigee of 240 km, the apogee of 6570 km, and inclination of 31°. In the spacecraft (77 cm diagnoal length and 68 cm tall, with three 2 m antennas, see Fig. 1), the "Impedance Probe for Satellite Observation (IPS)" has been installed together with other payloads that are planned to make an integrated observation for plasma structure and wave-particle interaction phenomena in the ionosphere and the lower part of the magnetosphere. These equipments include the electron temperature probe (TEL), the electromagnetic and plasma wave receiver (PWP), the flux-gate magnetometer (MGS), the cyclotron instability experiment (CIE) and the electron beam analyser (EBA).

The initial operation of all equipments was successful following the programmed procedure except the EBA. Unfortunately, the EBA, which was switched on the

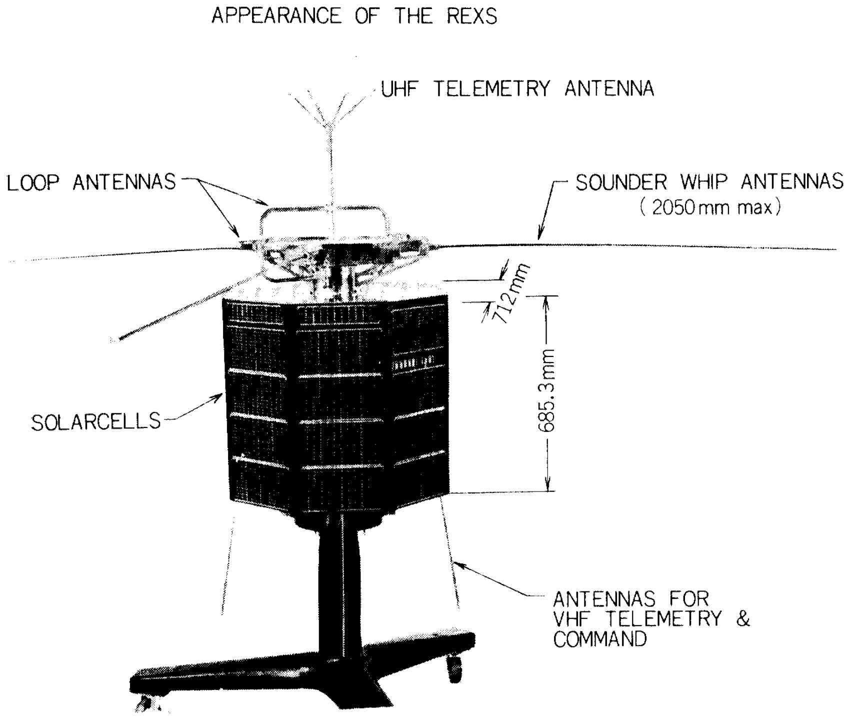

FIG. 1. Spacecraft REXS.

third day after the injection, had a fatal accident of electrical discharges. Consequently, the encoder of the spacecraft ceased normal operation. During the period of three days prior to this accident, however, the complete functioning of IPS produced excellent data on the electron density, electron temperature and ion composition of the topside ionosphere.

In the present report, the technical information to construct the IPS system for the REXS satellite and the preliminary observational results are given. The IPS has been developed from the experiences of the past rocket experiments. Section II gives a brief historical reviw on the development of the gyroplasma probe. The design of IPS circuit and interface problems between the gyro-plasma probe and the PCM telemetry system are described in Section III. Operational characteristics in pre-launching tests and the data handling method are given in Sections IV and V, and the preliminary results of observation in Section VI.

II. HISTORICAL REVIEW OF GYRO-PLASMA PROBE

Since the first successful gyro-plasma probe experiment performed at 1110 JST on 23 July, 1965 [2], a number of valuable results have been obtained in measuring the ionospheric electron density profie through rocket experiments. New data on ionospheric plasma has been acquired with a high accuracy of measurement within an error of a few percent.

The gyro-plasma probe is a kind of the RF impedance probe in which the frequency scanning technique is employed. The unique point is its performance of distinct identification of the plasma resonances based on rigorous theoretical treatment and careful techniques of measuring the frequency characteristics of the probe immersed in the space plasma. This has already been discussed, compared with the other type of RF impedance probe and the DC probe [*3*]. The main features of gyro-plasma probe experiments have also been published in several papers [*4–6*]. The most significant features of the gyro-plasma probe are: i) the system in measuring the amplitude and phase shift angle of the probe admittance over a wide frequency range, ii) the circuit designed to reduce the error of measurement, especially the bridge circuit to detect the frequency characteristics of the probe admittance. A brief review will also be given, here, of experimental results obtained by this gyro-plasma probe.

II-1 Gyro-plasma Probe System

1.1 Total system

The gyro-plasma probe is designed to measure the frequency characteristics of the absolute value and phase shift angle of the probe admittance. The overall layout of the system is illustrated in Fig. 2.

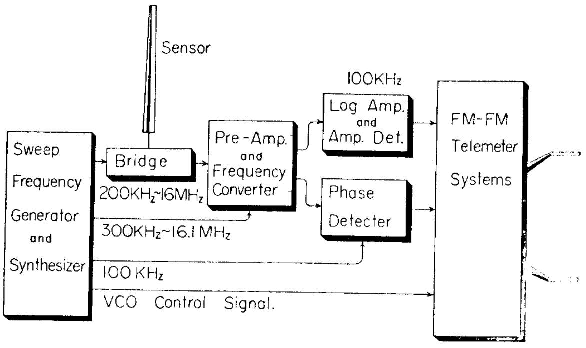

FIG. 2. Block diagram of gyro-plasma probe system.

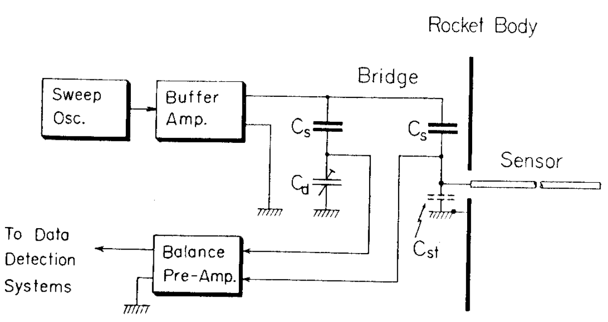

FIG. 3. Bridge circuit to measure the disturbance-free admittance value of the probe.

The source signal for the frequency characteristic measurement is fed by a sweep-frequency generator. The frequency is swept from 200 kHz to 16 MHz at the repetition rate of 1–2 c/s. A large range of this sweeping frequency is gained by mixing the VCO signal with a fixed frequency signal of 70,000 MHz, generated by a quartz stabilized oscillator; the frequency range of VCO is, in this case, 54,000–69,800 MHz (see Fig. 4).

This source signal which is swept in a range from 200 kHz to 16 MHz is impressed on the bridge circuit through a buffer amplifier. The bridge circuit consists of three condensers and the probe immersed in the space plasma. The admittance change of the probe in the space plasma is detected by a balanced pre-amplifier whose input impedance is sufficiently high not to disturb the admittance measurement of the probe in the birdge circuit.

Through the balanced pre-amplifier, whose operational frequency range is wide enough to cover 200 kHz to 16 MHz, the measuring signal is transformed into a fixed frequency signal converter not to be subjected to the complicated disturbances of the logarithmic amplifier and the phase detection circuits. After this process, the signal is divided into two channels, the channel for the absolute value detection and that for the phase detection. Finally, the absolute and the phase values of the probe admittance are expressed by quasi-DC signals in a level range of 0–5 V which are transmitted by an FM-FM telemetry system.

1.2 Bridge circuit

It is important to eliminate any disturbance due to stray capacity in sensor circuits for the measurement of the probe admittance, especially for an accurate detection of the resonance frequencies. A bridge circuit is used to eliminate this effect of stray capacity, as illustrated in Fig. 3. One can adjust the value of a dummy capacity C_d to that of the stray capacity C_{st} under the installation condition in the rocket body, so that the unbalance in the bridge circuit is purely caused by the probe admittance. The output signal intensity e_0 is given for the capacitance value given in Fig. 3 as

$$e_0=\frac{C_sC(\omega)}{(C_d+C_s)(C(\omega)+C_s)}e_i, \tag{1.1}$$

where e_i is the level of the input signal; $C(\omega)$ is the equivalent probe capacitance which is defined, for a probe admittance $A(\omega)$, as

$$C(\omega)=A(\omega)/j\omega, \tag{1.2}$$

where $j\equiv\sqrt{-1}$. For $C_s\gg C_d$ and $C_s\gg C(\omega)$, this output signal is directly proportional to the equivalent capacity as

$$e_0=(C(\omega)/C_3)e_i. \tag{1.3}$$

These characteristics were investigated carefully in a pre-launch test; no errors were found in measuring the resonance frequencies which give $C(\omega)=0$ (see Appendix A).

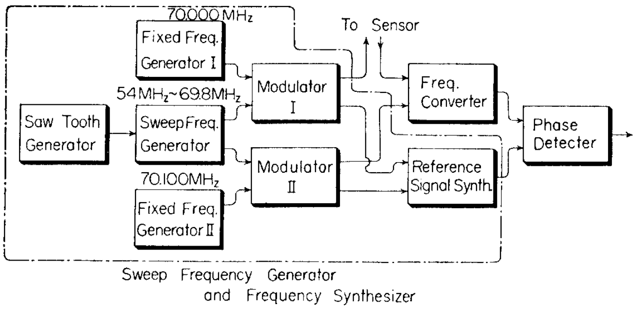

FIG. 4. Signal generator and frequency synthesizer for phase detection of the probe.

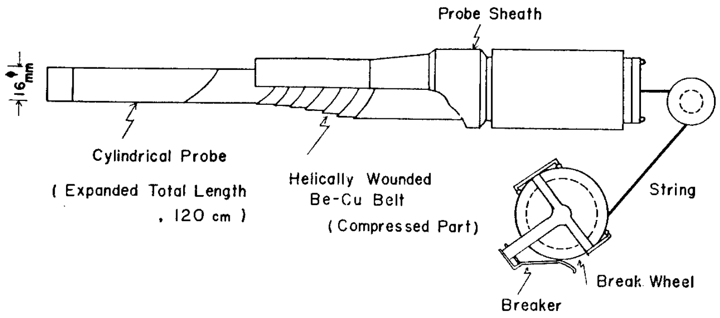

FIG. 5. Mechanism of an extendable helically wounded belt type cylindrical probe.

1.3 Amplitude and phase detection circuits

The detection of the signal amplitude which is proportional to the absolute value of eq. (1.3), is made after compressing the signal level within dynamic range of 60 dB so as to display it as a quasi-DC signal with a range of 0–5 V.

The detection of the phase-angle shift of the probe admittance is performed by transforming the signal at a fixed frequency into a periodic pulse train; the phase shift of these pulses is measured with respect to the reference pulse train through an AND-gate. The phase detection system is carefully designed so as not to be disturbed by any spontaneous phase fluctuation in the signal generators. To obtain a reference signal for the phase detection system, a special arrangement of the frequency synthesizing system is used as illustrated in Fig. 4. No phase shift except for that due to probe admittance is anticipated between the reference and the measuring signals, since the input signals to the frequency converter and the reference signal synthesizer are fed by the same signals except for the phase shifting elements in the sensor.

II-2 Sensors

Two kinds of sensors were used in the space plasma experiments onboard the ionospheric sounding rocket. The sensors used are: (i) a short cylindrical bar, and (ii) a sphere probe placed at the top of the boom [2]. It is essential for a

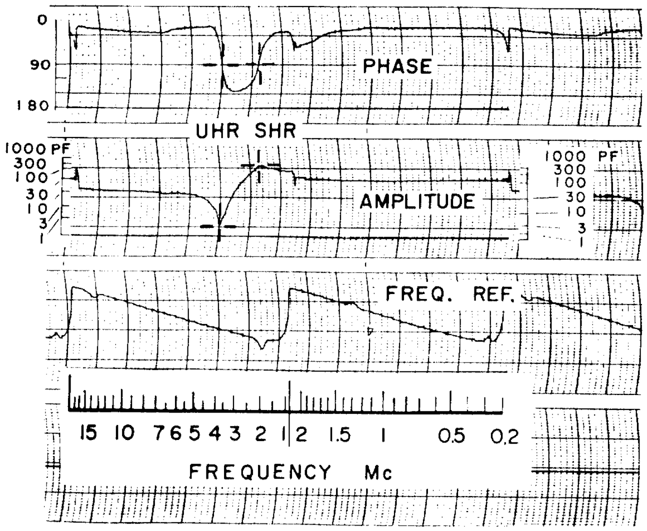

FIG. 6-a

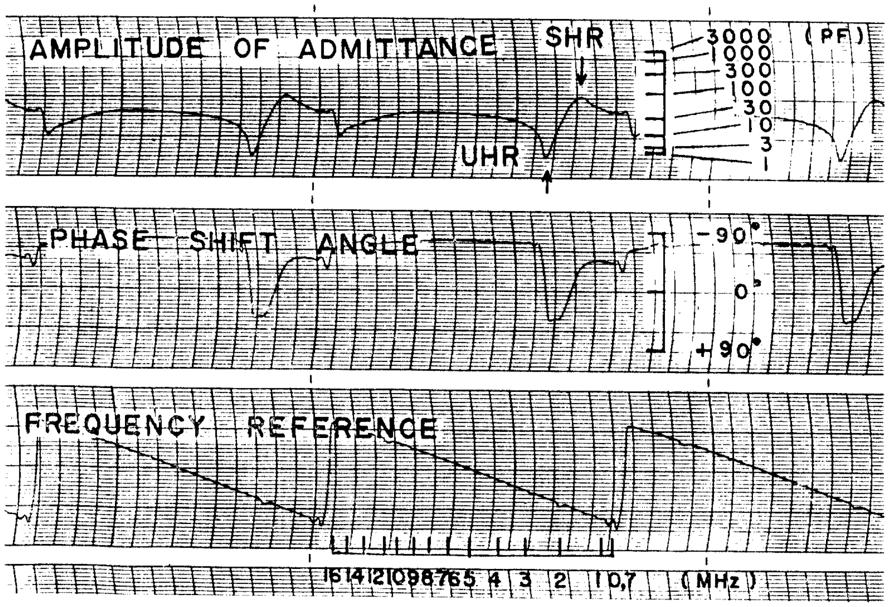

FIG. 6-b

FIG. 6. Sample records of admittance measurement ((a) Oya and Obayashi [4], and (b) Ejiri and Obayashi [50]).

successful experiment to obtain good performance in the extension mechanism of the sensor.

The short cylinder-type probe consists of many short concentric cylinder segments. The expansion of the sensor is made by releasing the compressed steel spring which is placed along the common axis of these cylinder segments. The other type of sensor consists of helically wound metal which is an elastic belt made of Be-Cu alloy. This helically wound metal belt is also compressed into the rocket body (see Fig. 5) and released to extend to a cylinder form probe for observation.

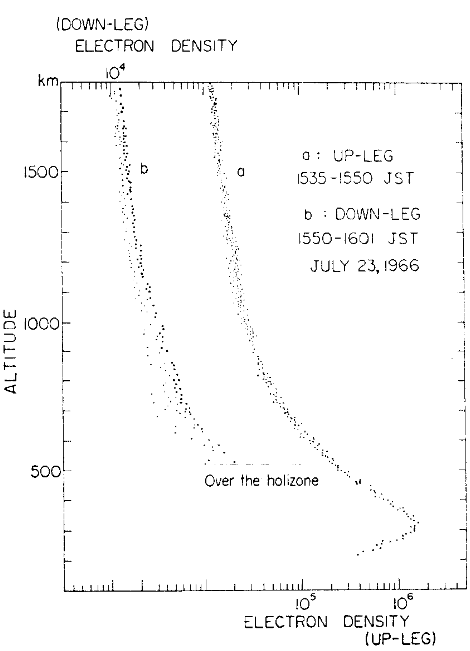

FIG. 7. Electron density profile in the topside ionoshere [4].

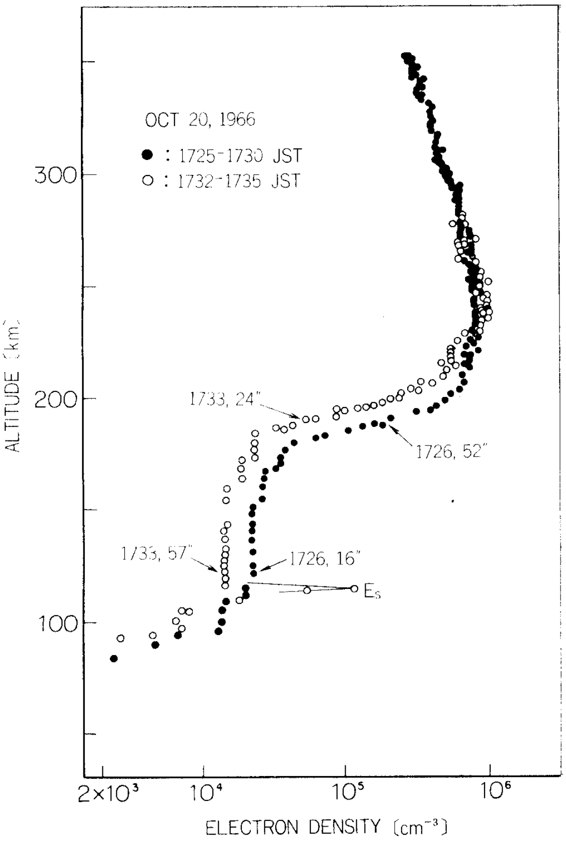

FIG. 8. Ionospheric electron density profile at sun-set (200 km level) (Oya and Obayashi [16]).

These expansion mechanisms of the sensor are very reliable and no failure in performance has occurred in the past experiments.

II-3 Review of Experimental Results

3.1 Displayed data

In Fig. 6, an example of the measured records [*3*] is reproduced; the data was obtained in the experiment of the L-3H-2 (a) and the K-8-15 (b) rockets launched in 1966 and 1969. Frequency characteristics of the equivalent capacity $C(\omega)$ is displayed for both the amplitude and phase shift angle. From this data the identification of plasma resonances is possible aided by the result obtained from theoretical investigation.

The upper hybrid resonance is indicated by the symbol UHR in Fig. 6. This displayed form of the frequency characteristics around UHR is identical with the parallel resource of an electric circuit in the point that the admittance varies from a cpaacitive value to an inductive with decreasing frequency; the amplitude of the admittance shows a minimum at the resonance point. The resonance indicated by the symbol SHR is the sheath resonance [*7–11*]. This is identical with the series

TABLE. 1. List of rocket experiments with the gyro-plasma probe.

No.	Rocket	Date	Launching Time (JST)	Altitude Range (km)	Remarks
1	K-9M-13	July 27, 1965	1210	85–315	500kHz–10MHz
2	K-9M-14	Oct. 4, 1965	1200	80–295	Fixed 5.01MHz, 1.15MHz
3	L-3H-2	July 23, 1966	1535	220–1800	200kHz–16MHz
4	K-9M-20	Oct. 20, 1966	1725	80–353	300kHz–10MHz
5	K-9M-21	Dec. 5, 1966	1100	90–330	300kHz–16MHz
6	K-9M-25	Jan. 8, 1969	1110	85–180	300kHz–12MHz
7	K-8-15	Jan. 9, 1969	1640	90–190	700kHz–17MHz
8	K-9M-24	Jan. 19, 1969	2100	95–340	1MHz– 7MHz
9	K-9M-27	Aug. 7, 1969	2115	200–340	500kHz–10MHz
10	L-3H-6	Jan. 21, 1970	1110	350–1850	200kHz–16MHz
11	L-3H-5	Sept. 19, 1970	2030	300–2050	200kHz–10MHz
12	S-210-6	Jan. 21, 1972	1124	75–110	200kHz–14MHz
13	K-9M-35	Jan. 23, 1972	2022	180–340	300kHz–14MHz
14	K-9M-38	Feb. 22, 1972	1500	95–360	200kHz–14MHz

reasonance of an electric circuit; the admittance variation versus the swept frequency reveals the so-called duality corresponding to the case of UHR.

Gyro resonance is not observed due to the existence of the ion sheath resign. The inhibition of the existence of this gyro resonance is due mainly to the absence of electrons in the ion sheath region, being repelled by the retarding potential around the probe [*11*].

It has been predicted theoretically from the Balmain's formula [*12*] that there is another branch of the plasma resonance called the modified plasma resonance [*13*]. This has been confirmed by this gyroplasma probe experiment [*14, 15*]. Thus, the gyro-plasma probe is excellent in that one is able to obtain precise identification of all existing plasma resonances caused by the relevant nearfield around the probe in the high frequency range.

The upper hybrid resonance at the frequency $\sqrt{(f_p^2+f_H^2)}$, where f_p and f_H are the plasma-resonance and the gyro-resonance frequencies, respectively, is used for the measurement of electron density; it is confirmed that there are the following merits: (i) there are no disturbances caused by the ion sheath which exists around the probe; (ii) UHR frequency can be determined independently to the attitude of the probe with respect to the pervading magnetic field and (iii) UHR frequency is also independent to the shape of the probe.

3.2 *Measured electron density profiles*

From the measured upper hybrid resonance frequency, the ionospheric electron density was evaluated within an error of ±3%. A brief review of the measured electron density profiles in the past experiments [*4–6, 13, 19*] is given here. Several eamples are illustrated in Figs. 7–9; the data plotted in these figures are repro-

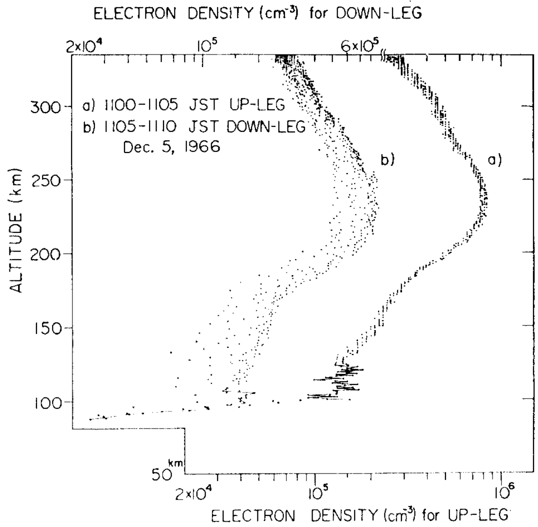

FIG. 9. Ionospheric electron density profile measured by a very short cylinder probe, a remarkable wake effect is evident in the descending path.

duced frrom the results of rocket experiments given in Table 1.

These results contributed much for the study of the ionospheric plasma, as follows: (i) direct confirmation of the diffusive equilibrium distribution of the electron density at the topside of the ionosphere [*4*, *19*], (ii) direct evaluation of the recombination coefficient in the F_1 layer of the ionosphere, yielding the value of 3.4×10^{-8} cm^3/sec [*5*], (iii) detection of the irregular-type sporadic *E* [*13*], which is found theoretically to be caused by a drift dissipative instability [*17*, *18*], (iv) detailed investiigation of the electron density around the moving vehicle, that is, detection of the wake disturbances and of the undisturbed ambient plasma region.

III. INSTRUMENTATION OF GYRO-PLASMA PROBE

III-1 Design Concept of Gyro-plasma Probe

The gyro-plasma probe for the REXS satellite (IPS) is designed to measure the antenna impedance characteristics as a function of frequency over a wide range which includes various plasma resonances. Since the observed data are transmitted through the time-sharing PCM tlemetry, an onboard data processing system is required to provide all digital information of measured plasma resonances and antenna impedance values.

A block diagram of the general concept of IPS is shown in Fig. 10. The system consists of the high frequency gyro-plasma probe (IPH), the low frequency gyro-plasma probe (IPL), the frequency calibration circuits (IPS CAL), the timing control signal generator including the antenna switching circuit, and the data processing system.

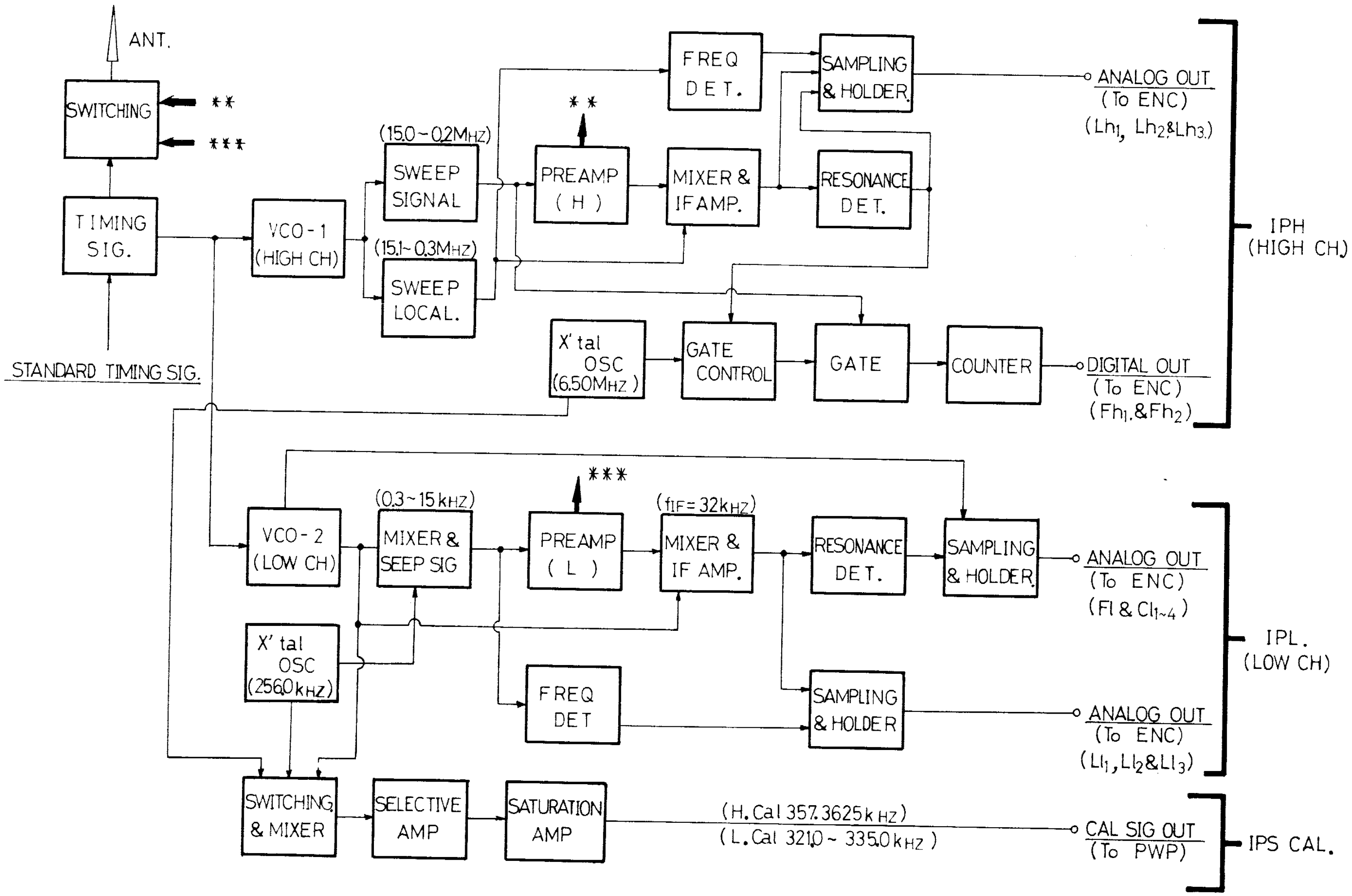

FIG. 10. Block diagram of IPS instrument.

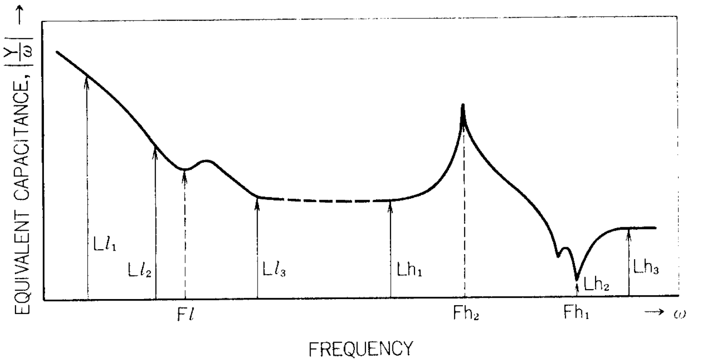

FIG. 11. Schematic illustration of admittance-frequency characteristics. Frequency range 1 kHz-15 MHz, equivalent capacitance= admittance/frequency.

TABLE. 2. Observation items and abbreviations.

	Abbreviation	Items
IPH	Fh_1	Upper Hybrid Resonance Frequency
	Fh_2	Sheath Resonance Frequency
	Lh_1	Equivalent Capacity at 300 kHz
	Lh_2	Equivalent Capacity at UHR
	Lh_3	Equivalent Capacity at 13 MHz
IPL	Fl	Lower Hybrid Resonance Frequency
	$Cl_{1\sim4}$	Frequency Calibration
	Ll_1	Equivalent Capacity at 1.25 kHz
	Ll_2	Equivalent Capacity at 3.80 kHz
	Ll_3	Equivalent Capacity at 6.65 kHz

The equivalent capacitance is the absolute value of the representative antenna admittance devided by the operating angular frequency.

The swept frequency ranges are 0.2–15 MHz for IPH channel and 0.3–15 kHz for IPL channel. The upper hybrid resonance frequency (f_{UHR}) and the sheath resonance frequency (f_{SHR}), and antenna admittance values are detected and stored in the IPH channel. The lower hybrid resonance frequency (f_{LHR}) is detected and the antenna admittance values are sampled and stored in the IPL channel. The measuring items are summarized in Table 2. For the reference, an analog form of the admittance-frequency curve of an antenna in a plasma is shown in Fig. 11.

Both the IPH and IPL systems consist of *r.f.* swept signal generator, pre-amplifier with capacitance bridge, IF amplifier, and data processing circuits. Utilizing the frequency spectrum analyser technique, the output signal from the capacitance bridge is amplified and mixed with local sweep signal to form IF amplitude modulated signal, and it is compressed by the logarithmic operational amplifier. As for the resonance frequency detection of IPH, the triggering signal to the gate control circuit is fed by the monostable multi-vibrator after resonance identification through the differentiator and level comparator.

To check the standard frequency, the IPS CAL section is provided. The IPS CAL section consists of the switching circuit, mixer, selective amplifier and saturation amplifier.

The timing signal generator produces the various time-sequence control pulses for the data processor and switching circuits using the standard timing pulse out of the timing encoder instrument of the spacecraft.

To design IPS circuits, as a satellite-borne instrument, following constraints should be observed.

i) To reduce hard-ware components and their weight.

ii) To minimize the power consumption; circuits are operated in time-sequencially by switching the power source, except for the common parts where the high stability is required.

iii) To secure the reliability of operations in a thermal vacuum environment and in the radiation hassard; individual instrument parts are tested under simulated space conditions before the integration of circuits.

III-2 PCM Telemetry System

The data transmission has been made through two telemetry channels at 136.695 MHz (VHF TM) and 400.500 MHz (UHF TM) with PCM/DPSK/AM. FM/AM mode (IRIG BAND #10) is also used in UHF telemetry channel, the operation of this channel being selected by the command item "SIG. CHANGE-2". The observed data has been stored in the onboard data recorder which is capable to store the data (recording time of 133 min and playback time of 7 min). The outline of the signal flow is shown in Fig. 12. The telemetry signal is 768 Hz square wave phase shift-keyed by a 64 bps split-phase mark code stream in a real-time mode, and 3648 Hz square wave phase-shift-keyed by a 1216 bps split-phase-mark code stream in a playback mode.

In the present PCM coding, one sampling datum is quantized by 8 bits pulses which correspond to decimal counts of 255, and the bit rate of this data transmission system in a normal sampling mode is 64 bits. One frame of the telemetry unit consists of 32 words, that is transmitted in 4 sec; that is defined as one mode. In the REXS satellite system the mode changes in cyclic form; a period of one rotation of these modes is 32 sec that contains 8 frames.

The telemetry mode format of the time-sequential words is shown in Fig. 13, in which the data obtained with the gyro-plasma probe are allocated in mode II_1 (IPH) and mode II_2 (IPL). SY is a frame synchronous pattern, and MZ, $MH_{1\sim 2}$, and HK are the axial component, two horizontal components of geomagnetic field, and the house keeping data, respectively. F_0 is used as a frame counter to identify the frame mode from I to IV.

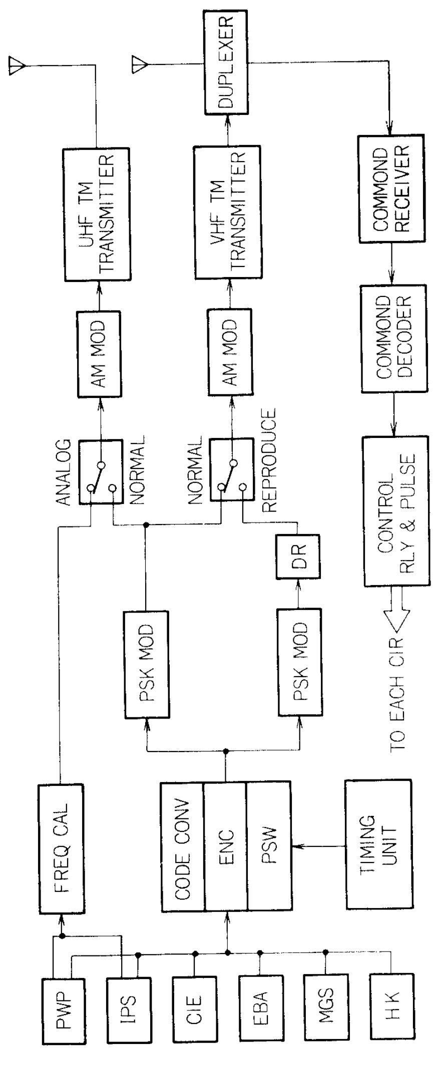

FIG. 12. Signal flow of science payloads.

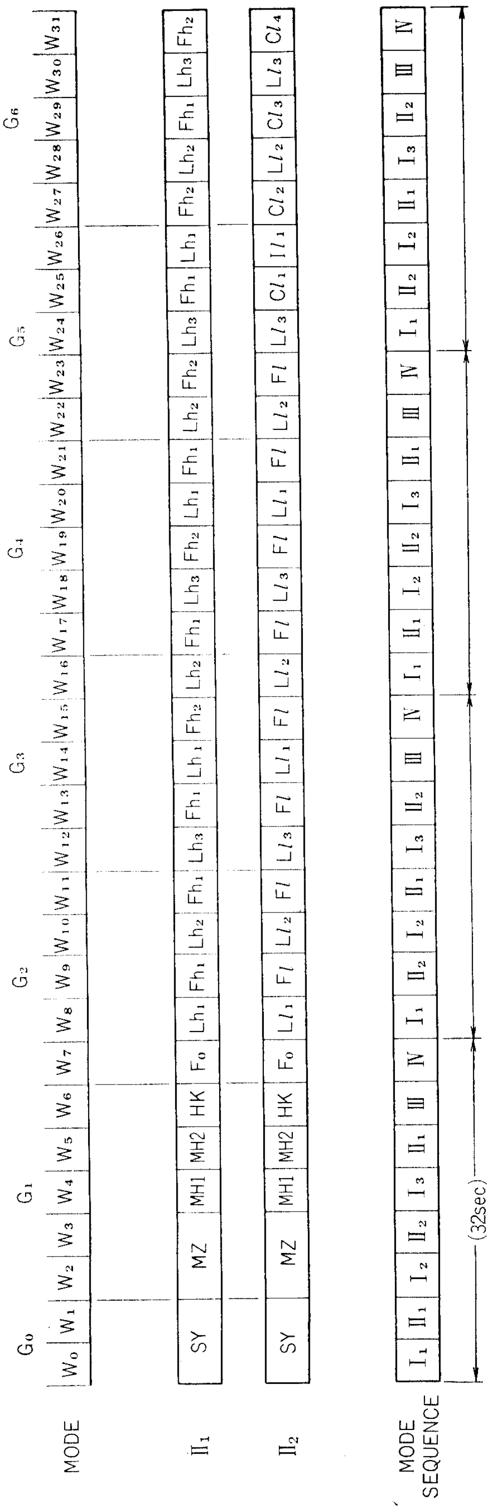

FIG. 13. Telemetry mode format; II_1 for IPH and II_2 for IPL.

III-3 High Frequency Gyro-plasma Probe

The detailed circuit designs and construction for the high frequency Gyro-plasma Probe (IPH) are given. The swept frequency signal is generated by the voltage controlled oscillator, buffer amplifiers, crystal oscillators, mixers, and video-amplifiers with low pass filters. The antenna impedance is measured by the capacitance bridge with pre-amplifier, the output signal from which is converted to IF signal (100 kHz) and detected through the IF amplifier and the linear detector. The frequency and resonance detectors for identification of the time at 300 kHz, 13 MHz, f_{UHR}, and f_{SHR} associated with logarithmic and linear amplifiers, sampling-hold circuit and data processing circuits are presented. The gate width control circuit with a crystal oscillator and 8-bit binary counter for Fh_1 and Fh_2 are also explained.

3.1 Saw-tooth generator and voltage controlled oscillator (VCO-1)

The saw-tooth generator used in this instrument is a kind of boot-strap circuit as shown in Fig. 14. The output swept voltage to VCO-1 is a potential difference between two points of the trimmer resistor VR_2 and VR_3. The period of the time-base is given by the timing and encoder instrument (TIM-ENC) of the spacecraft and coincides with the time interval of a word rate of ENC, that is, 125 ms.

The voltage controlled oscillator (VCO-1) is a Colpitts type. Q_1 is the silicon N-channel junction-type field effect transistor (FET), and CR_1 and CR_2 are the epitaxial diffused junction Mesa type silicon diodes (Vari-cap diodes), characteristics of which are shown in Fig. 15. The frequency of this oscillator is expressed as

$$f=\frac{1}{2\pi}\sqrt{\frac{1}{LC_0}+\frac{\Delta y}{C_1\cdot C_2}} \tag{3.1}$$

where $C_0=(C_1\cdot C_2)/(C_1+C_2)$ and $\Delta y=y_i y_0-y_r y_f$. C_1 and C_2 are the capacities of the vari-cap diodes CR_1 and CR_2 which change its values depending upon the applied voltage from the saw-tooth generator. y_i, y_0, y_r and y_f are the input admit-

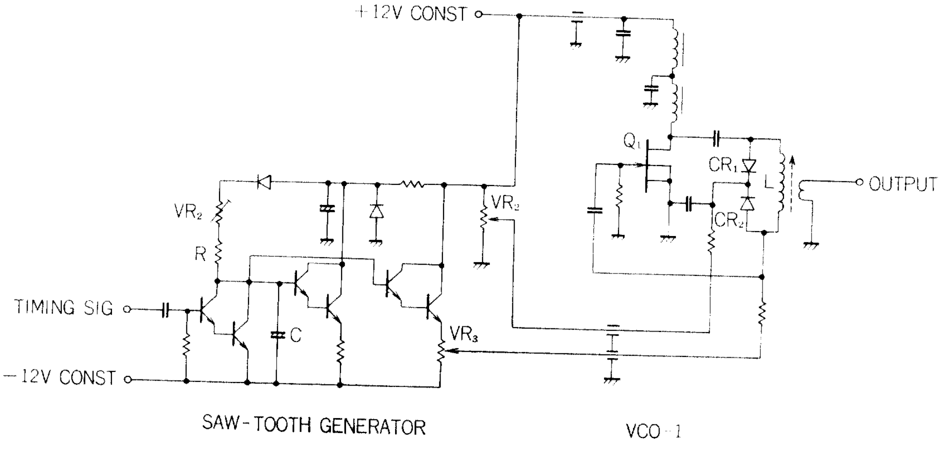

FIG. 14. Saw-tooth generator and voltage controlled oscillator.

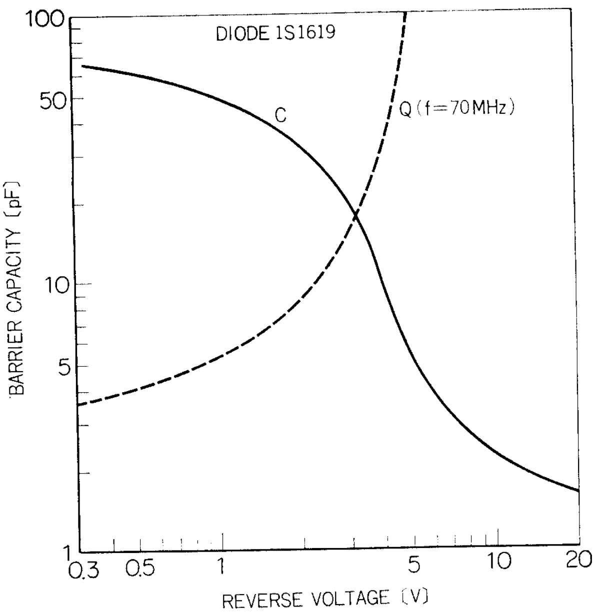

FIG. 15. Characteristics of the vari-cap diodes CR_1 and CR_2 (1S1619).

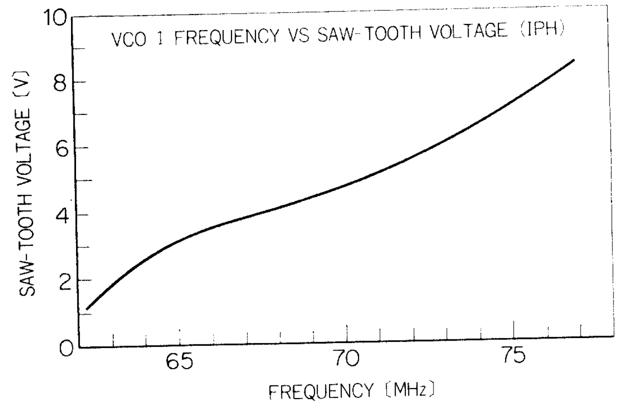

FIG. 16. Oscillation frequency versus applied saw-tooth voltage of the controlled oscillator VCO-1.

tance, output admittance, reverse transadmittance, and forward transadmittance of the transistor Q_1, respectively. Therefore, this type of oscillator is influenced by an active element in general.

The swept frequency range of this oscillator is 77.1 MHz to 62.3 MHz and its output voltage amplitude is 50 mV±1 dB. The relation of the swept frequency to the saw-tooth voltage applied to the VCO-1 is illustrated in Fig. 16. The time versus the swept frequency is shown in Fig. 17.

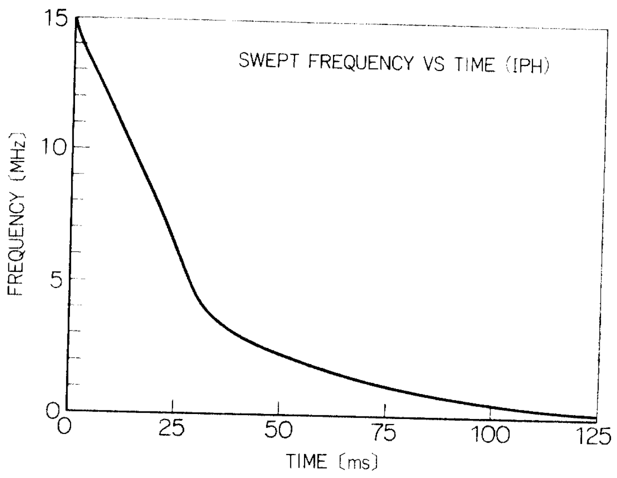

FIG. 17. Characteristics of swept frequency versus sweep time. Ordinate; frequency difference between output signal from VCO-1 and crystal controlled oscillator, 62.100 MHz.

3.2 *Swept frequency signal and local signal generators*

The swept frequency signal (77.1 MHz to 62.3 MHz) of VCO-1 is converted into two values by two mixers with two different crystal oscillators. These systems are illustrated in Fig. 18. The frequency relation between f_s and $f_{1\sim 6}$ is as follows. Mixer 1 and mixer 2 are double balanced modulators, then, $f_3=f_s \pm f_1$ and $f_4=f_s \pm f_2$. The high frequency conponents of them are eliminated through the low path filters (LPF 1 and 2), after which $f_5=f_s-f_1$ and $f_6=f_s-f_2$. The frequency difference between f_5 (SWEEP SIGNAL) and f_6 (SWEEP LOCAL) is always 100 kHz, being used for the intermediate frequency of the IF amplifier. As the frequency difference between two crystal oscillators is just 100 kHz, the signal to noise ratio (S/N) is made extremely low by mixing the two signals if the buffer amplifiers are removed. Buffer amplifier 1 and 2 act as isolaters to prevent the

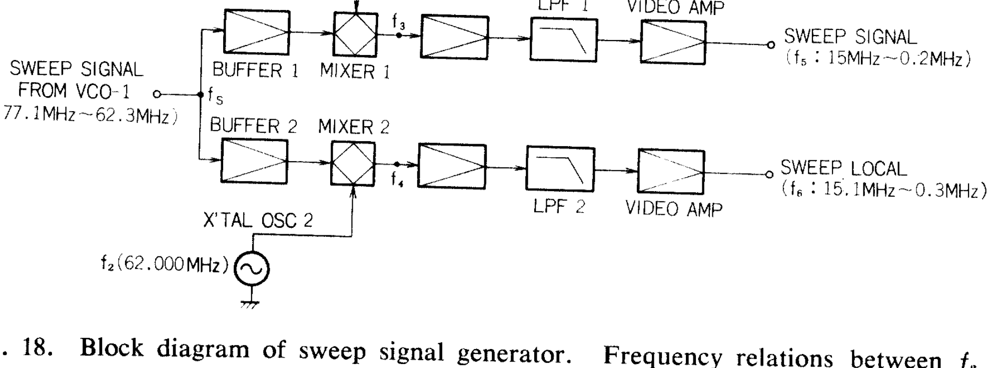

FIG. 18. Block diagram of sweep signal generator. Frequency relations between f_s and $f_{1\sim 6}$ are given in the parentheses.

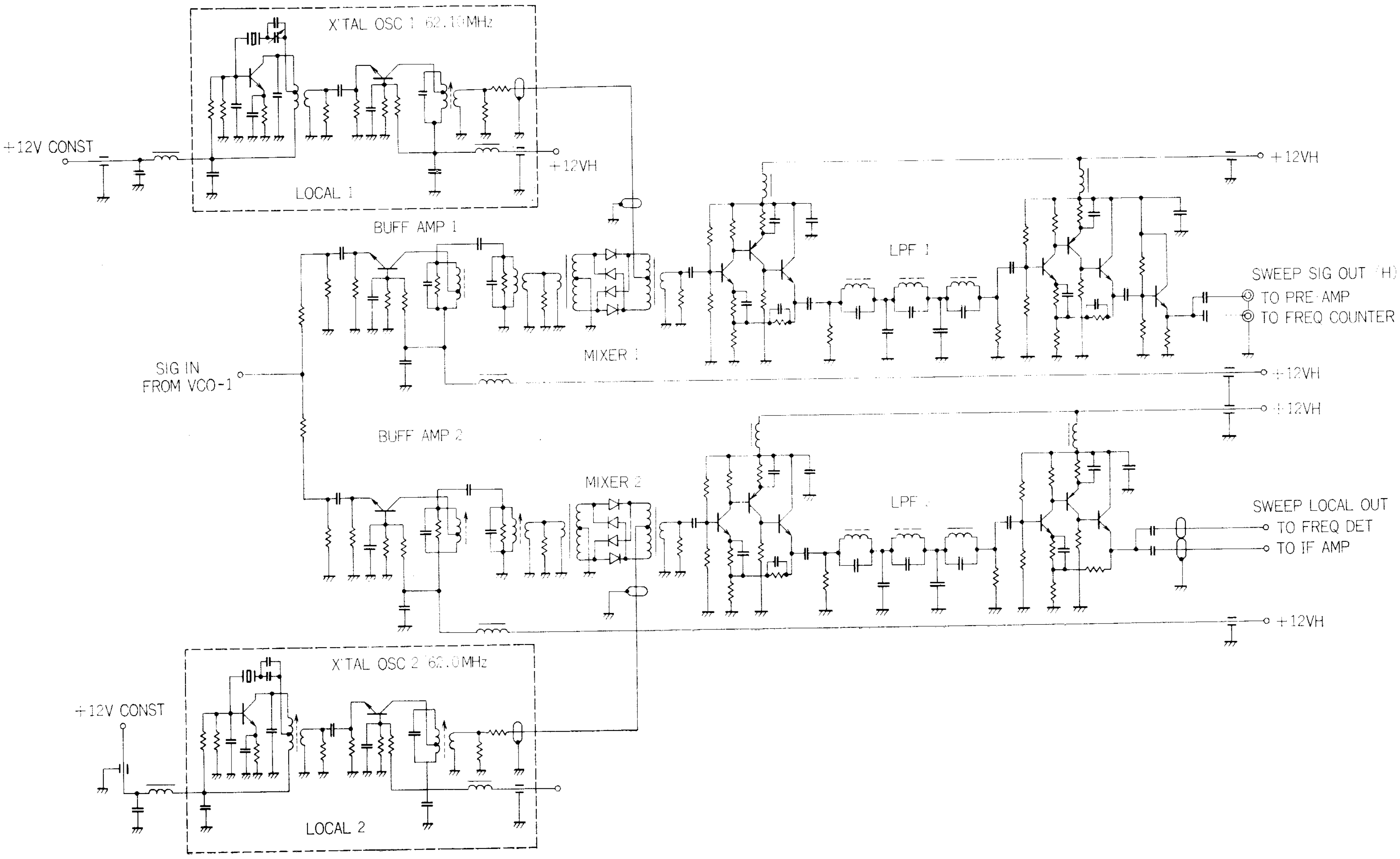

FIG. 19. Circuit diagram of sweep signal generator.

crystal oscillator signal on the other channel from mixing with the signal. The electrical circuits diagram of this section is given in Fig. 19.

X'tal OSC 1 and 2. The crystal-controlled oscillator used here is a Pierce-type of overtone oscillator with the crystal (HC-18/U) and the frequency stability is $3\times10^{-5}/°C$ ($-30°C\sim+60°C$). Frequencies of LOCAL 1 and 2 are 62.100 MHz and 62.000 MHz, respectively. These signals are used for local signals to the balanced modulators through the buffer amplifiers which suppress the interference from the signals from VCO-1.

Buffer 1 and 2 These amplifiers are double tuned amplifiers which have broad band width and 6 dB gain. The center frequency is 69.5 MHz and the bandwidth is ±8 MHz at −3 dB. As mentioned above, these amplifiers also act as isolaters, and their isolation is −46 dB.

Mixer 1 and 2 The use of double balanced modulators, which possess an appearance somewhat like the push-pull amplifier, automatically elliminates both the carrier (f_s) and the modulating frequency (f_1 or f_2), as well as many of the intermodulation frequencies. The carrieir f_s is balanced by the transformer and controls the values of resistance of the diodes against the modulating signal. Namely, the output signal contains frequency components of $f_s \pm f_1$ and $f_s \pm f_2$ without the carrier term f_s.

LPF and Video AMP To eliminate a high frequency component of the output signal from the mixer, a low-pass filter (inductive M-drived wave filter) is designed to have an image impedance of 50 Ω, a cut-off frequency of 25 MHz, and a fre-

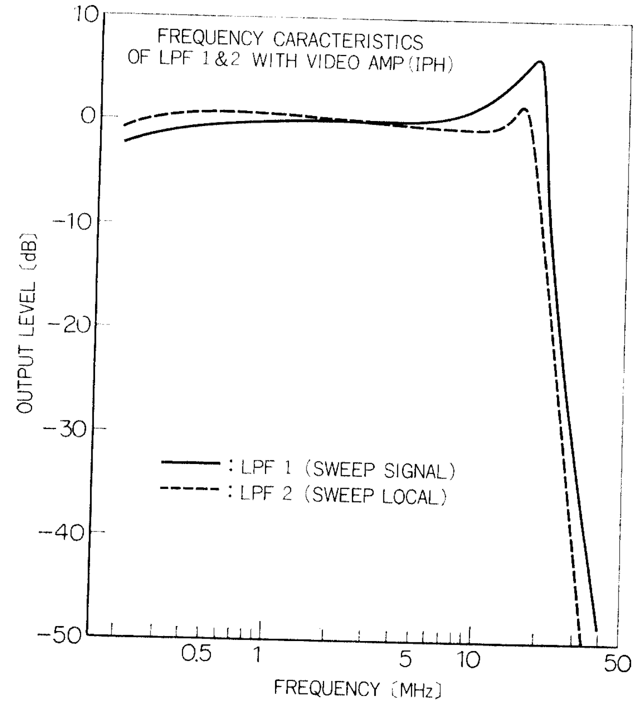

FIG. 20. Frequency characteristics of low pass filter and video amplifier.

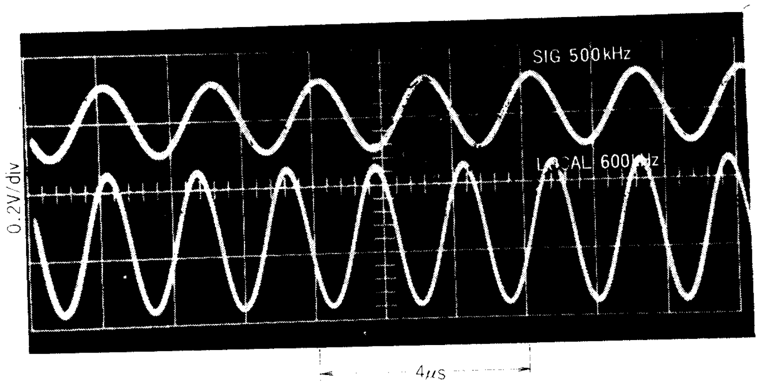

FIG. 21. Output wave form; upper trace: 500 kHz sweep signal, lower trace: 600 kHz sweep local signal.

quency of maximum attenuation of 40 MHz. The video amplifier is a current feedback amplifier which possesses 3 direct-coupled transistors. The cut-off frequency (−3 dB) is 18 MHz and its gain is 20 dB. Frequency characteristics of this system are shown in Fig. 20, and outputs of the swept frequency signals are 2.1 V_{p-p} for the supplied valtage to the pre-amplifier and 4.2 V_{p-p} for the local sweep signal. The sinusoidal wave forms are illustrated in Fig. 21.

3.3 *Signal detection system*

The output swept frequency signal from the pre-amplifier associated with the capacitance bridge and the sensor is converted into an intermediate frequency signal by the mixer IF amplifier. The use of double balanced mixer makes intermediate frequency and upper side-band frequency signals, that is, $f_{IF}=f_L \pm f_s$ where f_L is the swept local signal frequency and f_s the swept frequency that is adjusted to make difference 100 kHz from f_L. The upper side-band frequency is eliminated by the selective amplifier (IF AMP) and only the intermediate frequency signal is amplified and rectified by the linear detector. This d.c. signal from the rectifying circuit is supplied to the logarithmic amplifier; the output signal from the logarithmic amplifier is fed to the resonance detector circuit for the upper hybrid resonance frequency (Fh_1) and to the level hold circuit for $Lh_{1\sim3}$. In the other channel, the d.c. signal is fed to the linear amplifier for detection of the sheath resonance frequency (Fh_2). The electrical circuits diagram are described in Fig. 22.

Mixer As illustrated in the figure, the mixer is a diode bridge-type double balanced modulator whose input and output impedances are 50 Ω and 600 Ω, respectively. The unbalance characteristics of the diodes are corrected by the variable resistor VR located at the middle point of the secondary winding of the input transformer. The output swept signal frequency f_L (15 MHz to 0.2 MHz) from the pre-amplifier is converted to 100 kHz by mixing the local swept signal frequency f_s (15.1 MHz to 0.3 MHz).

IF AMP A selective amplification of the 100 kHz signal is made by the IF amplifier that is double tuned at the frequency 100 kHz with the band width of

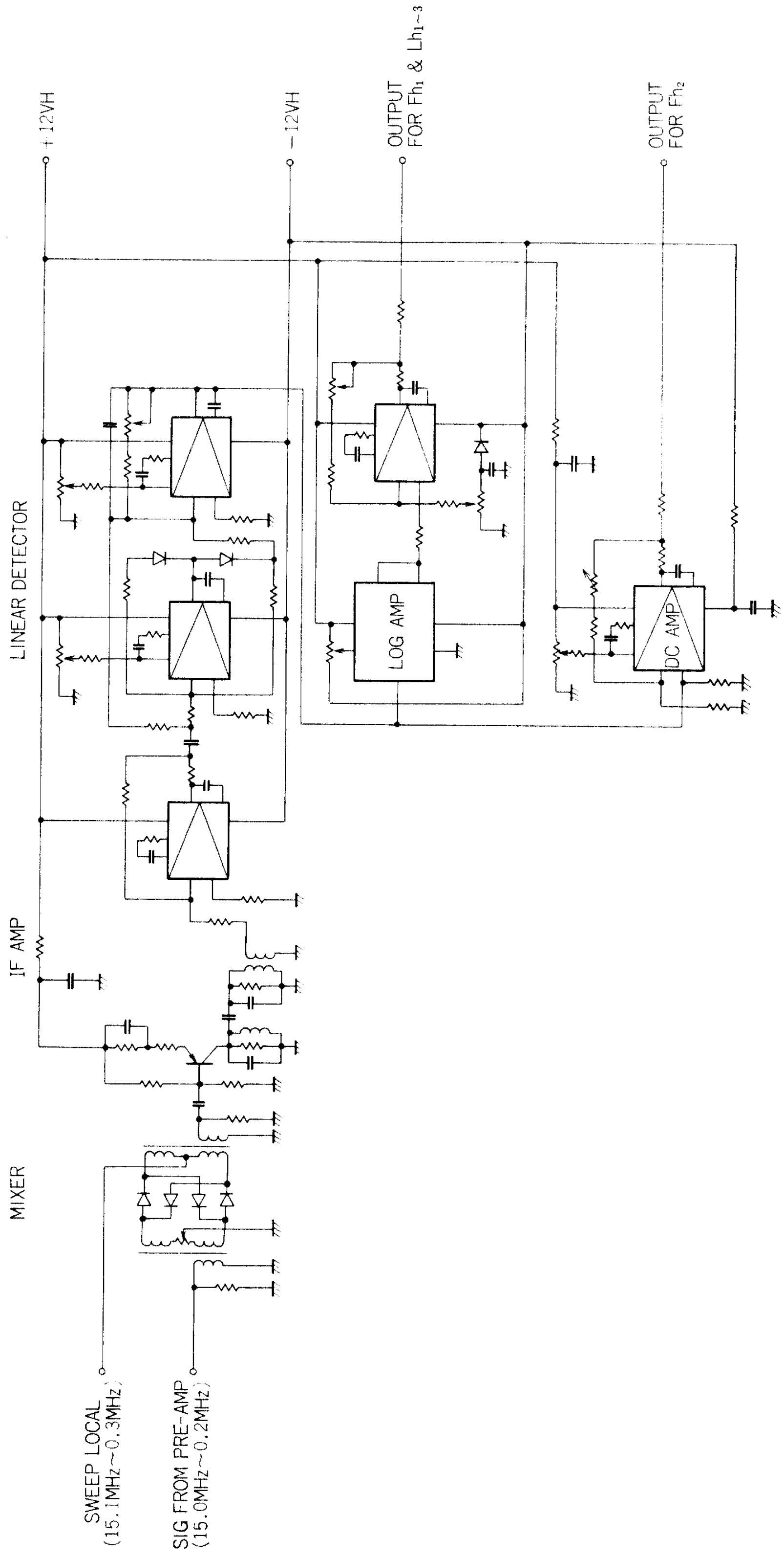

FIG. 22. Mixer, IF amplifier, linear detector, logarithmic amplifier and d.c. amplifier.

±1 kHz (at −3 dB point). Additional amplification by the operational amplifier yields the total gain of 60 dB. The selectivity at 500 kHz is −60 dB.

Linear Detector The diode rectifier of a conventional type has linear characteristics for the level range of 60 dB. Due to influence of the diode junction voltage and temperature dependence of the voltage-current characteristics, the linearity more than this dynamic range is impossible. In this circuit system, the operational amplifier with the pair diodes and the integrator used as the linear detector circuit, the dynamic range of which is 5 mV to 5 V (60 dB).

LOG AMP and Level Shift AMP In order to obtain a wide dynamic range for the antenna impedance measurement, the signal should be suppressed logarithmically. The LOG module model 4351 (PHILBRICK/NEXUS) is employed as the logarithmic amplifier. The transfer function is expressed as

$$e_{OUT}=\left[A\log_{10}\frac{\text{Imput Voltage}}{\text{Reference Voltage}}\right] \qquad (3.2)$$

where the sensitivity A is 1 V/decade. The input −1 mV to −10 V is compressed to about −2 V to +2 V at the output. This output voltage is transformed to 0 V to 4 V through the level shift amplifier. The transformed signal in 0–4 volts range is used for automatic detection of the upper hybrid resonance (Fh_1) and the impedance values ($Lh_{1\sim3}$). The characteristics of the input versus output level of this system is shown in Fig. 23.

Linear D.C. AMP The logarithmic amplification of the antenna impedance is inconvenient to detect the sheath resonance frequency, because the sheath resonance

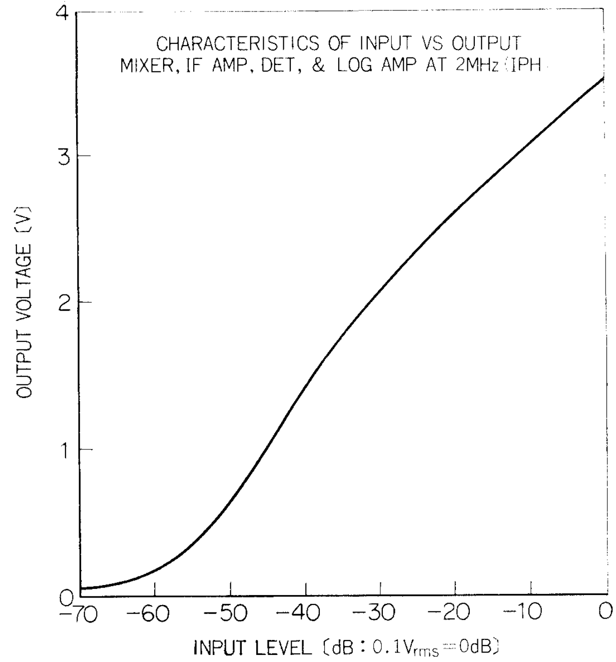

FIG. 23. Characteristics of input versus output of IF and logarithmic amplifiers. Dynamic range≃60 dB.

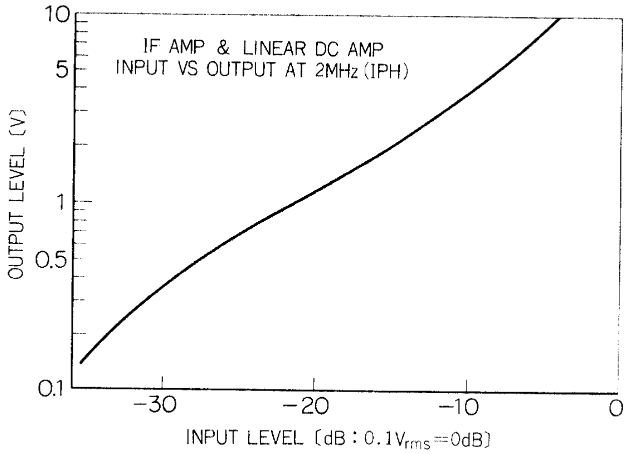

FIG. 24. Characteristics of input versus output of IF and linear d.c. amplifiers. Dynamic range≃40 dB.

is characterized by a peak value of the admittance that can be compressed if the logarithmic amplifier is used. The d.c. linear operational amplifier is then employed. The characteristics of input versus output level of this system is shown in Fig. 24.

3.4 Frequency detector

For the automatic measurement of the antenna admittance value at a given frequency, a control signal is fed to a sampling-hold circuit at the time when the swept frequency coincides with a given frequency. The frequency detector circuit for 0.3 MHz and 13 MHz is illustrated in Fig. 25. For this purpose the input sweep signal with the frequency f_L is supplied to the L-C tank circuit that are tuned at 0.4 MHz and 13.1 MHz to give the time of detection at 0.3 MHz and 13 MHz, respectively. When the sweep signal f_s is fed to the tank circuit, the sweep signal level is changed at the given frequencies due to reaction of the LC resonance circuit.

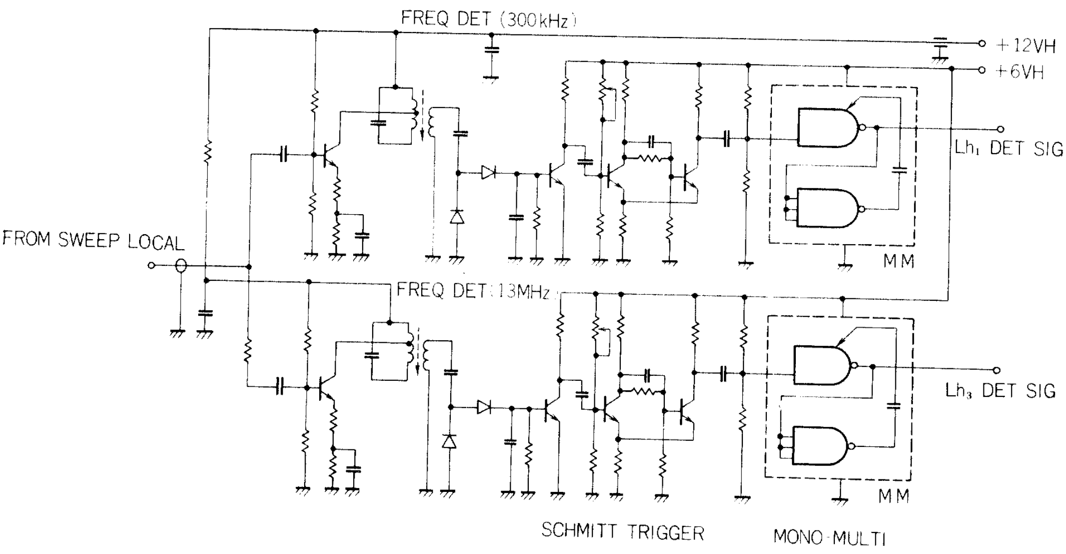

FIG. 25. Frequency detector circuit (0.3 MHz and 13 MHz).

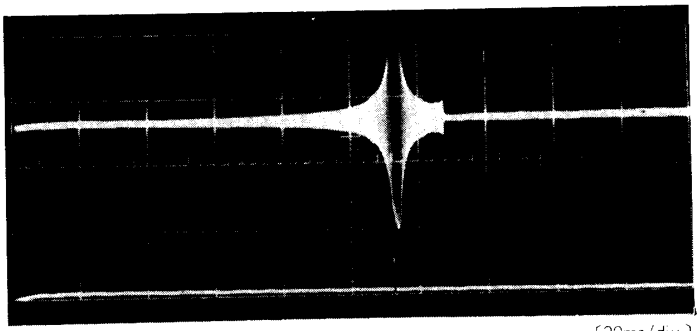

(a) 0.3MHz FREQ DET [20ms/div.]

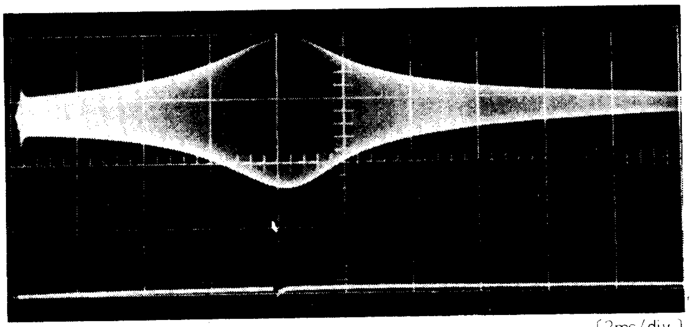

(b) 13MHz FREQ DET [2ms/div.]

FIG. 26. Output wave form from the tuned amplifier (upper trace) and frequency detect pulse with pulse width of 100 μsec from the monostable multivibrator (lower trace).

This change is unsuitable for the antenna impedance measurement. The output signals from the tuned circuit indicate r.f. pulse form which is rectified by a diode that produce a pulse. The wave form of the output signals from the L-C tank circuits and the monostable multivibrators are illustrated in Fig. 26. The produced pulse can be reshaped through a Schmitt trigger circuit. A pulse from the Schmitt trigger circuit induces a transition from the stable state of a monostable multivibrator to the quasi-stable state. The monostable multivibrator may remain in this quasi-stable state for 100 μs which is determined by the RC time constant, and return from the quasi-stable state to the stable state, spontaneously. Thus, the rectangular wave form is obtained; this pulse gates the circuit for the automatic sampling of the Lh_1 and Lh_3 values at the frequencies of 0.3 MHz and 13 MHz, respectively.

3.5 *Automatic data sampling system*

The signals to PCM telemetry transmitter should be adapted to time-shared telemetry channels. The antenna admittance levels at frequencies 0.3 MHz, f_{UHR} and 13 MHz, that are obtained at the output points of the logarithmic amplifier, are sampled and stored when frequency detection and resonance detection pulses are submitted to the gate control circuit at the time of swept frequency coincidence at 0.3 MHz, f_{UHR} and 13 MHz. For the identification of upper hybrid resonance, the output singnal from the logarithmic amplifier is applied to two circuits; one is a differentiator which produces a gating pulse at the resonance and another is a com-

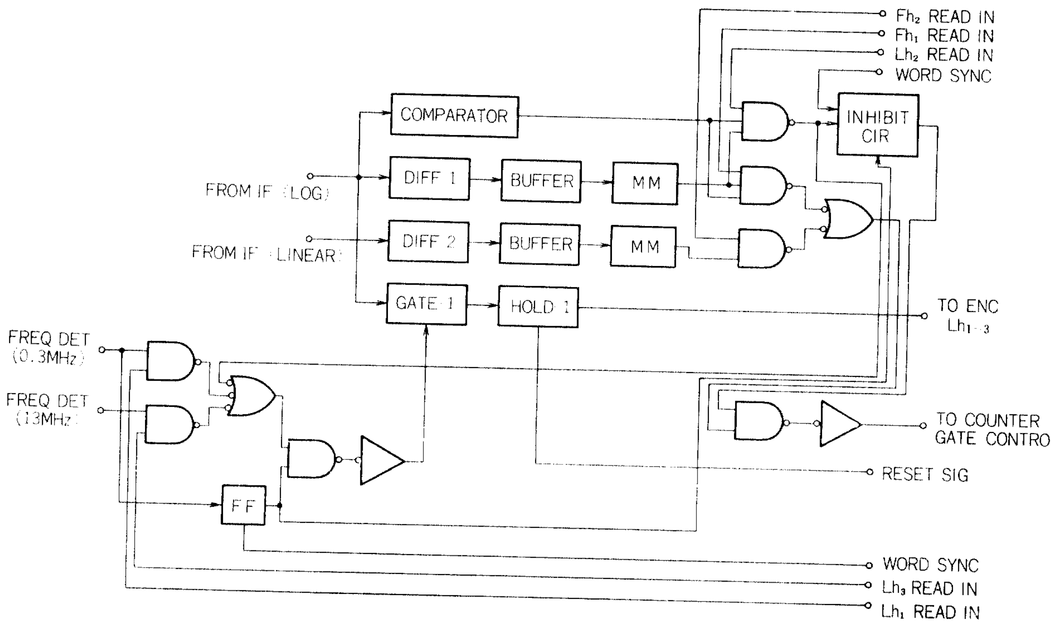

FIG. 27. Functional block diagram of resonance detectors for Fh$_1$ and Fh$_2$ and sampling-hold circuit for Lh$_{1\sim3}$, including the inhibit circuit.

parator which excludes the pseudo resonance spikes raised by noise contamination. Since the upper hybrid resonance is characterized by minimum of the admittance versus applied swept frequency, the reference level of comparator for upper hybrid resonance detection is designed to be the antenna admittance value in free space. The sheath resonance can be detected by differentiating the output signal from linear d.c. amplifier. The detection of sheath resonance is thought to be negligible interference from the small level noise because the resonance is characterized by maximum value of the antenna admittance. Therefore the comparator is not used in this system. Both upper hybrid resonance and sheath resonance frequencies (Fh_1 & Fh_2) are measured by a frequency counter that is gated for the pulse counting triggered by these resonance detection pulses. The functional block diagram and electrical circuit of this section are illustrated in Figs. 27 and 28. The differentiator consists of emitter follower amplifiers, low pass filters, differentiators and Schmitt trigger circuits. The low pass filter with cut-off frequency of 1 kHz is used for the noise screening. The time differentiation of admittance value vs. swept frequency at the output point of the logarithmic amplifier is obtained by R-C circuits. At the resonance point, the differentiated signal gives the turn-on signal to the grounded-base junction transistor which drives the Schmitt trigger circuit. The Schmitt trigger circuit produces a gating pulse for the monostable multivibrator. The performance of the comparator circuit is illustrated in Fig. 29, and also the output signals of the monostable multivibrators for the parallel and series resonances are shown in Fig. 30; signals are those responses for the electrical parallel and series resonant circuits impedance.

Sampling-Hold Circuit The sampling circuit consists of junction type FET's that works as an analog switching element; gates are opened by a trigger from the data

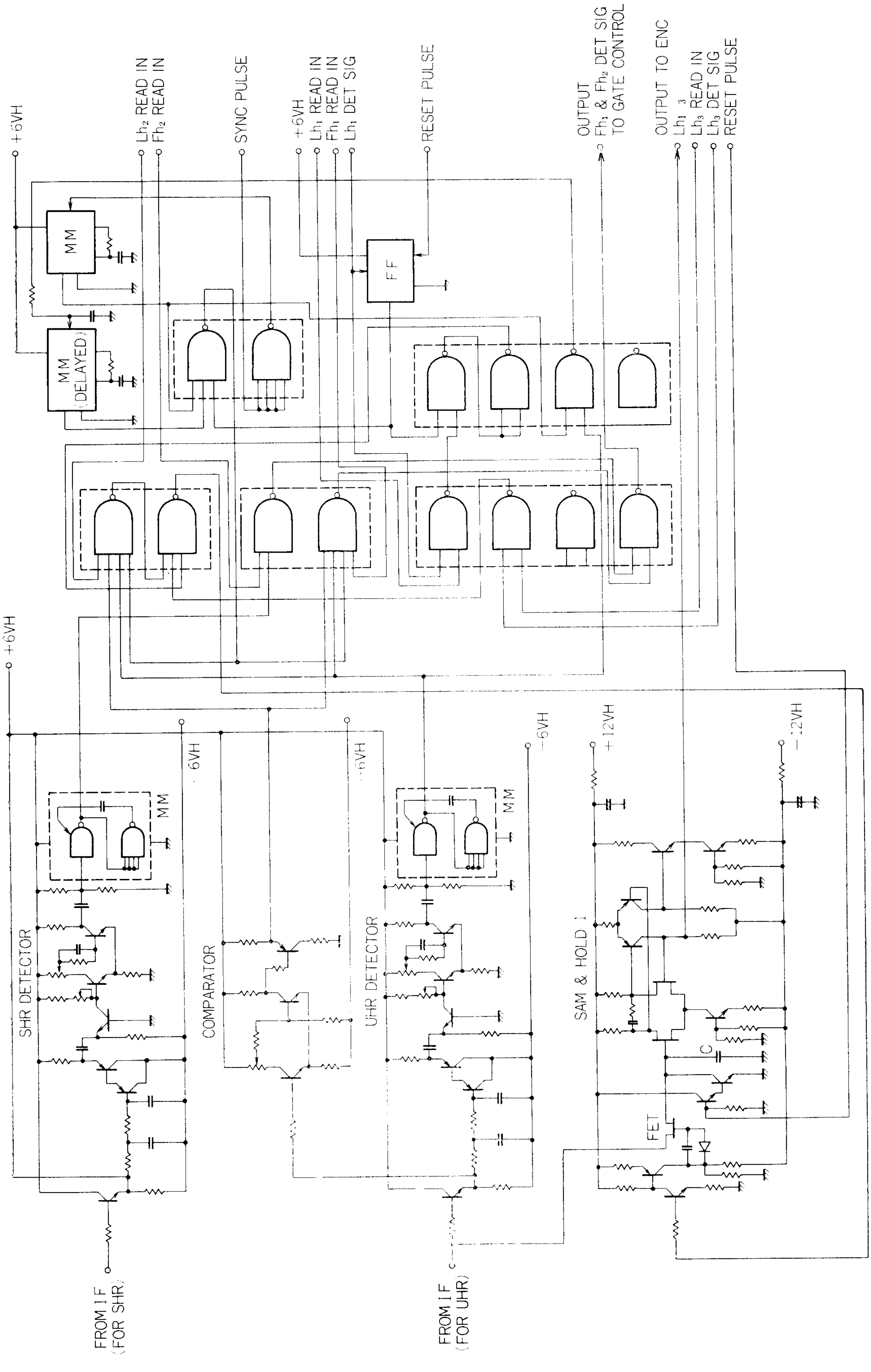

FIG. 28. Resonance detector and sampling-hold circuit.

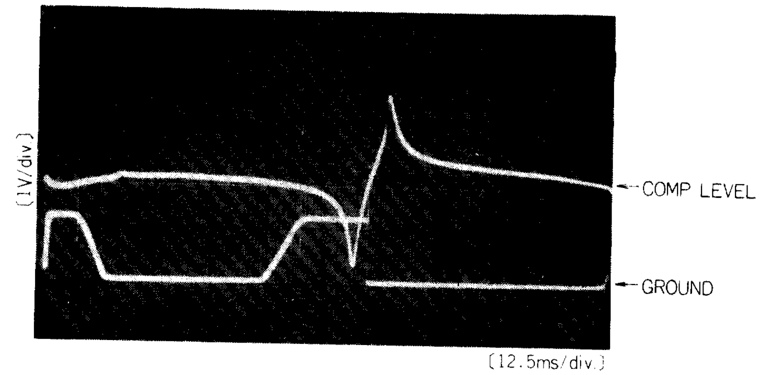

FIG. 29. Pulse wave form (lower trace) from the comparator; dummy resonance circuit are used. The wave form of output signal from the logarithmic amplifier is superimposed (upper trace).

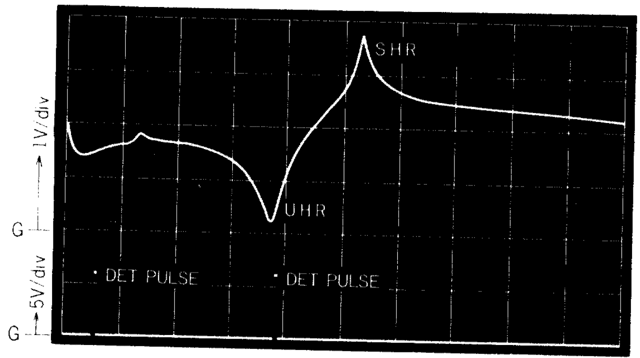

(a) UHR DETECTOR [125ms/10div]

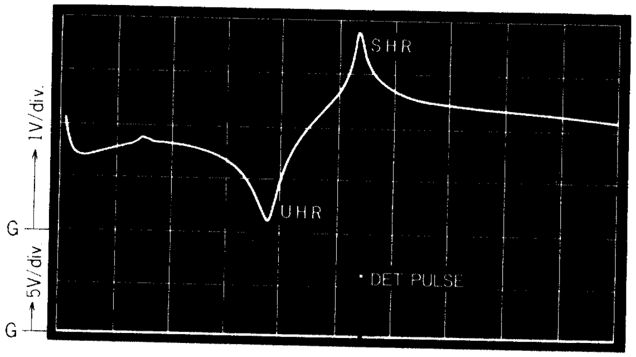

(b) SHR DETECTOR [125ms/10div]

FIG. 30. Output pulse of resonance detector; output from logarithmic amplifier is superimposed (upper trace).

channel selector as will be discussed later. The sampling gate time is 100 μs, i.e., the same interval with the pulse width of the monostable multivibrator. Sampled potential values are stored in a charging condenser C and discharged to zero value by the reset signal. The potential of C is transmitted to the encoder circuit (ENC) through a negative feedback d.c. amplifier that operates as buffer circuits with a high input impedance. The gain of this amplifier is set to 0 dB. The input versus output characteristics of the sampling-hold circuit is given in Fg. 31. The

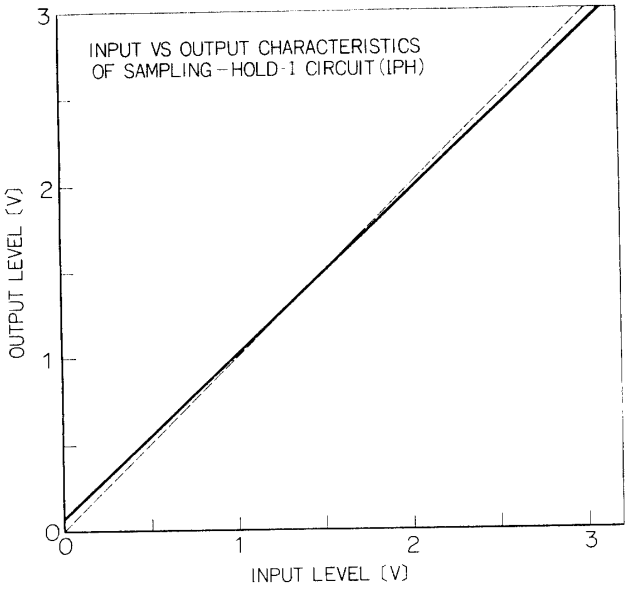

FIG. 31. Input versus output characteristics of the sampling-hold circuit.

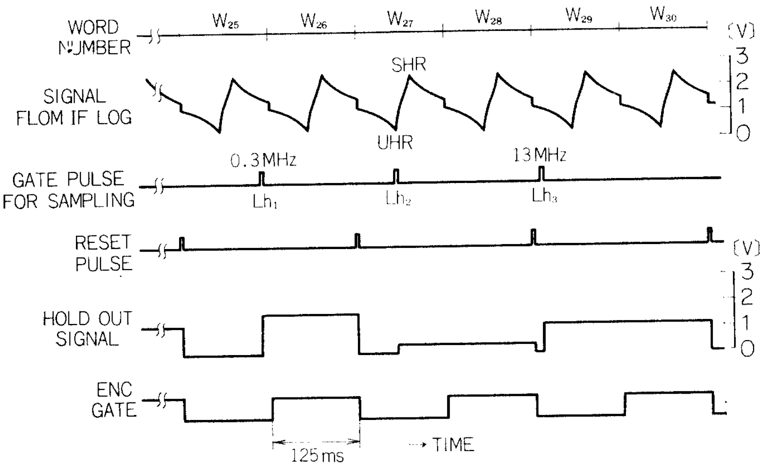

FIG. 32. Schematic time sequence of the sampling-hold circuit. For example, Lh_1 (admittance level at 0.3 MHz) is allocated at W_{26}, and the detect pulse is applied to the gate of sampling-hold circuit at W_{25}. The sampled potential is stored and transmitted to ENC at W_{26}, being discharged by the reset pulse at the end of W_{26}.

operation time sequence for a typical impedance function is illustrated in Fig. 32.

Data Channel Selector Circuit The mode II_1 ($W_8 \sim W_{31}$) of the telemetry time sequence is used for IPH; the odd word numbers are for the counted digital frequency of the upper hybrid and sheath resonances (Fh_1 and Fh_2); and the even word numbers are for the sampled values of the admittance levels $Lh_{1\sim3}$. By using the data channel selector circuit, time parallel signals of $Lh_{1\sim2}$ in the hold circuits are re-arranged to be the time serial signal for adaption to the time-sharing telemetry

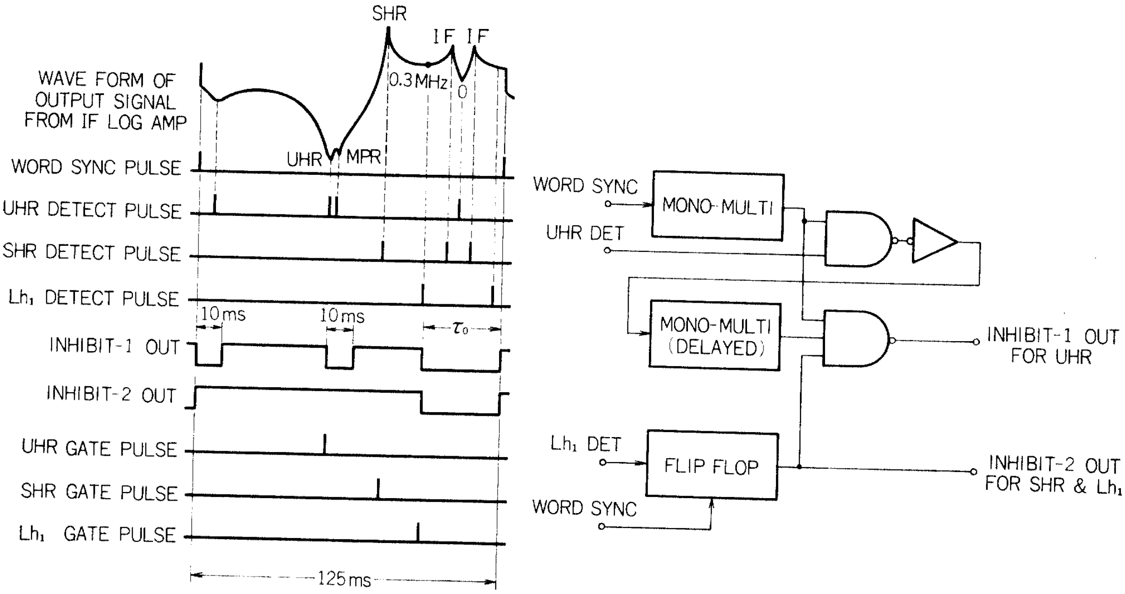

FIG. 33. Operational performance of inhibit circuit.

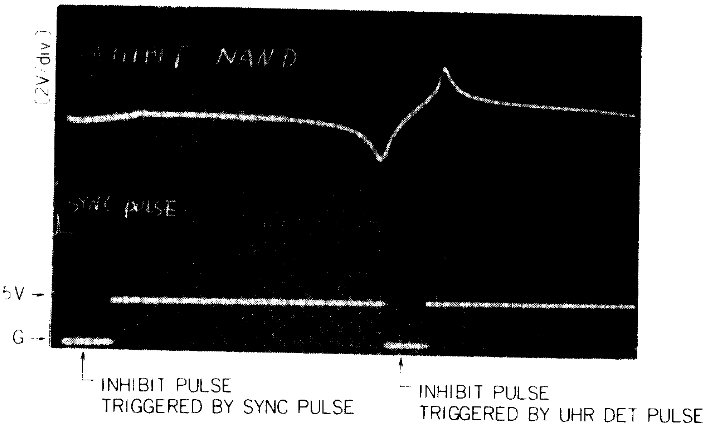

FIG. 34. Output pulse (lower trace) of delayed monostable multivibrator of the inhibit circuit. First pulse is triggered by word synchronous pulse and second pulse is triggered by UHR detect pulse. Output curve from logarithmic amplifier is superimposed (upper trace).

sequence. The data are sampled and stored during one word interval of the telemetry sequence before reading out to ENC. Near the starting and ending frequencies of the sweep signal, pseudo pulses are generated due to the circuit characteristics. An active elimination of these pulses are made by using logical inhibit circuits. The operational procedure of the inhibit circuit is shown in Fig. 33. The time duration of the inhibit pulses are designed to be 10 ms and τ_0. τ_0 is determined by the set trigger of the first Lh_1 detect pulse and the reset trigger of the word synchronous pulse. The output pulse wave form of the delayed monostable multivibrator is shown in Fig. 34.

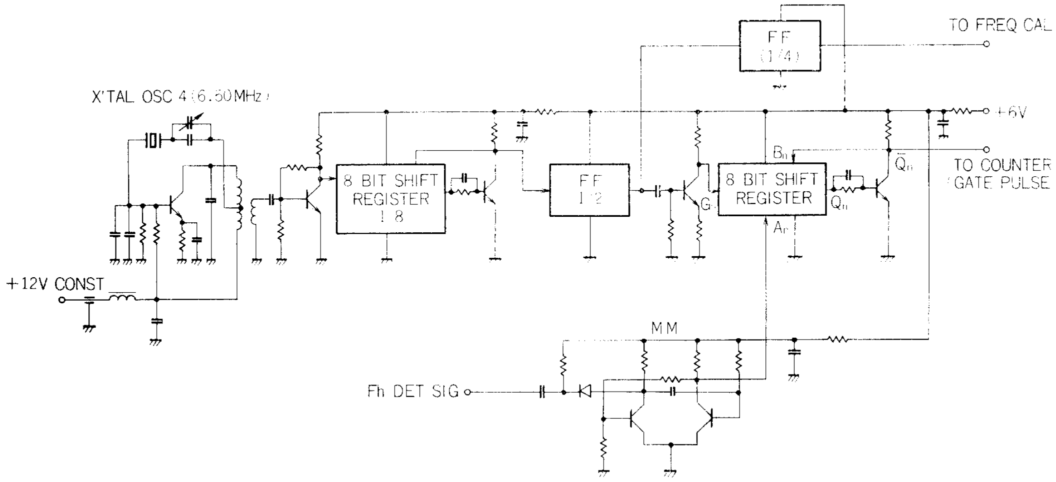

FIG. 35. Gate width control circuit.

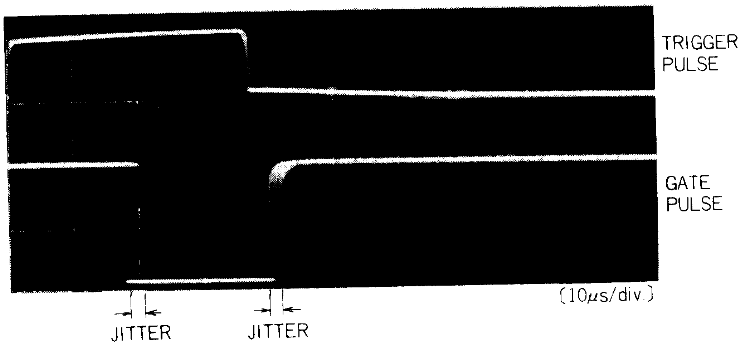

FIG. 36. Gate pulse (lower trace) and output pulse of the monostable multivibrator (upper trace). Gate width is 19.692 μsec and jitter of pulse appears because several traces are superimposed.

3.6 *Gate-width control circuit*

The gate-width control circuit illustrated in Fig. 35 generates a gate pulse to the frequency counter for Fh_1 and Fh_2, and the frequency calibration signal. The crystal controlled oscillator of Pierce-type is used as the standard signal (6.5000 MHz). This standard frequency is demultiplied by 16 through the 8-bit shift resistor coupled to the flip-flop circuit.

The signal of 406.25 kHz (=6.5000 MHz/16) is applied to two circuits; one is the flip-flop circuit which demultiplies the signal by 4 and sends to the frequency calibration circuit, the other is an 8-bit shift resistor. The logical function of the 8-bit shift resistor is given as,

$$A_n \cdot B_m = Q_{n+8},$$

where A_n is the output pulse of the monostable multivibrator which is triggered (say at $n=1$) by the *UHR* and *SHR* detect pulses, and B_n is the inverted pulse of

Q_n. The clock time τ of the pulse G_n is equal to the value of 1/406.25 kHz, i.e., $\tau=2.4615\ \mu s$. Since the pulse width of the monostable multivibrator is designed to be less than $16\tau(n=16)$ and longer than $8\tau(n=8)$, $Q_n=1(9\leq n\leq 16)$. Consequently, the output pulse width of the 8-bit shift resistor is just 8τ (19.692 μs) which is controlled accurately by the frequency of the crystal controlled oscillator and is gated at the time after 8τ period by the triggering of the monostable multivibrator. This pulse is used as a gate pulse to the frequency counter for Fh_1 and Fh_2. The gate pulse and the output pulse of the monostable multivibrator are shown in Fig. 36. Jittering (2.46 μs) of this pulse repetition time is raised by time difference between the clock pulse and the *UHR* or *SHR* detect pulse. Then, the time delay of the gate pulse becomes $19.692\pm 2.46\ \mu s$, but this is negligible compared with the swept frequency period (125 ms).

3.7 *Frequency counter*

The swept frequency is counted by the series of 8-bit binary counters during the gating interval, for Fh_1 or Fh_2, that is fed from the gate width control circuit, and transmitted to ENC after time-parallel to time-serial conversion through the

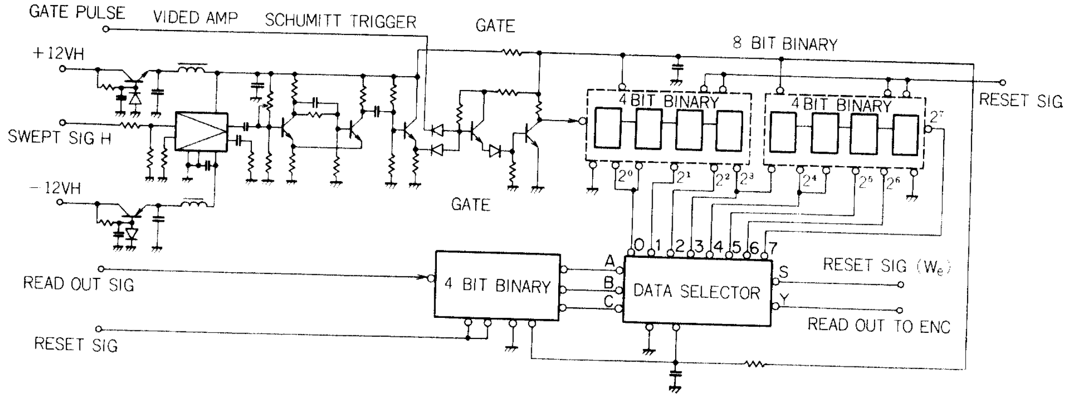

FIG. 37. Frequency counter.

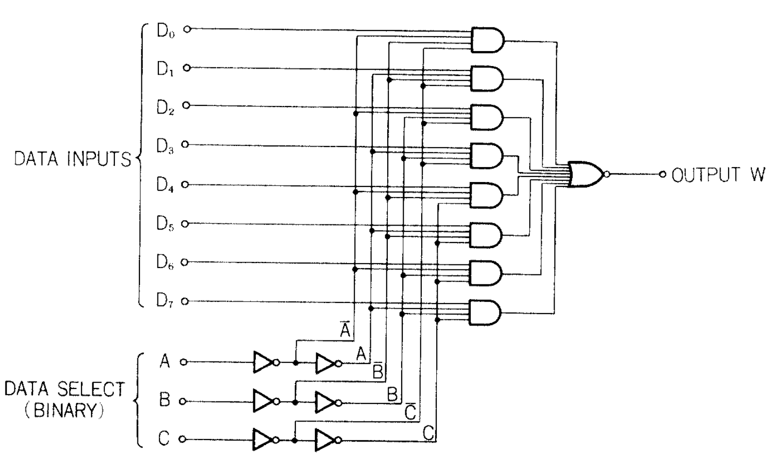

FIG. 38. Functional block diagram of data selector, SN 54151.

data selector. The electrical circuit for this operation is illustrated in Fig. 37.

The swept signal is fed to the video amplifier to get 20 dB amplification for triggering the Schmitt circuit. The output wave form of the Schmitt trigger circuit is differentiated and fed to the 8-bit binary counter through the gate circuit. The pulse width of this gate circuit is 19.692 μs, equivalent to the frequency of 50.782 kHz. The available maximum frequency of this counter is 12.949 MHz, i.e., 255 (maximum) counts of the 8-bit binary with the unit of 50.782 kHz for one count.

The parallel output pulses from the 8-bit binary counter are fed to the data selector and read out in time-series form by the Fh_1 or Fh_2 read out pulse from the TIM-ENC circuit. The data selector is a TTL-MSI (Transistor Transistor Logic-Middle Scale Integration) circuit SN 54151 (TEXAS Inst.), the block diagram of which is shown in Fig. 38. This circuit element are used to performs the parallel-to-serial conversion. The logical operation of the circuit is expressed as,

$$\begin{aligned} Y=&\bar{S}(\bar{A}\bar{B}\bar{C}D_0+A\bar{B}\bar{C}D_1+\bar{A}B\bar{C}D_2+AB\bar{C}D_3+\bar{A}\bar{B}CD_4+A\bar{B}CD_5 \\ &+\bar{A}BCD_6+ABCD_7), \end{aligned} \tag{3.3}$$

and $W=\bar{Y}$

where the $D_{0\sim7}$ are the inputs from the binary counter; A, B, and C are the data selecting pulses generated by the 4-bit binary counter using the read out bit pulses from TIM-ENC and $\bar{A}$ shows the inverted pulse of A. S is the reset pulse. The time sequence of the digital read out pulses to ENC is in series of MSB (Most Significant Bit).

The frequency counting is subjected to the relative error that increases as the frequency decreases, when the gate pulse width is constant while the frequency is swept as linear function of time t. Taking t_1 and t_2 to be the opening and closing time of the gate, the relative error of the frequency E is given by,

$$E=\frac{f(t_1)\Delta\tau-\int_{t_1}^{t_2}f(t)dt}{f(t_1)\Delta\tau}\pm\frac{1}{f(t_1)\Delta\tau}\equiv E_0\pm E_1 \tag{3.4}$$

where $f(t)$ is the swept frequency as a function of the time t, and $\Delta\tau=t_2-t_1$ is the gate pulse width. For a constant value of $E(\ll 1)$, the approximate solution of this integral equation is given as

$$f(t)=f_0\exp\left(-\frac{2E}{\Delta\tau}t\right)\mp\frac{1}{\Delta\tau} \tag{3.5}$$

where $\mp 1/\Delta\tau$ ($\mp$50.782 kHz) is the correcting term against the frequency resolution rate of the counter and f_0 is the maximum frequency at t=0. As is shown previously in section 3.1 and also in Fig. 17, the time dependence of swept frequency is designed to have an exponential function for $f(t)$, so as to make E_0 independent to t. The estimated relative error E_0 is computed for swept frequency function $f(t)$, shown in Fig. 17, as illustrated in Fig. 39 with the frequency resolution limit of this

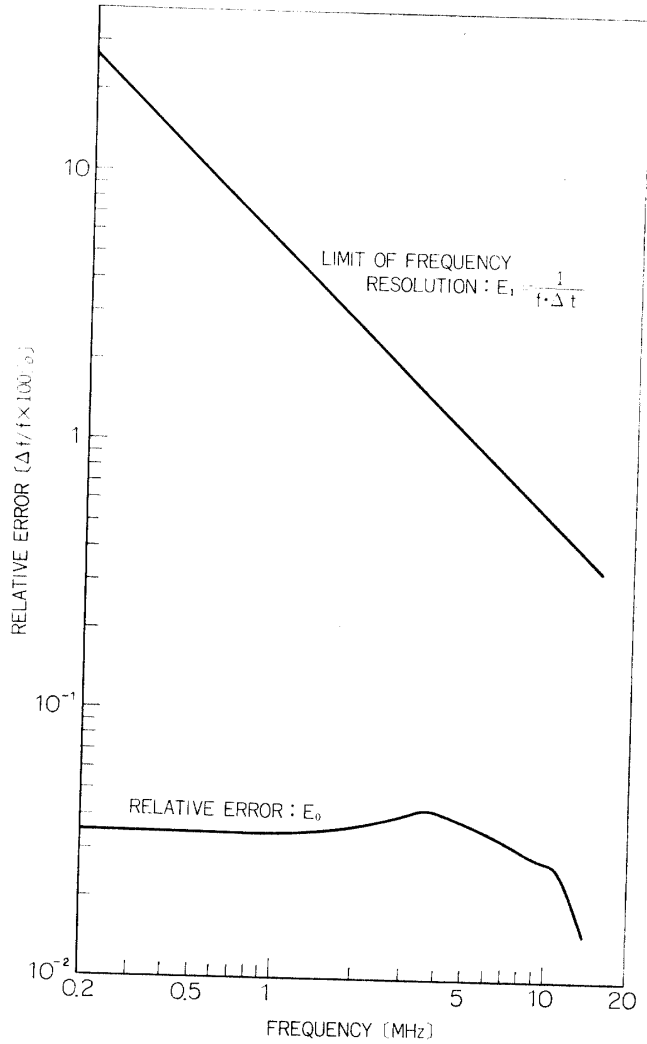

FIG. 39. Relative frequency error (E_0 and E_1) of frequency counter system.

counter. E_0 is approximately constant (about 4×10^{-4}) in a range below 10 MHz and negligibly small compared with the frequency resolution limit.

III-4 Low Frequency Gyro-plasma Probe

The antenna impedance as a function of the swept frequency in the low frequency range, including a lower hybrid resonance frequency, can be obtained by the low frequency gyro-plasma probe (IPL). The swept frequency signal is generated by a CR phase shift oscillator, the frequency of which is controlled by the saw-tooth (serrasoidal) voltage wave form. The frequency is beated-down using a crystal oscillator through the mixer, i.e., a kind of beat oscillators is formed. The high frequency side band (65 kHz~79 kHz) of the output signal from the mixer is produced through the high-pass filter and applied to a frequency calibration circuit. The low frequency component (1 kHz~15 kHz) is obtained through the low-pass filter and used as the swept frequency signal that is applied to the antenna and to the frequency detection circuit. The antenna impedance is measured by the capacitance bridge associated with pre-amplifier, the output signal from which is converted to IF signal (32 kHz) and detected through the IF amplifier and linear detector. The frequency and resonance detectors for identification of the time at 1.25 kHz, 3.80 kHz, 6.65 kHz, 10.1 kHz and f_{LHR} associated with the logarithmic amplifier, sampling-hold circuit and data processing circuit are presented.

4.1 *Swept frequency signal generator*

The swept frequency signal in a frequency range of 1 kHz to 15 kHz is used for the source signal of the IPL system. The used frequency signal is steped up from 65 kHz to 79 kHz for the frequency calibration. The block diagram and the electrical circuit which generates these signals are illustrated in Fig. 40 and Fig. 41.

Saw-Tooth Generator This circuit is a bootstrap sweep circuit that is the same type as is used in IPH saw-tooth generator; but in this circuit the deviation from linearity of the serrasoidal wave form is very small, due to current feedback through the large capacity condenser C_1. The output transistor of the emitter follower circuit are controlled not to saturate at high potential, using three serial diode $D_{1\sim3}$ for the level shift operation. The emitter follower circuit consists of a complementary compound (Darlington) connection of PNP and NPN transistors, in order to set the beginning potential of the saw-tooth to be just 0 volt. The start-end controll of the saw-tooth generation circuit is given by the word synchronous pulse from TIM-ENC that coincides with a time period of a word rate controlling at ENC, i.e., 125 ms. The output signal from the terminal VR_1 is applied to the voltage controlled oscillator and that from VR_2 is used for the reference voltage of Fl and $Cl_{1\sim4}$. Wave forms from these terminals are illustrated in Fig. 42.

VCO-2 The voltage controlled oscillator (VCO-2) is the modified high-pass-type phase shift oscillator. The phase of a current is advanced by four CR ladder circuits and the oscillating frequency is selected due to the condition to satisfy that the phase of feed-back signal advances by 180° from that of the input signal. In this circuit, the signals having the different phases from 3rd stage and 4th stage of

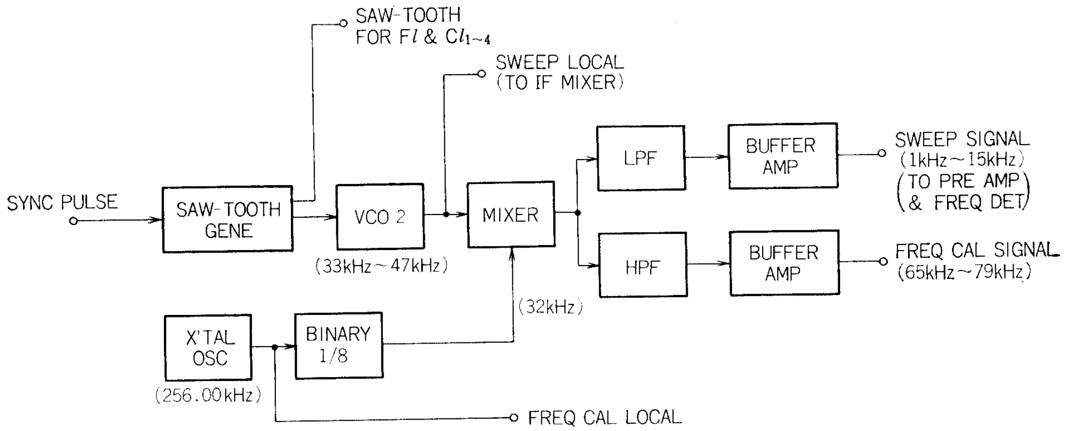

FIG. 40. System block diagram of swept frequency signal generator.

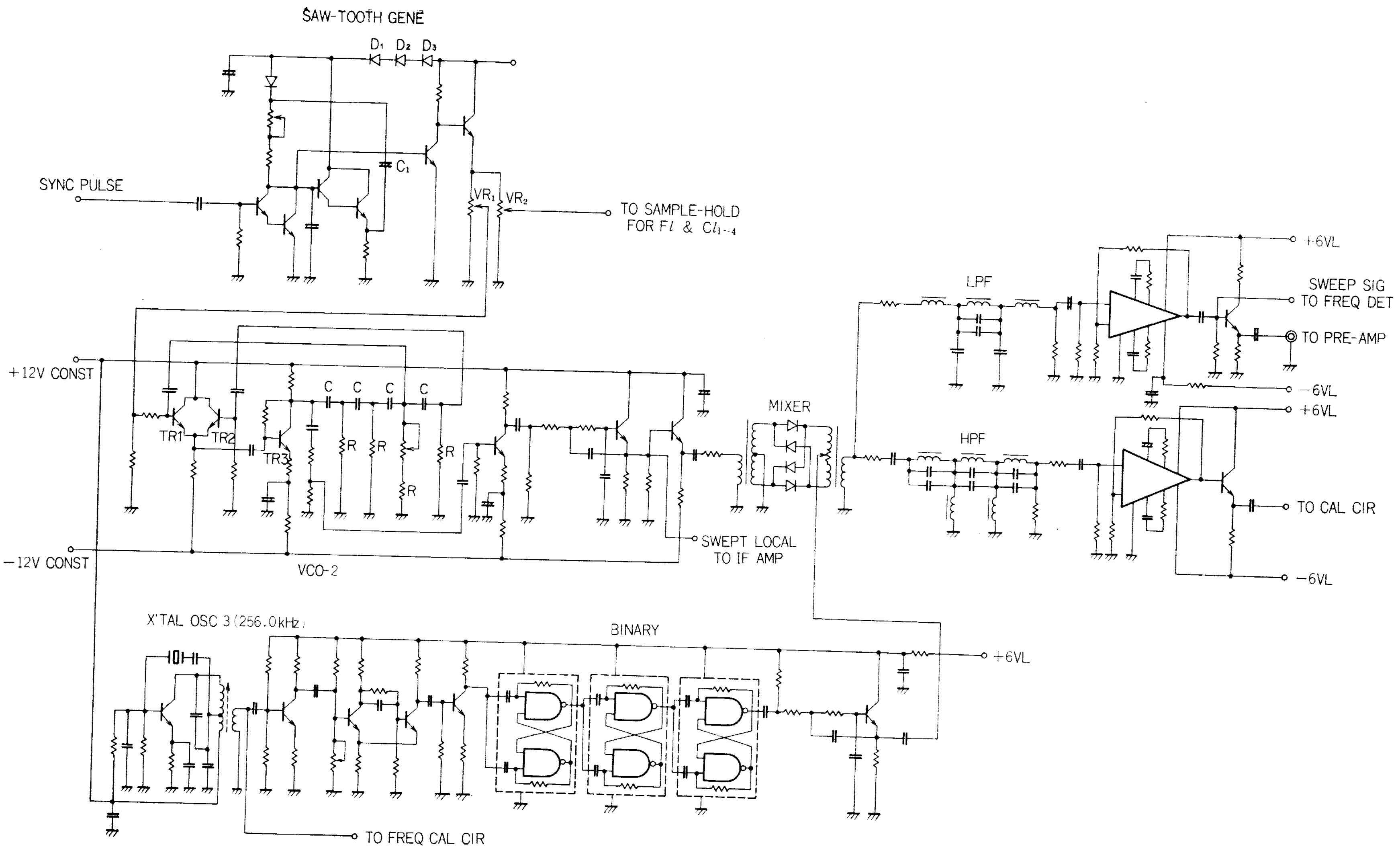

FIG. 41. Circuit diagram of sweep frequency signal generator.

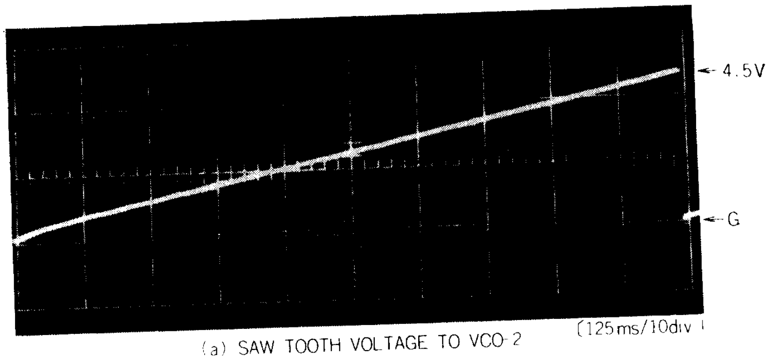

(a) SAW TOOTH VOLTAGE TO VCO-2 (125ms/10div)

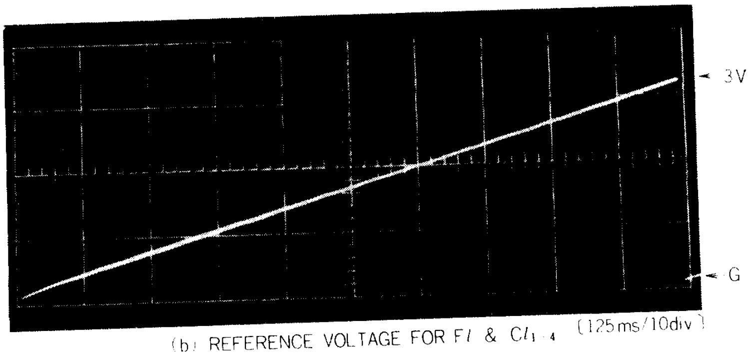

(b) REFERENCE VOLTAGE FOR Fl & Cl_{1-4} (125ms/10div)

FIG. 42. Saw-tooth wave form (0 to 4.5 volts) to voltage controlled oscillator (a), and frequency reference voltage (0 to 3 volts) for Fl and $Cl_{1\sim4}$ (b).

CR ladder circuits are fed back to two inputs of the balanced amplifier (TR_1 and TR_2) and the saw-tooth potential from VR_1 controls the gain of TR_1. The oscillation frequency is determined by the potential ratio of these two feedback signals, that is applied to the input transistor TR_3, as follows,

$$\frac{1}{2\pi RC\sqrt{6}}<f<\frac{1}{2\pi RC\sqrt{10/7}} \tag{3.6}$$

In this circuit, the oscillation frequency changes from 33 kHz to 47 kHz in accordance with applied saw-tooth potential change of 0 volt to 4.5 volts. This type of a phase shift oscillator is commonly used to generate the signal of frequency at VLF range. An advantage of this circuit is a high operation stability of generating frequency, while the disadvantage is in the distortion of the wave form to some extent compared with Terman oscillator and other sinusoidal wave oscillators. The output signal from this oscillator is reshaped to be sinusoidal wave form through the active wave filter (12 dB/Oct.).

X'tal OSC-3 The local oscillator is a Pierce-type crystal controlled oscillator, the generating frequency of which is 256.00 kHz and used for the reference signal of the frequency calibration circuit. The generated signal is also used as a local signal (32.000 kHz), that is fed to a mixer, being devided by 8 through 3-bit binary and the Schmitt trigger circuit.

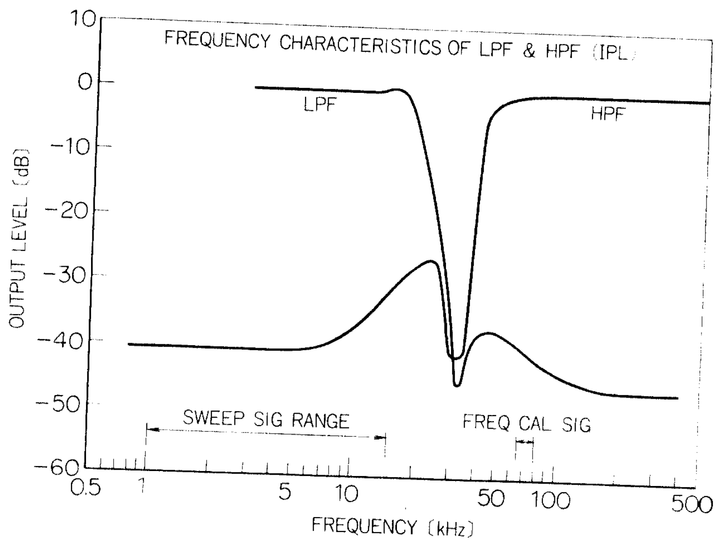

FIG. 43. Frequency characteristics of low-pass filter and high-pass filter; maximum attenuation frequency is 32 kHz.

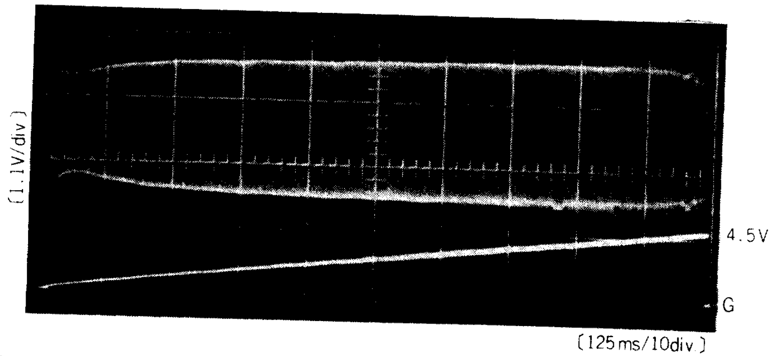

FIG. 44. Wave form of sweep signal output applied to antenna. The indent at the beginning of the sweep is due to the response of the voltage controlled oscillator to retrace of saw-tooth voltage. Saw-tooth wave form is superimposed (lower trace).

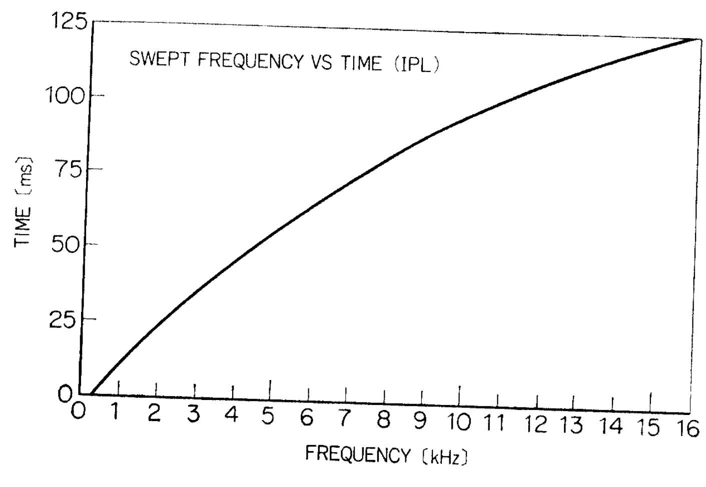

FIG. 45. Swept frequency versus time curve.

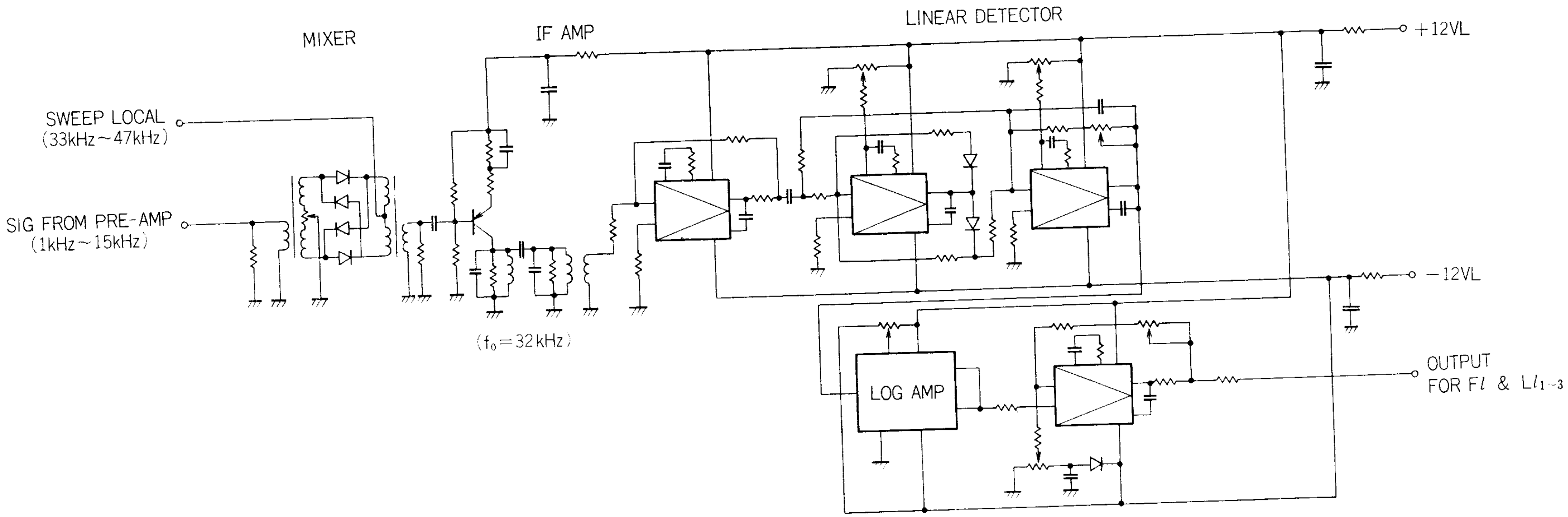

FIG. 46. IF amplifier and detector stage.

Mixer The mixer consists of a double balanced modulator which is used in IPH system (see III-3.2). As the frequency of the local signal is the same frequency of the center frequency of IF amplifier, the direct leakage of the local signal into IF stage from this mixer should be suppressed to be −54 dB, taking the balance of the mixer by the variable resistor that is located at the middle point of a primary coil of an output transformer (see Fig. 41).

LPF, HPF and Buffer AMP The output signal from the mixer contains two side bands. Each side band signal is separated through the low-pass filter and the high-pass filter. The lower side band (1 kHz to 15 kHz) of the signal is amplified to apply to the antenna and the frequency detection circuit. The upper side band (65 kHz to 79 kHz) of the signal is amplified to use for the frequency calibration. Figure 43 shows the frequency characteristics of both low pass and high pass filters. The frequency to give maximum attenuation in these filters is designed to be 32 kHz in order to eliminate the leakage signal of local frequency from the mixer. The wave form of swept signal to the pre-amplifier is illustrated in Fig. 44 and the characteristics of swept frequency versus time is indicated in Fig. 45.

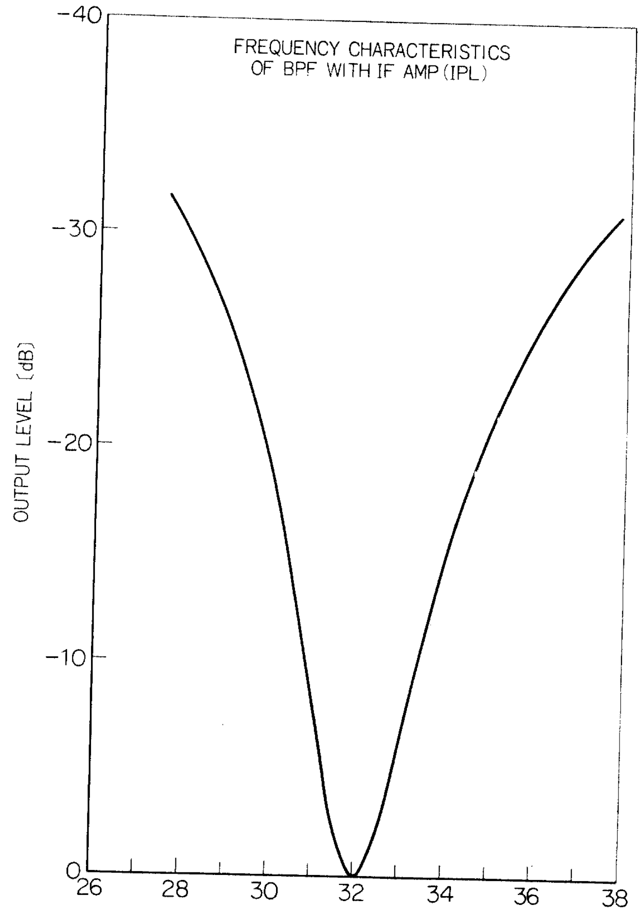

FIG. 47. Frequency characteristics of band-pass filter with IF amplifier.

4.2 Signal detection system

The output swept signal from the pre-amplifier is converted to the intermediate frequency signal (32 kHz) through the mixer. The signal from the mixer is fed to the IF amplifier; the output signal from the IF amplifier is rectified by the linear detector and compressed logarithmically. The circuits of this section is illustrated in Fig. 46. The basic system design of this circuits is the same as corresponding part of IPH, discussed in III-3.3. In this case, the leakage of local swept signal (33 kHz to 47 kHz) should be carefully eliminated by the double balanced modulator. The upper side band of output signal from the mixer should also be depressed by the double tuned selective amplifier with the band-pass filter designed to have the narrow pass-band characteristics (±600 Hz at −3 dB). This is illustrated in Fig. 47. The characteristics of inputs versus output of this circuit is shown in Fig. 48. The d.c. signal output from the logarithmic amplifier is applied to the frequency detection circuit for the lower hybrid resonance frequency Fl and to the sampling hold circuit for absolute values of impedance $Ll_{1\sim3}$.

4.3 Frequency detector for $Ll_{1\sim3}$ and $Cl_{1\sim4}$

To measure the antenna admittance level at fixed frequencies, the control signals to the sampling-hold circuit should be generated at the time when the swept frequency just coincides with a specified frequency. The frequency detector in this circuit, shown in Fig. 49, is a super-narrow band selective amplifier with a RC

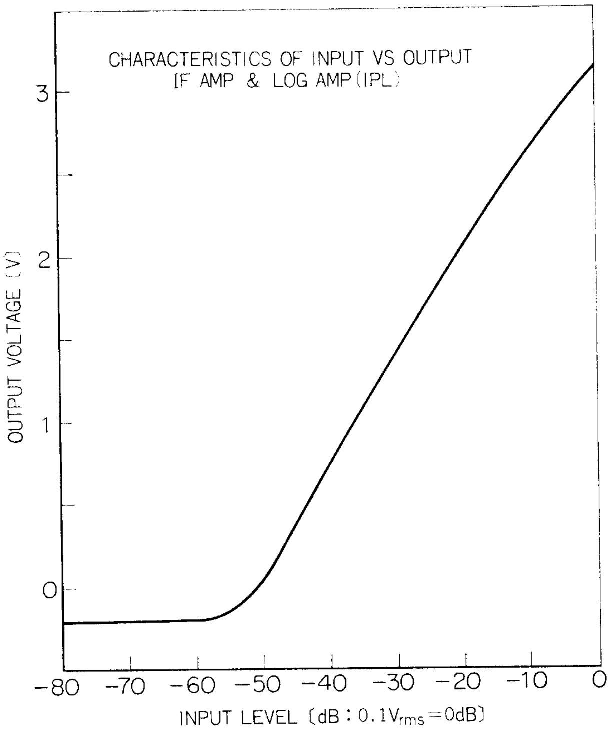

FIG. 48. Input versus output characteristics of logarithmic amplifier and IF amplifier. Dynamic range≃60 dB.

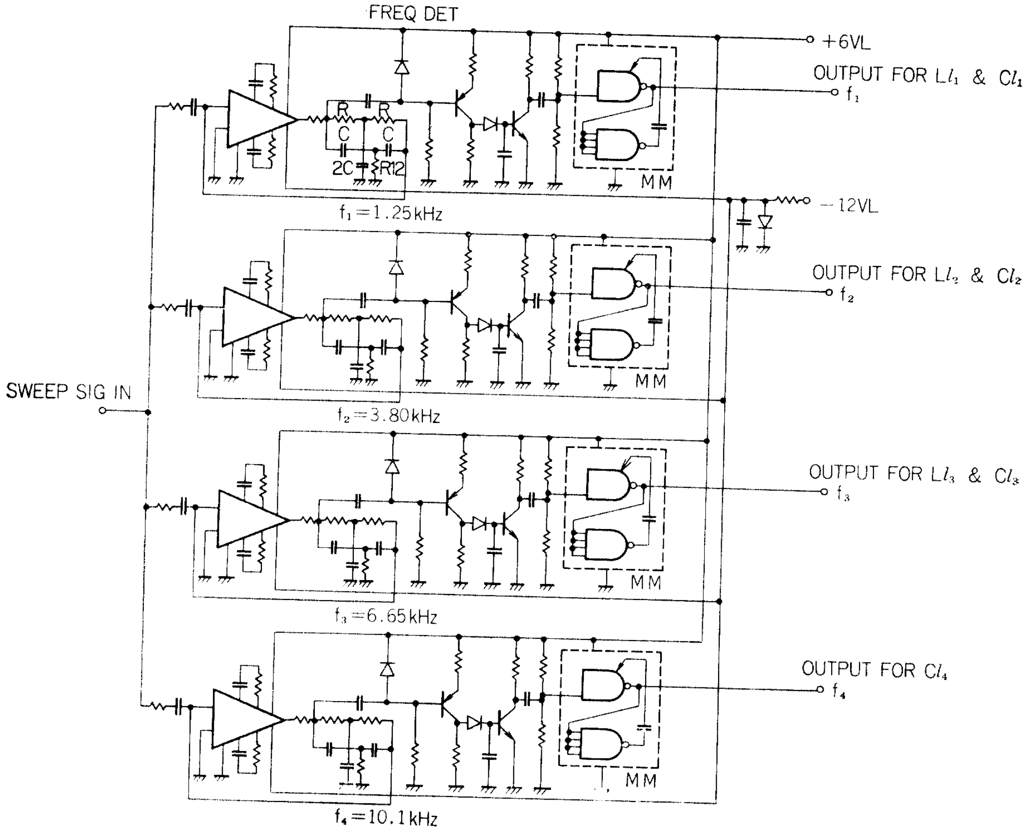

FIG. 49. Frequency detector ; center frequencies at 1.25 kHz, 3.80 kHz, 6.65 kHz and 10.1 kHz.

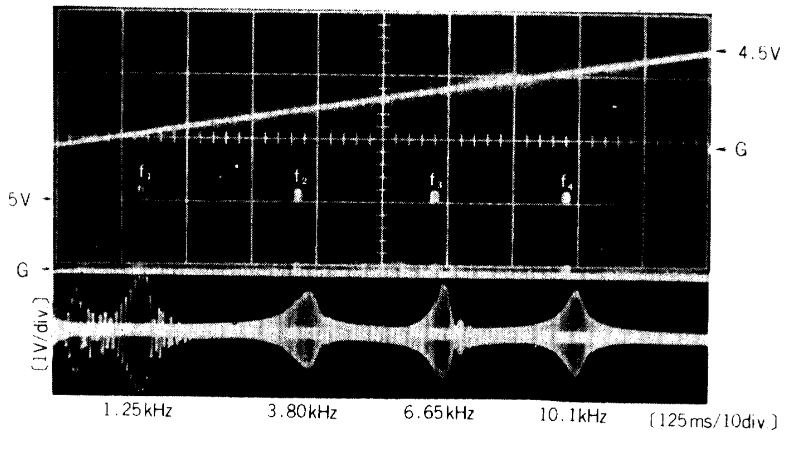

FIG. 50. Frequency detect pulse sequence, $f_1 \sim f_4$. ; lower trace is resonance wave form of the frequency detector.

twin T-section as a feedback circuit, each center frequency ($f_0 = 1/2\pi RC$) of which is designed to be 1.25 kHz, 3.80 kHz, 6.65 kHz and 10.1 kHz. The swept signal is amplified at these frequencies and rectified to give a trigger signal to the monostable multivibrator through the grounded-emitter amplifier. The output pulse width of the monostable multivibrator is 100 μs. Figure 50 shows the resonance wave forms at each above mentioned frequency and the sequence of the output pulses corresponding to frequencies given above.

4.4 *Lower hybrid resonance detector, sampling-hold circuit and data selector*

The basic concept of the circuit design of the resonance detector, the sampling-hold circuit, and the data selector is the same as corresponding circuits of IPH discussed in III-3.5. For detection of the lower hybrid resonance frequency, the output signal from the logarithmic amplifier is differentiated in terms of the time. This signal is formed as a detect pulse, through the monostable multivibrator, to feed to the data selector. The resonance frequency Fl and frequency calibration levels $Cl_{1\sim4}$ are expressed in terms of the saw-tooth voltage at the sampling time when resonances are detected, or the time when the signal frequency coincides with $Cl_{1\sim4}$. For the measurement of antenna admittance levels at 1.25 kHz, 3.80 kHz and 6.65 kHz, the output signal from the logarithmic amplifier is sampled at each corresponding frequency; the sampled data are stored until the read-in pulses of $Ll_{1\sim3}$ are applied to the gate control circuit. The function of data selector is to transform the time-parallel signal to the time-serial signal in accordance with the PCM time-sharing telemetry format for the detected frequency pulses $f_{1\sim4}$ and the resonance pulse. The circuit diagrams of this section are illustrated in Fig. 51.

Resonance Detector This circuit is designed to detect the lower hybrid resonance which has equivalent characteristics as a parallel resonant circuit. The circuit is almost the same as the case of the resonance detector used for the upper hybrid resonance detection (see III-3.5). The operation of this resonant detection function is given in Fig. 52; this is an example operated by a simulation dummy circuit for the antenna in a plasma, that consists of the parallel and series resonant circuit. The detected pulse at the resonance point is indicated, after reshaped by the monostable multivibrator, with the impedance value obtained from the logarithmic amplifier.

Sampling-Hold 2 and 3 The output signal from the logarithmic amplifier gives the absolute admittances; these absolute admittance values are sampled in accordance with the time-sequential gate pulses from the data selector and stored in the charging condenser at frequencies, 1.25 kHz (Ll_1), 3.80 kHz (Ll_2) and 6.65 kHz (Ll_3). The stored data are transmitted to ENC through the d.c. amplifier. The lower hybrid resonance frequency Fl is transmitted by corresponding potentials of the saw-tooth signal from VR_2. The calibration of this saw-tooth signal is made at frequencies, f_1, f_2, f_3 and f_4 that gives calibration levels Cl_1, Cl_2, Cl_3, and Cl_4. The input versus output characteristics of the sampling-hold circuits (HOLD 2 for $Ll_{1\sim3}$, and HOLD 3 for Fl and $Cl_{1\sim4}$) are given in Fig. 53. These function forms of input-output characteristics are used to obtain an accurate input signal level from observed data using the computer.

Data Selector The mode II$_2$ ($W_8 \sim W_{31}$) of the telemetry format is used for the IPL data transmission; the odd word numbers are used for the lower hybrid resonance frequency (Fl) and the frequency calibration levels ($Cl_{1\sim4}$), and the even

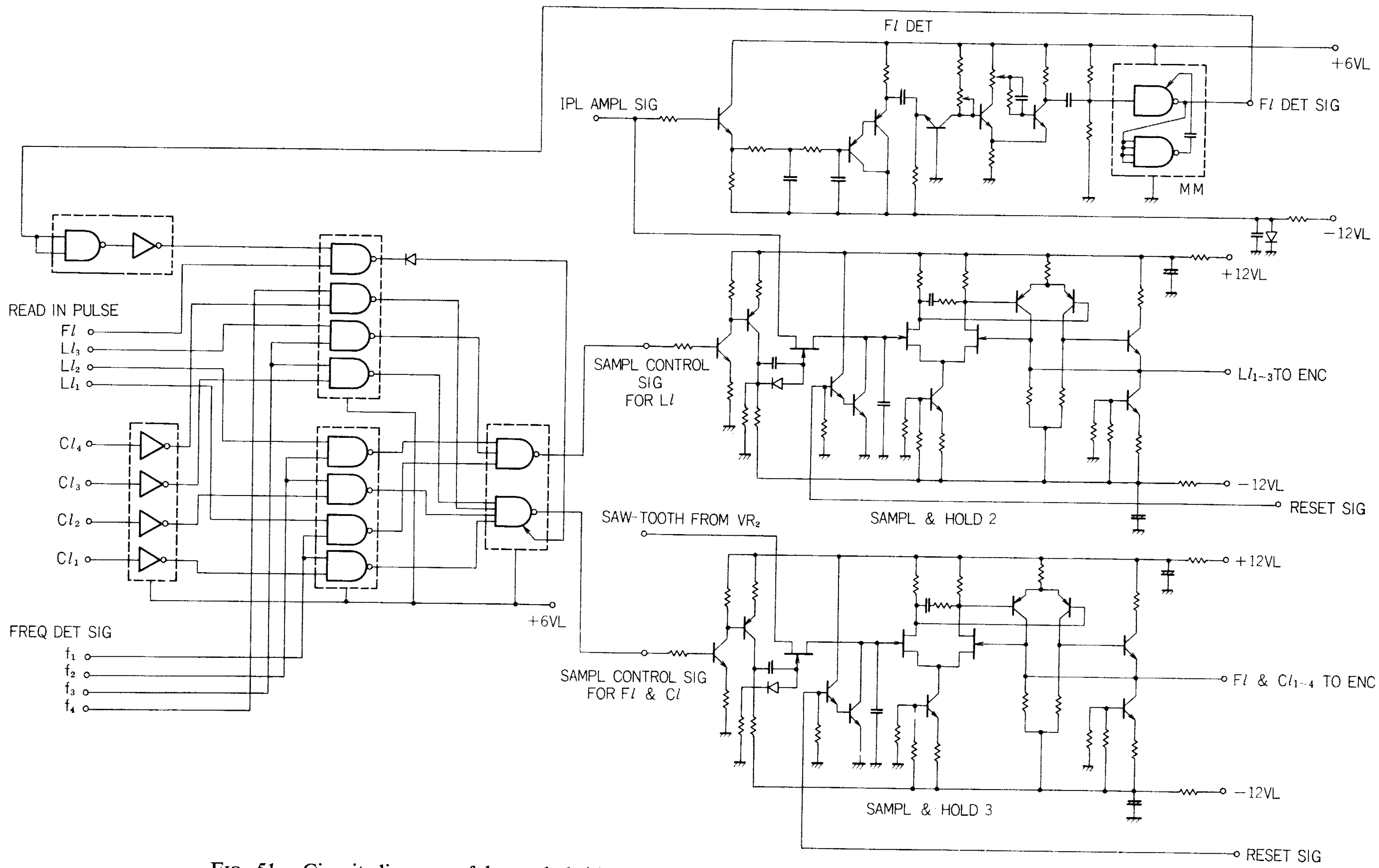

FIG. 51. Circuit diagram of lower hybrid resonance detector, sampling-hold circuit and data selector.

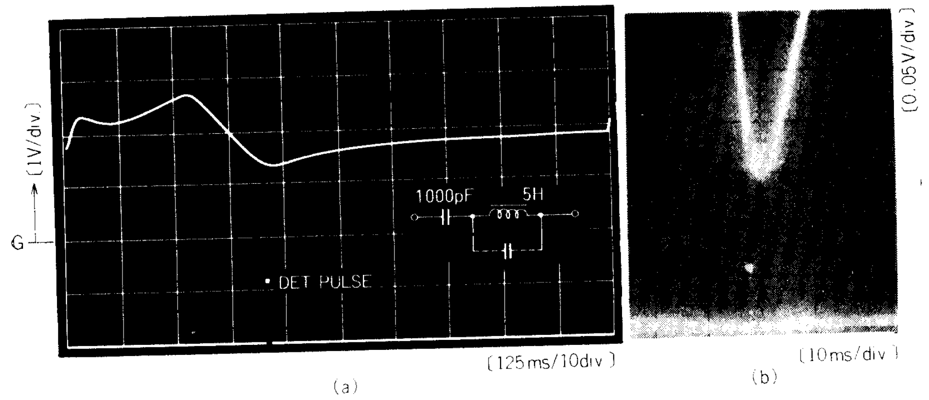

FIG. 52. Performance of resonance detector; output wave form from logarithmic amplifier (upper trace) and resonance detect pulse (lower trace). (b) enlarged a part of resonance of (a).

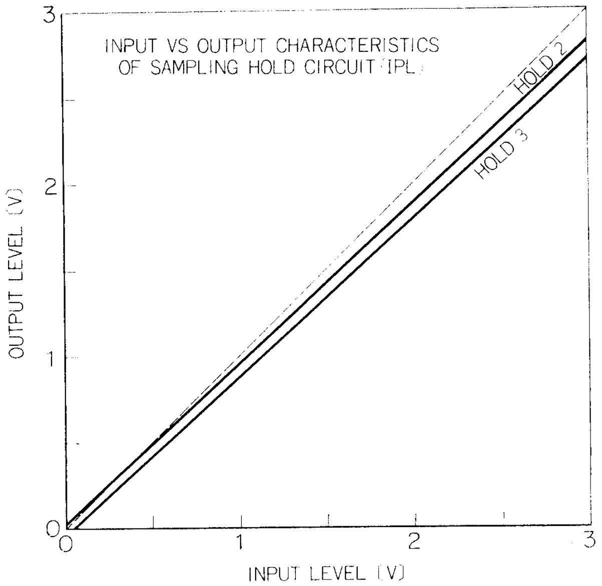

FIG. 53. Input versus output characteristics of sampling-hold circuit (HOLD 2 for $Ll_{1\sim3}$, and HOLD 3 for Fl and $Cl_{1\sim4}$).

word numbers are used for the admittance levels $Ll_{1\sim3}$. By using the data selector circuit with read-in signals of $Fl, Ll_{1\sim3}$ and $Cl_{1\sim4}$, time-parallel signals of the resonance detect pulse and frequency detect pulses $f_{1\sim4}$ are transformed to time-serial signal in accordance with the time-sharing telemetry format. The data are sampled and stored during one word before the assigned word.

III-5 Capacitance Bridge and Pre-amplifier

As has been previously noted, the gyro-plasma probe system has a capacitance bridge circuit with an antenna as one of the branch of the circuit. The unbalance potential produced between the other branch due to the variation of the antenna

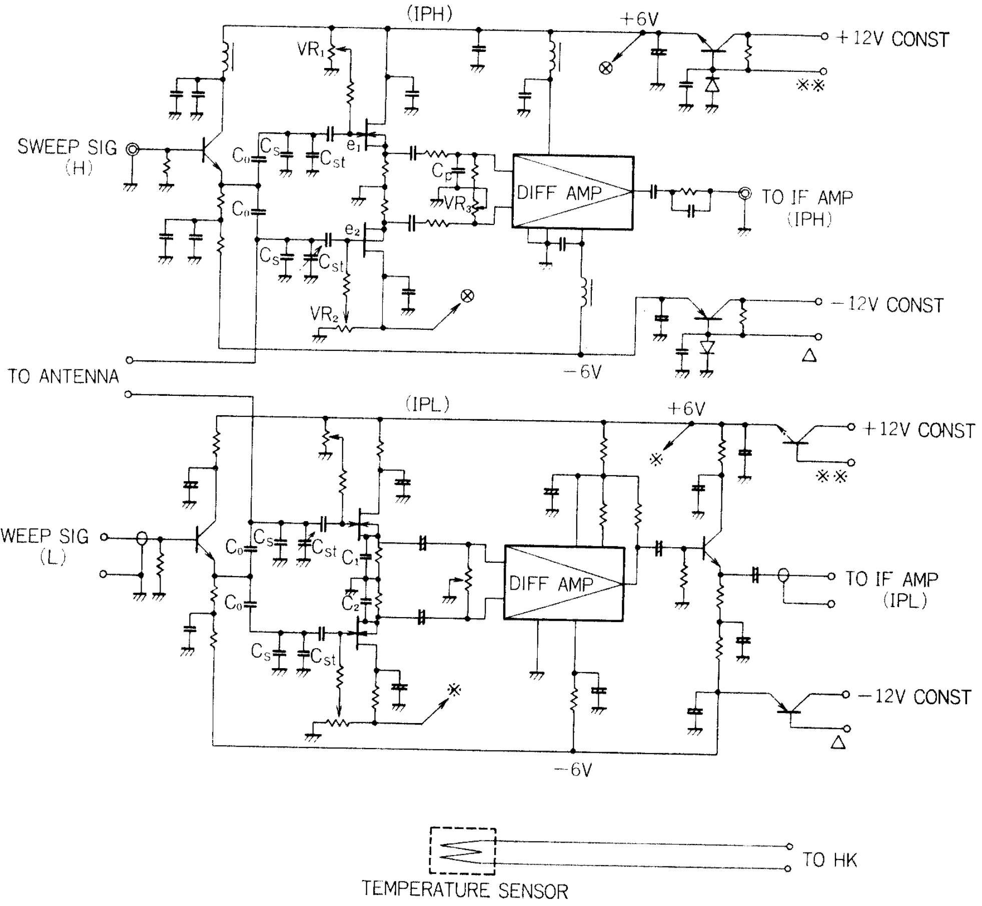

FIG. 54. Circuit diagram of pre-amplifiers of both IPH and IPL.

admittance as a function of the operating frequency is detected to give the absolute value of equivalent capacity (admittance value divided by the operating frequency). The rocket-borne gyro-plasma probe includes both amplitude and phase detectors to measure the vector impedance of an antenna. The satellite probe, however, does not include the phase detector circuit for restriction of allowed payload weight and limitation of the PCM telemetry system.

The circuit diagram of the pre-amplifiers is illustrated in Fig. 54. The pre-amplifier comprises the emitter follower circuit, the capacitance bridge, the buffer amplifier with high input impedance, the differencial amplifier and the antenna switching circuit (IPH and IPL, and CAL). To measure the temperature at the moment of operation, the temperature sensor of platinum wire is allocated in this pre-amplifier. The detected temperature signal is treated by the house keeping instrument (HK channel #18) and transmitted through the telemetry system.

IPH Pre-AMP The swept signal from the part of swept signal generator is applied through the 50 Ω coaxial cable to the emitter follower circuit (buffer amplifier) with the input impedance of 50 Ω and the output impedance less than 10 Ω. The IPH system is designed to have the dynamic range from 1 pF to 1000 pF for the measurement of the equivalent capacitance. The value of the capacitor C_0

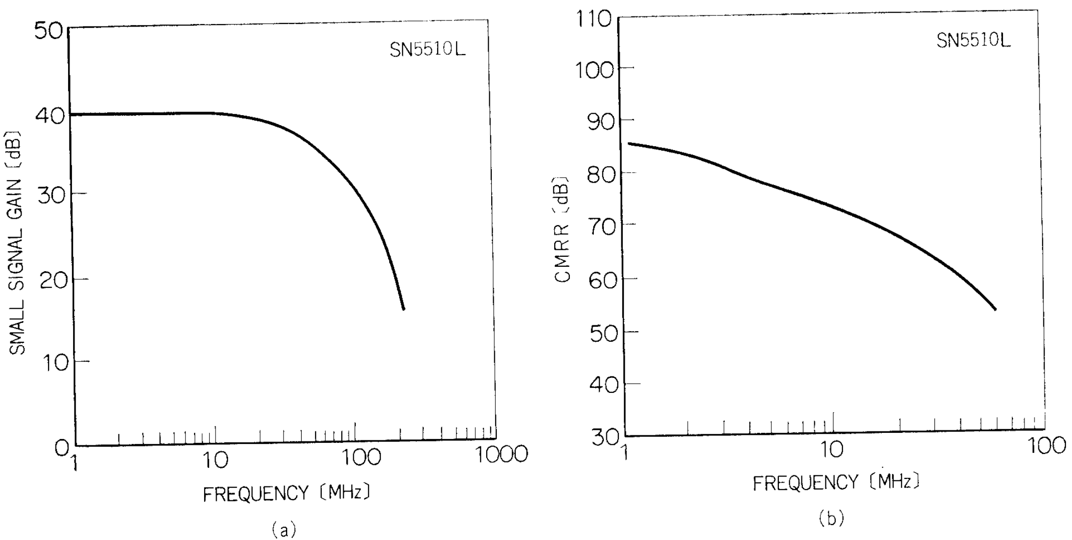

FIG. 55. Typical characteristics of wide band video-amplifier, SN 5510 L; (a) small-signal voltage gain versus frequency, and (b) common-mode rejection ratio versus frequency.

is 1000.0 pF and the stray capacity of the cable is 57 pF, which can be cancelled by adjusting the values of the capacitors C_s, C_{st} and C'_{st}. The outputs e_1 and e_2 (as shown in Fig. 54) from the capacitance bridge are applied to the source follower FET amplifiers that have high input impedances (10 MΩ/12 pF). The balance ratio of the capacitance bridge, that is defined by the difference of the amplification of two FET source followers and the common mode rejection ratio of the differential amplifier should be less than about −60 dB (1/1000). Adjustment of the amplitude of signal in these two channels is made by the variable capacitor C'_{st} and the variable resistor $VR_{1\sim3}$; and the phase difference through these channels is adjusted by the capacitor C_p. The differential amplifier used in the IPH is the wide-band video-amplifier SN5510L (TEXAS Inst.) which has a constant gain and low phase-shift versus from d.c. to 40 MHz as has been illustrated in Fig. 55(a). The common mode rejection ratio (CMRR) is given in Fig. 55(b).

IPL Pre-AMP The principle of circuit design is much the same as the case of the IPH pre-amplifier. In this system the values of capacitors C_0 and C_s are chosen to be 10000 pF and 100 pF, to obtain the dynamical range of equivalent capacitance from 30 pF to 10000 pF. The phase difference of two differential amplifier channels is adjusted to be minimum shift angle by the capacitors C_1 and C_2. The differencial amplifier used in the IPL is TA7034MJ (TOSHIBA) which has a gain of 16 dB, a low NF (Noise Figure) of 7.8 dB at 100 MHz and CMRR of −110 dB at 1 kHz.

ANT Switching CIR A monopole antenna is used for the sensor of high and low frequency gyro-plasma probes, and switched alternately being synchronized with the telemetry time-sharing period. The antenna switching circuit as shown in Fig. 56

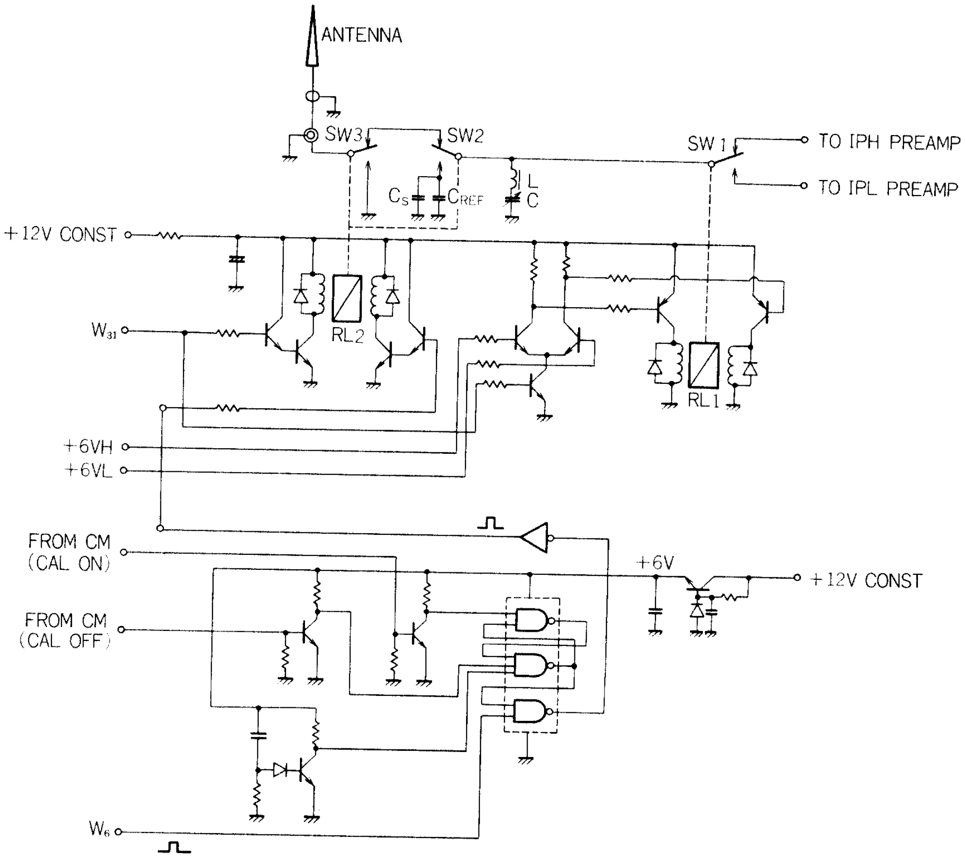

FIG. 56. Antenna switching circuit.

selects the antenna for IPH and IPL pre-amplifiers (SW 1), and also this circuit comprises the switching operation to earth connecting circuit (SW 3), and the capacitance calibration circuit (SW 2). A trapping circuit to shunt the carrier from UHF 400.5 MHz transmitter to avoid the interference has also been included.

The switch SW 1 is operated by the relay RL 1 that is drived by the gate pulse W_{31} and the power supplies of +6 VH and +6 VL from the PSW (Power switch of the spacecraft) corresponding to the telemetry mode II_1 and II_2. The gate pulse W_{31} is an end mark of each mode so that SW 1 is switched from IPH to IPL after all the observation of mode II_1 (IPH), and vice versa.

The switches SW 2 and SW 3 are operated by the relay RL 2 that is drived by the gate pulses W_{31} and W_6. When the gate pulse W_6 drives the relay RL 2, both SW 2 and SW 3 connect the line to the antenna. When the gate pulse W_{31} is applied, SW 2 connects the line to the reference capacitor C_{REF} and C_s. The switch SW 3 connects the antenna to the ground. The antenna is connected to the pre-amplifier only during the observation of IPS, i.e. from W_6 to W_{30}, to protect the FET transistors of the pre-amplifiers from the damage due to high voltage inputs, that may possibly be transmitted from the cyclotron instability experiment (CIE). The CIE equipment is designed to radiates the electromagnetic wave with high voltage (about 1200 Vpp) at frequencies of 120 kHz to 210 kHz from a horizontal loop antenna (see Fig. 65).

The calibration of operating level for the instrument is performed by using the reference capacitor (C_{REF}). The operation to switch C_{REF} by SW 2 is controlled by command (PI CAL ON and OFF). When the "CAL ON" pulse is applied, the gate pulse W_6 is inhiibted to drive the relay RL 2. Consequently, SW 2 remains at the side of the reference capacitor, and the pre-amplifier with the capacitance bridge detects the fixed value of C_{REF} (100 pF). C_s is used to compensate a stray capacitance of the cable that is extended from the position of SW 2 to the antenna.

Since the antenna of the UHF 400.5 MHz transmitter is located just above monopole antennas, the induced potential on the antenna is rectified through the nonlinearity of the circuit and the modulation signal (768 Hz square wave for the real-time mode telemetry transmission) is superimposed on wave from of IPS signal. In order to avoid this interference a trapping circuit is installed. It consists of the LC series resonator which is tuned to the frequency at 400.5 MHz. The admittance of this circuit in the frequency range less than 15 MHz takes capacitive value that is low enough not to disturb the observation value.

III-6 Frequency Calibration and Data Processing Sub-systems

Frequency Calibration Circuit For the purpose of monitoring the circuit operation in orbit, the command system is employed and controls onboard calibration circuits. One of control items is the frequency calibration of IPS; the frequency of the crystal controlled oscillator for the gate width control circuit of IPH and the swept frequency of IPL. These signals are transmitted by a UHF 400.5 MHz telemetry system (IRIG band #10; 5.4 kHz±7.5%). The circuit of this system is illustrated in Fig. 57.

Frequency calibration signals from IPH (101.5625 kHz) and IPL (65 kHz~79 kHz) are switched by the timing signal (+12 VH and +12 VL) that is fed from PSW (Power Switch). Each signal is mixed with the reference signal (256.00 kHz) to convert the signal frequency into the modulation frequency band. The selective amplifier is used to eliminate the lower side band of mixed signals; obtained upper side band frequencies are 357.5625 kHz for IPH,and in a range from 321 kHz to 335 kHz for IPL. These obtained signals are reshaped by a saturation amplifier to be the rectangular wave form as shown in Fig. 58. The output signal is demultiplied by 64 through binary circuits to obtain final signal frequencies for the telemetry at 5.587 kHz for IPH and in a range from 5.016 kHz to 5.234 kHz for IPL.

Data Processor The data processing equipments consist of onboard and ground-based systems. The data processor, onboard the spacecraft, is designed to generate gate control pulses that are required for data selector which controls the data sample due to time-sharing program of the telemetry. The assembly of functional elements is illustrated in Fig. 59; this logical operation circuit is controlled by pulses from the TIM-ENC. The time sequence of input pulses are given in Fig. 60. G_0 is a pulse corresponding to frame synchronous word and $G_{1\sim 6}$ are used to make 6 groups, for $W_2 \sim W_{31}$, in which 5 words are included. For example, the word

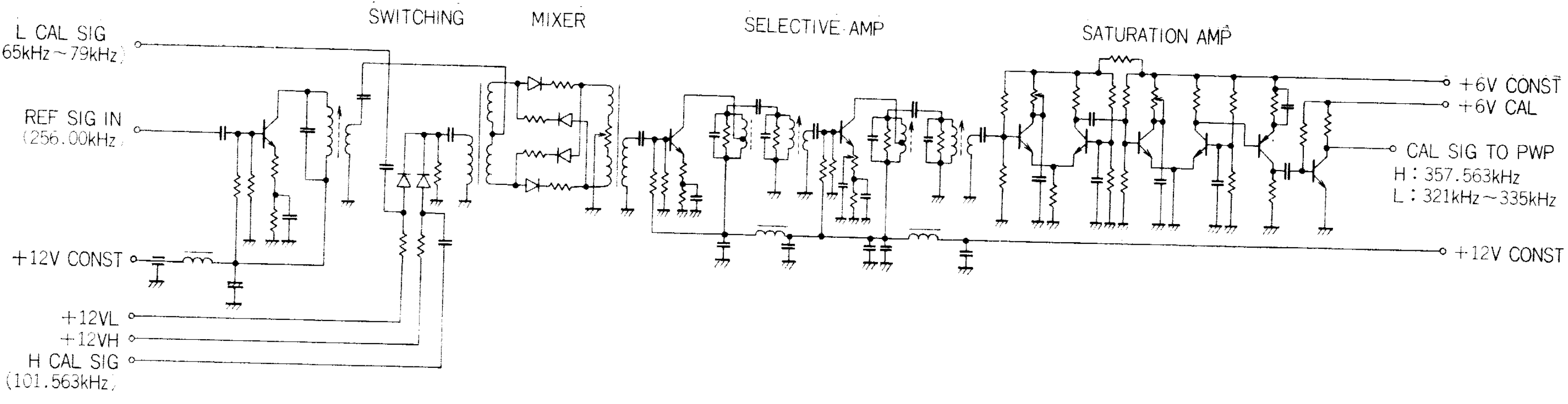

FIG. 57. Frequency calibration circuit.

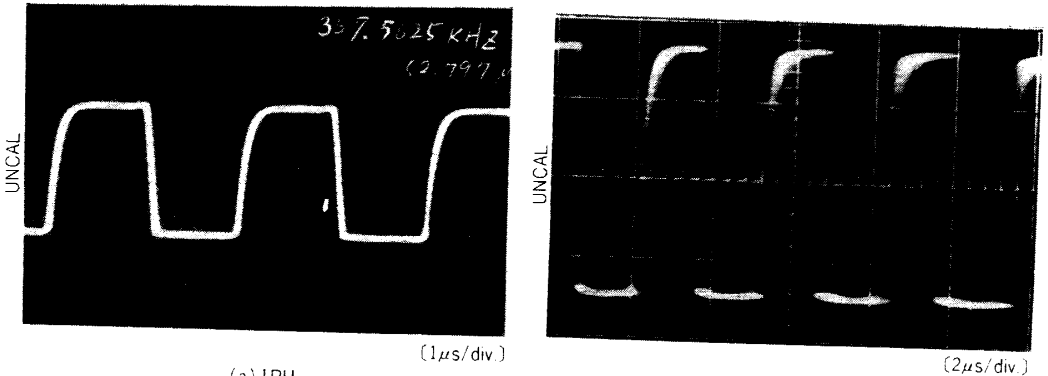

(a) IPH

(b) IPL

FIG. 58. Output wave form of frequency calibration of IPH (a) (fixed frequency of 357.5625 kHz) and IPL (b) (swept frequency of 321 kHz to 335 kHz).

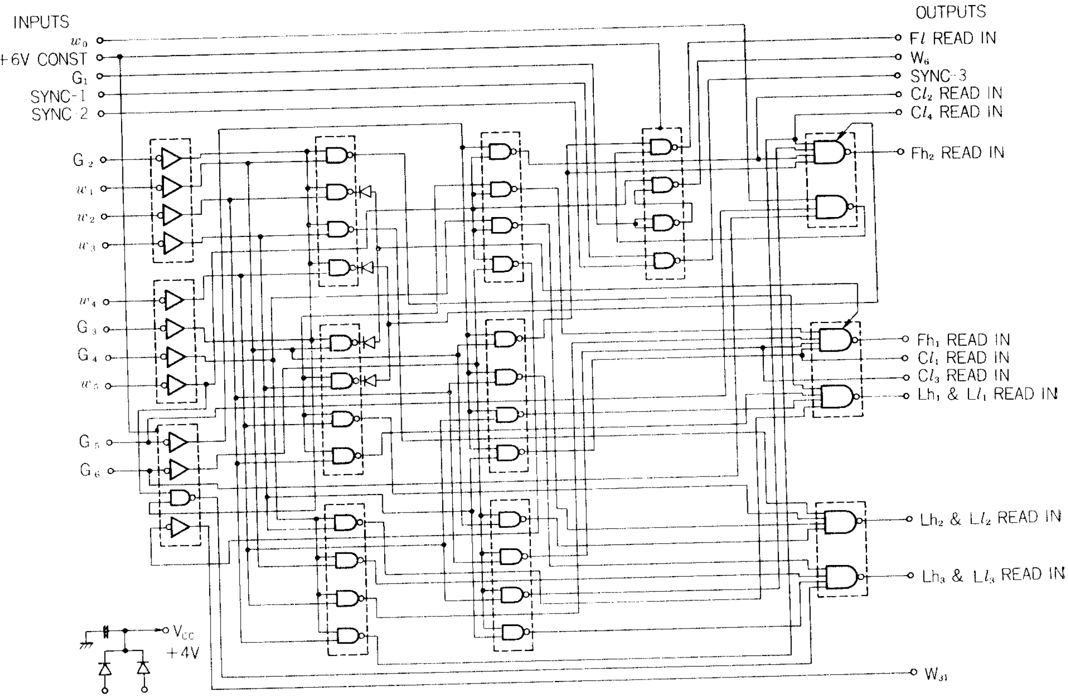

FIG. 59. Functional operation diagram of data processor; integrated circuits, HD 203F and HD 204F, are used.

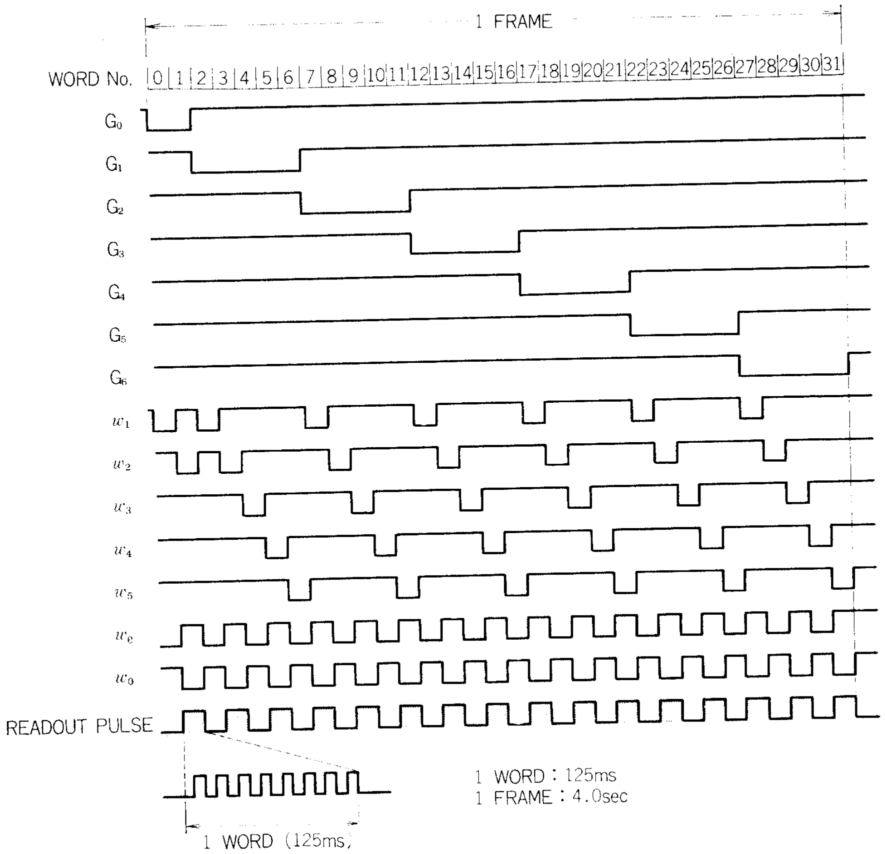

FIG. 60. Pulse sequences from TIM-ENC.

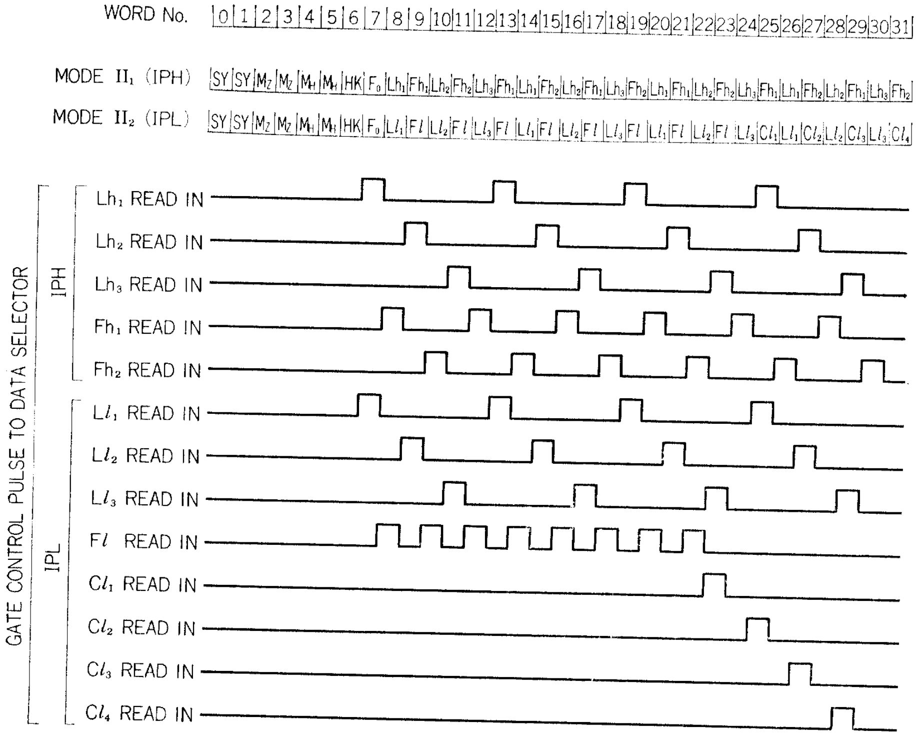

FIG. 61. Pulse sequences from TIM-ENC.

pulse W_{13} can be obtained as a result of logical operations, $\overline{G_3} \cdot \overline{W_2}$. The produced read-in pulses for observation items (Fh_1, Fh_2, Lh_1, Lh_2, Lh_3 for IPH and Fl, Ll_1, Ll_2, Ll_3, $Cl_{1\sim 3}$ for IPL; see III-2) are shown in Fig. 61. These reading-in pulses are applied to the data selectors of IPH and IPL at the time advancing one-word period before the assigned word number, as has been explained previously in III-3 and III-4. Input pulses SYNC-1 and 2 generated from w_o and w_e produce the timing pulse SYNC-3 which is applied to the saw-tooth generators of IPH and IPL, and these three pulses are used as reset trigger pulses. The pulses for W_6 and W_{31} are used for the set and reset operations of the antenna switching circuit.

The so-called "Quick-Look" instrument is prepared to check the telemetry data quickly on the real-time base. The main quick-look instrument sorts the time-serial PCM signal into the each corresponding frame mode. The sorted PCM signals are converted into the analog signals through the D/A converter. The IPS quick-look sorts the time-serial data of mode II_1 and II_2 into six parallel channels corresponding to observational items, Fh_1 and Fl, Fh_2 and Fl, Lh_1 and Ll_1, Lh_2 and Ll_2, Lh_3 and Ll_3, and $Cl_{1\sim 4}$. The circuit of the gate control signal generator is shown in Fig. 62. Input pulses of the frame synchronous, bit and word identification signals are supplied from the main quick-look to this IPS quick-look circuit. Generated pulse sequences to control the gate circuit of IPS quick-look are summarized in Fig. 63. These gate pulses are applied with the delay one word period from the assigned word number, because of the time delay of the D/A converter and hold circuits. The signal is sampled by gate control pulses and fed to

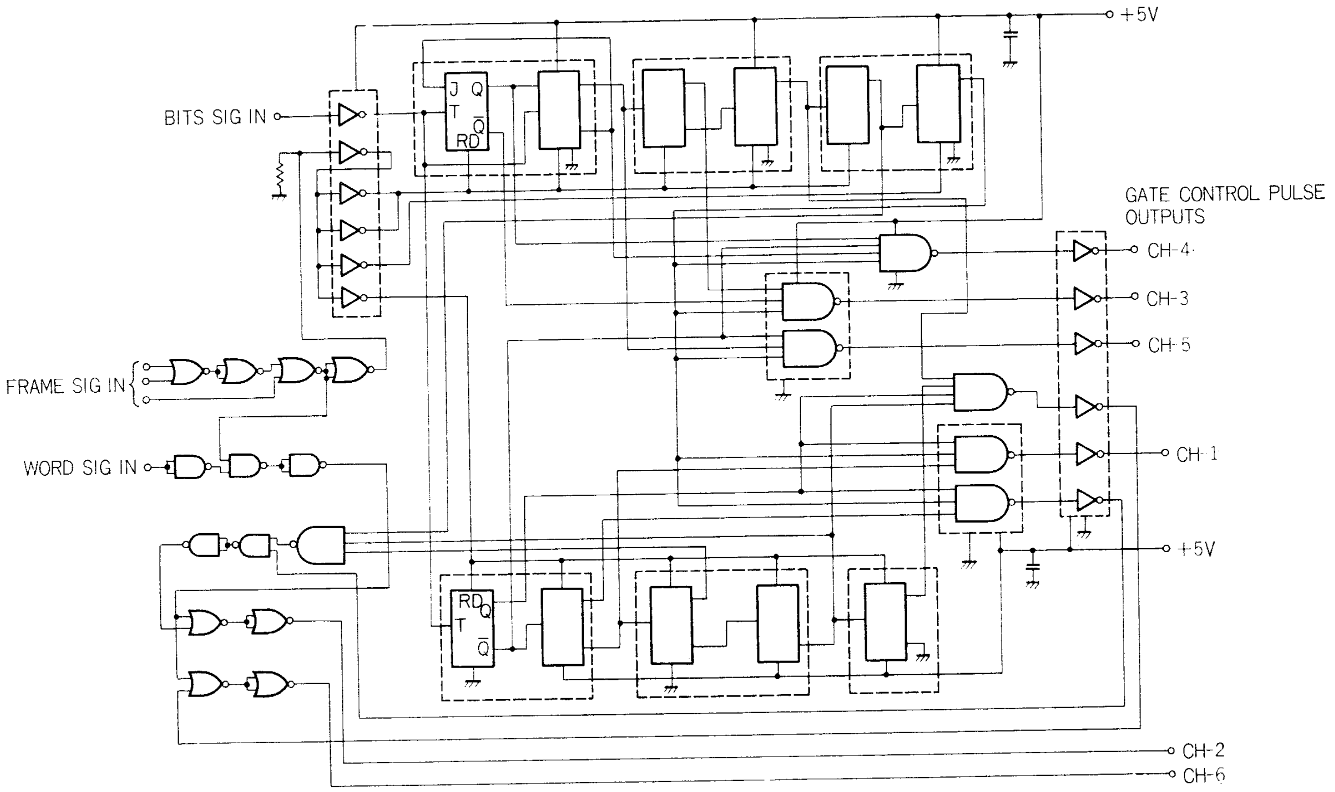

FIG. 62. Functional block diagram of ground-based data selector.

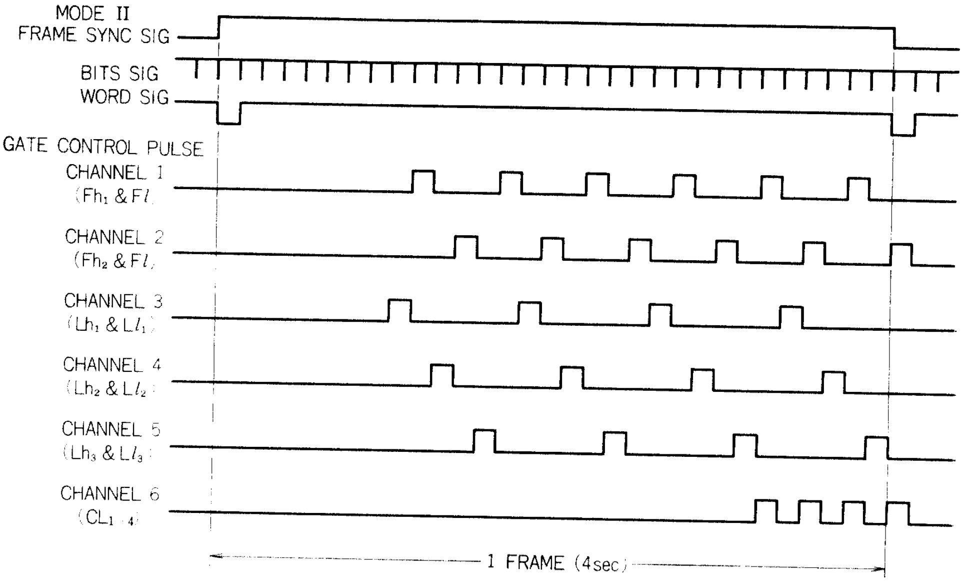

FIG. 63. Gate control pulse sequences of ground-based data selector.

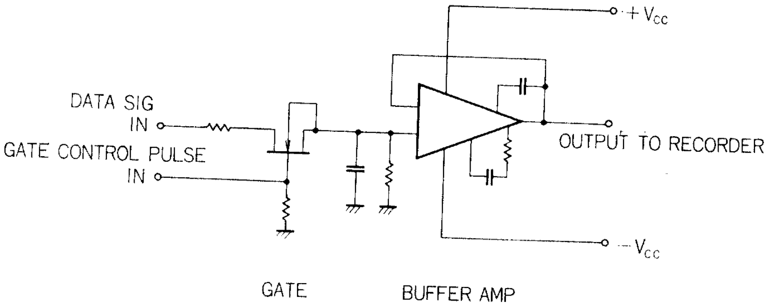

FIG. 64. Electrical circuit of gate and buffer amplifier.

the pen recorder with six channels through the buffer amplifier and d.c. amplifier. An example of one unit circuit of the gate and buffer amplifier is illustrated in Fig. 64.

III-7 Construction of Payloads and Antenna Sub-system

The REXS satellite has three monopole antennas and two orthogonal loop antennas (Fig. 65). One of the monopole antennas is used as a sensor of the gyro-plasma probe, which is a thin flat strip of spring steel (beryllium copper) preformed into a cylindrical tube with an overlapping seam. The tube is subsequently opened flat and wound onto a drum for storage purposes. When the strip is released from its storage drum, the strip curls into its preformed shape to form a tube with considerable bending strength. The diameter is 10 mm, and the length from root to tip are movable with three steps of length (60 cm, 123 cm and 205 cm). When the satellite is separated from the 4th stage rocket motor, the antenna begins to extend with a speed of 5 cm/sec being controlled by a pre-set timer. The command system is able to control the extension and retraction of

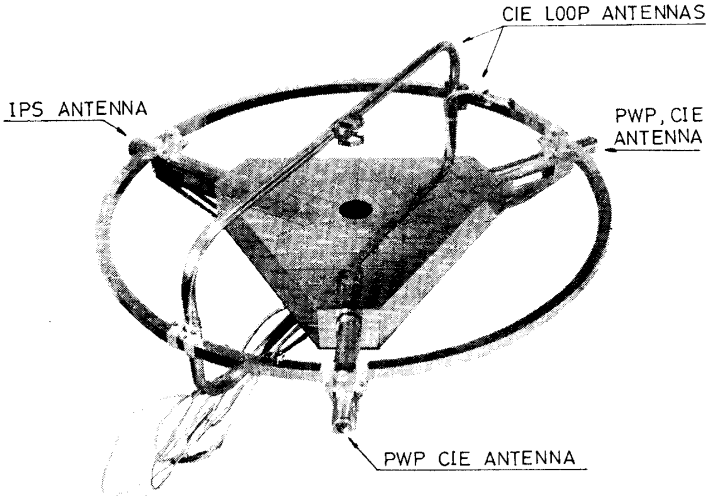

FIG. 65. Structure of three monopole antennas and two loop antennas.

antennas at every step. The capacitance of fully extended antenna in free space is calculated to be 26 pF, which agrees well with the measured value of the gyro-plasma probe (Lh_3=110 decimal counts).

The main package of IPS instrument and its pre-amplifier are shown in Fig. 66 (a) and (b). The main package is mounted on the flat aluminium-honeycomb plate of the spacecraft deck. The pre-amplifier is installed in the central tube. To protect from the damage due to vibration, shock, and heat in vacuum condition, all circuits are encapsulated with a polyurethane foam-in-place resin that is called Eccofoam FPH. To protect against temperature increment, a thermal barrier of aluminium foils is muffled around the main instrument. The covering-case of the pre-amplifier is painted black for the thermal coupling between the pre-amplifier and instruments of the spacecraft because of its small heat capacity.

Standardized pre-flight test conditions for the mechanical and thermal environment of instruments are summarized in Appendix B.

III-8 Summary of IPS Instrument

The gyro-plasma probe has been designed and developed for the instrument onboard the spacecraft. A number of improvements and re-constructions of electrical circuits and mechanical structures have been made after various operational tests. Adequate operational performances of electrical circuits of both high and low frequency gyro-plasma probes are obtained.

The total weight of the main instrument is 3.642 kg and that of the pre-amplifier is 0.434 kg. The required electrical power is summarized in Table 3. As one period of 32 frames contains twelve frames of IPS mode, the use-time ratio of IPH and IPL is 0.1875 (=6/32). The average electrical power consumption is 2.299 watts for the normal mode and 2.449 watts for the calibration mode (PI CAL ON).

Reliability of the instrument should be studied and considered critically because

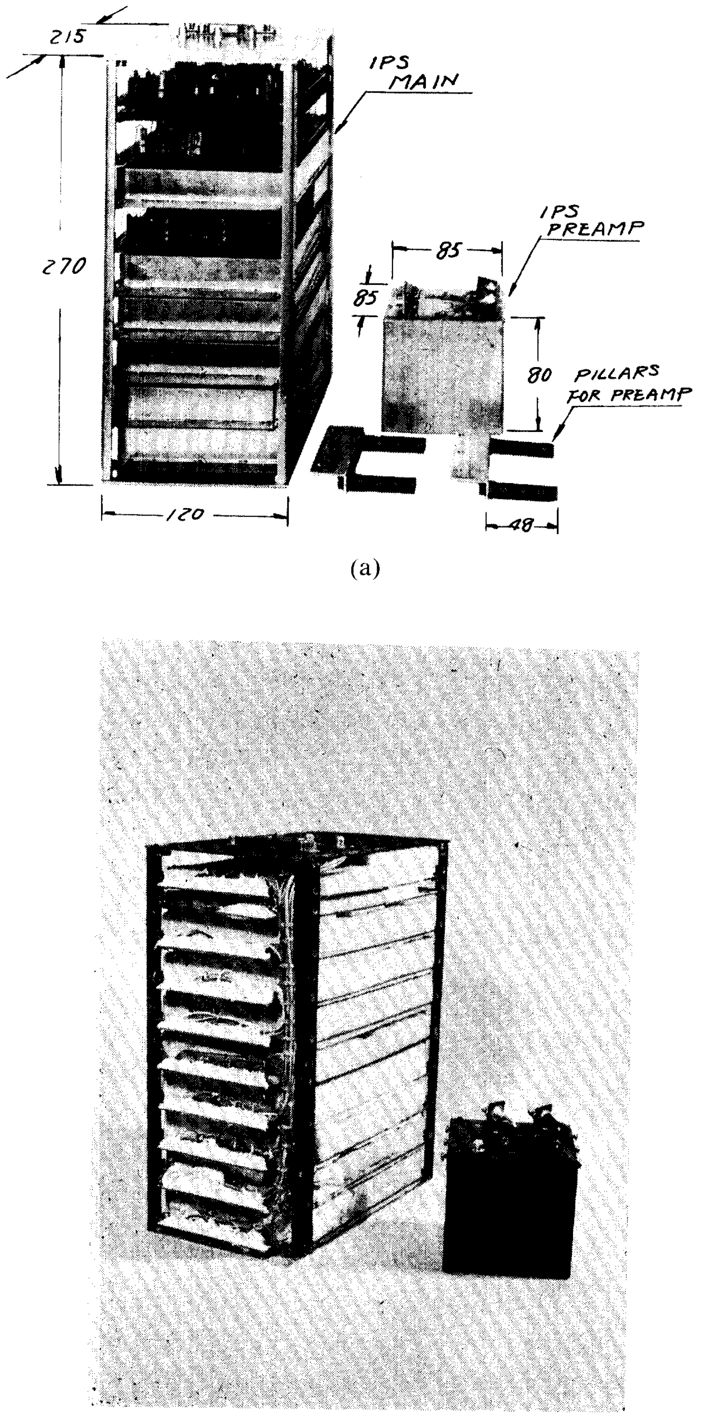

(a)

(b)

FIG. 66. Main instrument of gyro-plasma probe and its pre-amplifier; (a) before and (b) after encapsulation.

it is unable to repair or operate the instrument except some controlled items by command after the spacecraft launching. The reliability R is expressed as a function of time t,

TABLE 3. Electrical power consumption of gyro-plasma probe.

Mode	+12 V	+6 V	+4 V	−12 V	Total	×0.1875
Continuous	70 mA	—	—	30 mA	1.20 W	—
IPH	205 mA	150 mA	35 mA	25 mA	3.80 W	0.713 W
IPL	30 mA	120 mA	35 mA	70 mA	2.06 W	0.386 W
CAL	—	25 mA	—	—	0.15 W	—

$$R=\exp(-k\lambda Nt/10^9), \qquad (3.7)$$

where k is the coefficient of severity, $\lambda=1/\mathrm{MTBF}$ in 10^9 fits (MTBF is the mean time between failures), N the total number of the parts, and t the time duration in hour. As the instrument comprises different kinds of parts, the λN is written as

$$\lambda N \equiv \sum_i \lambda i\, Ni. \qquad (3.8)$$

Values of λi and Ni are summarized in Appendix C. The total number of parts used in the IPS is 1438 and that of the soldering points is 3969. The summation products of λ_i and N_i becomes 27007.5. If k might be unity (for the most mild condition), the reliability R of IPS is computed to be 0.9433 for an interest life of three months.

IV. PRE-FLIGHT TESTS OF INSTRUMENT

The instruments onboard the spacecraft should be subjected to pre-flight tests of electrical and mechanical performances under various phase of the spacecraft mission. Pertaining to these tests, operational characteristics of the instrument has been given, using the electrical simulation circuits for the antenna in a plasma. The test for heat effects in vacuum and the space plasma simulation experiment were also carried out. The calibration data for all observation items were obtained.

IV-1 Operational Characteristics

The admittance of a combined electrical circuits that consists of the series parallel resonant circuit shows the similar frequency characteristics with the antenna in a plasma, when the proper values of resistance, inductance and capacitance elements are used (see Fig. 69).

IPH The measured admittance value (the output of logarithmic amplifier) versus frequency is illustrated, in Fig. 67, in terms of the equivalent capacitance. The peak of the wave form appeared at higher frequency side, is due to a resonance like phase variation in the characteristics of the pre-amplifier circuit. The frequency dependence of amplitude is mainly due to the amplitude variation of the sweep signal versus frequency that is applied to the antenna. The measured values of equivalent capacities at 300 kHz (Lh_1) and 13 MHz (Lh_3) are given in terms of

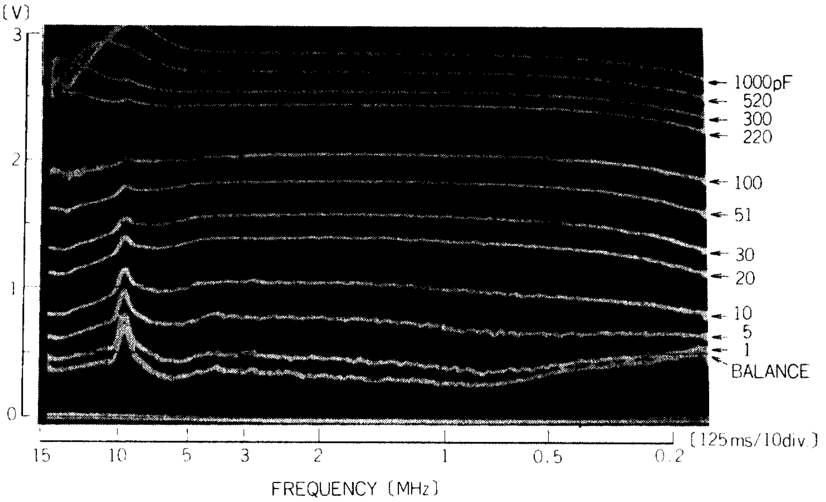

FIG. 67. Equivalent capacitance versus frequency characteristics of output from logarithmic amplifier (IPH).

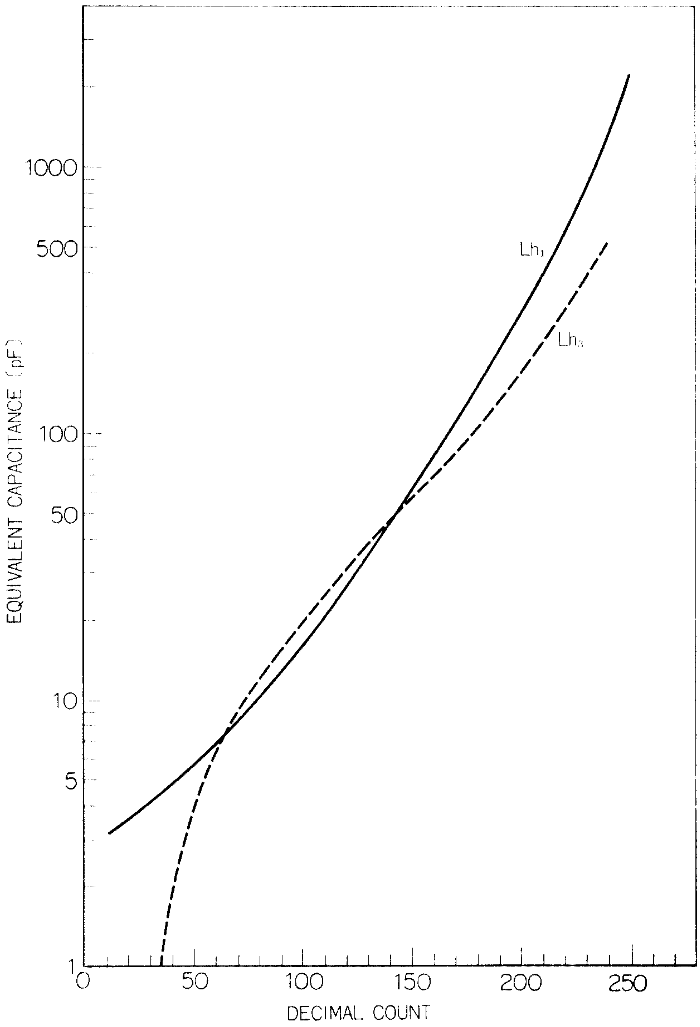

FIG. 68. Equivalent capacitance versus output decimal data (Lh_1 and Lh_3) through sampling-hold circuit and A/D converter of telemetry system.

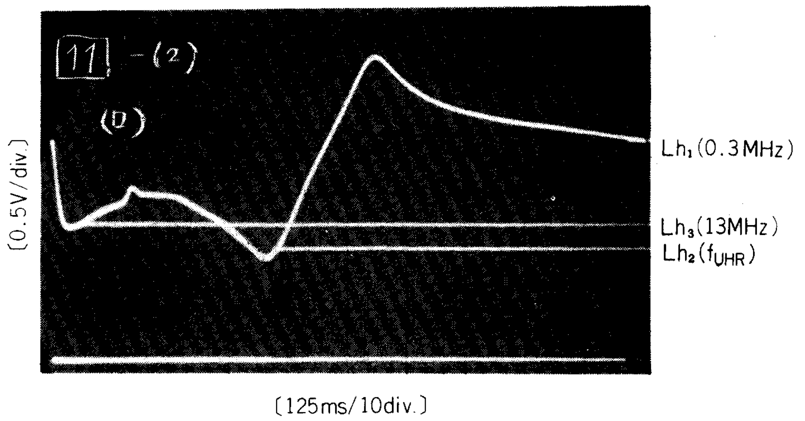

FIG. 69. Sampling-hold performance. Corresponding to 0.3 MHz, f_{UHR} and 13 MHz, frequencies are detected and potentials (Lh_1, Lh_2 and Lh_3) are sampled and stored. Output wave form of logarithmic amplifier is superimposed. Dummy antenna circuit $C_0\langle\frac{L}{C}\rangle$ (L=100 μH, C=30 pF, C_0=100 pF and damping resistor of 5.1 kΩ) are used.

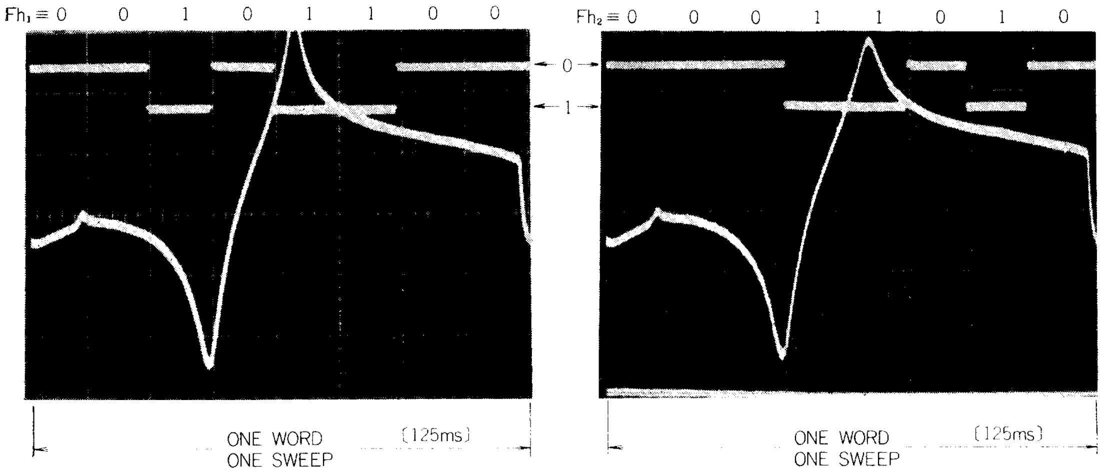

FIG. 70. Resonance frequency detection; (a) output of Fh_1 is 00101100 (binary)=44 (decimal) which is equal to 2.23 MHz, and (b) output of Fh_2 is 0011010 (binary)=26 (decimal) which is equal to 1.32 MHz. Output wave form of logarithmic amplifier is superimposed (Vertical: 0.5 V/div.). Dummy antenna circuit (L=100 μH, C=15 pF and C_0=100 pF) are used.

PCM count in Fig. 68. These results are obtained through the over all system of instruments. The detection function at $Lh_{1\sim3}$ are examined using a simulation circuit (L=100 μH, C=30 pF and C_0=100 pF) as given in Fig. 69. The output levels Lh_1, Lh_2, and Lh_3 from the sample-hold circuit are compared with the total admittance level from the logarithmic amplifier being superimposed in a dual trace oscilloscope. Detections of resonance point frequencies at Fh_1 and Fh_2, are checked by a simulation circuit with parameters as L=100 μH, C=15 pF and

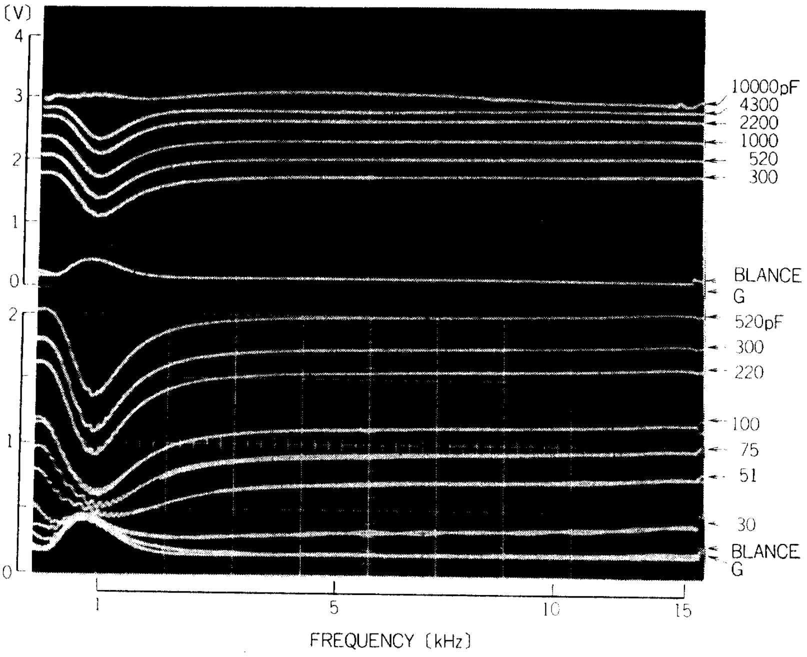

FIG. 71. Equivalent capacitance versus frequency characteristics of output from logarithmic amplifier (IPL).

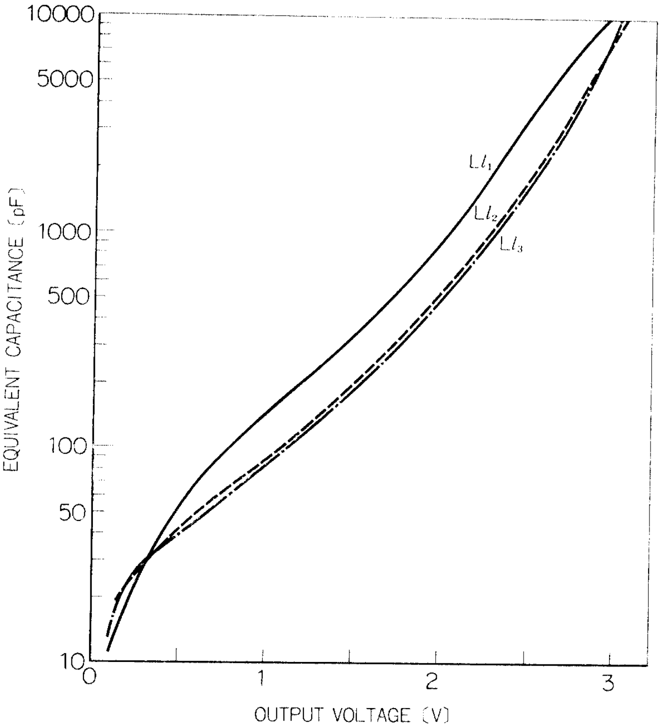

FIG. 72. Equivalent capacitance versus output decimal data (Ll_1, Ll_2 and Ll_3) through sampling-hold circuit and A/D converter.

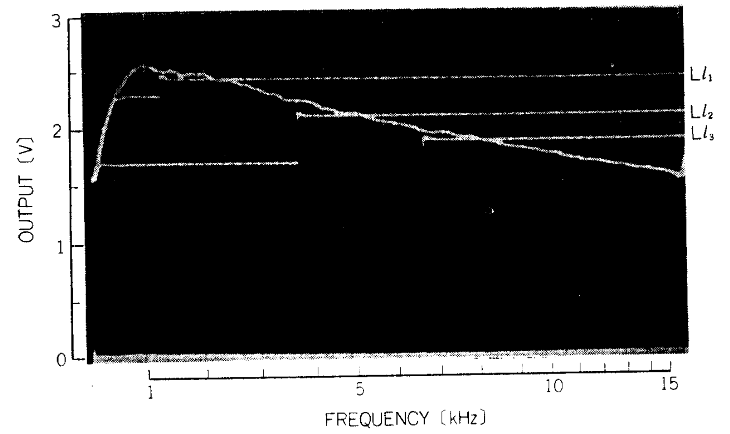

FIG. 73. An example of sampled and stored levels of Ll_1, Ll_2, and Ll_3 ; frequency spectrum of admittance level is superimposed.

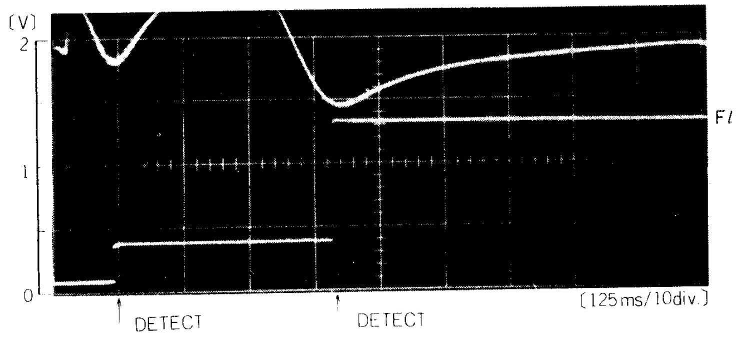

FIG. 74. Resonance detect performance. Two resonances are detected and the last one is stored and transmitted as Fl. Output wave form of logarithmic amplifier is superimposed. The dummy antenna circuit with L of 1H, C of 1000 pF is used.

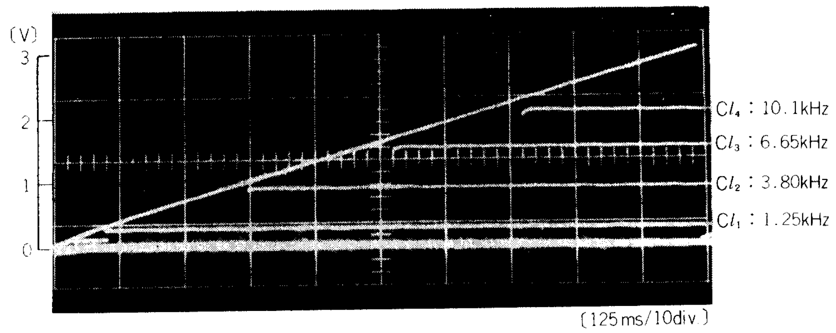

FIG. 75. Frequency reference levels $Cl_{1\sim4}$. ; saw-tooth wave form for this reference level is superimposed. Sampled potential is a little less than saw-tooth voltage, due to input-output characteristics of the sampling-hold circuit (HOLD 3, see Fig. 53).

$C_0=100$ pF, whose parallel and series resonance frequencies are 2.26 MHz and 1.31 MHz. The output signals from the frequency counter are illustrated in Fig. 70. The output admittance level after logarithmic amplifier are given superimposed with the counter output codes. The 8-bit binary counts (MSB) are indicating 00101100 for Fh_1 and 00011010 for Fh_2; these counts correspond to 2.23 MHz and 1.32 MHz, respectively. These agree well with the values of 2.26 MHz and 1.31 MHz, that are indicated by the direct recording of the admittance level, within an error of the frequency resolution of about 50 kHz.

IPL The measured admittance value in terms of the equivalent capacitance that is detected at the output of the logarithmic amplifier is illustrated in Fig. 71. A resonance-like behaviour of the admittance value appeared at the low frequency side of the sweep range is produced by leakage of the swept local signal which is allocated near the intermediate frequency and the returning interval of frequency sweep due to the retrace of the saw-tooth. Measured equivalent capacities at 1.25 kHz (Ll_1), 3.80 kHz (Ll_2) and 6.65 kHz (Ll_3) are given in Fig. 72. These curves are used for calibration of decimal counts from the PCM telemetry to the observed antenna admittance values. The detection functions of Ll_1, Ll_2, and Ll_3 are examined in the space plasma simulation chamber; Fig. 73 shows the outputs Ll_1, Ll_2, and Ll_3 from the sampling-hold circuit with the admittance level at the output point of logarithmic amplifier being superimposed in a dual trace oscilloscope. A typical response of the low frequency admittance of an antenna in a plasma is simulated by this test. Main contribution to the low frequency admittance of the antenna in a plasma is thought to be represented as RC parallel circuit with an inclination of 6 dB/Oct.. The difference between sampled output levels from output potentials of the logarithmic amplifier is due to the variation of stored potential by charge leak at the sample-hold circuit (see Fig. 53). *Fl* detection function is checked using a simulation circuit, with parameters $L=1$H, $C=1000$ pF and $C_0=1000$ pF, whose parallel resonance frequency is calculated to be 5.01 kHz. The measured *Fl* are illustrated in Fig. 74; the admittance level (equivalent capacity) at the output point of the logarithmic amplifier is superimposed in a dual trace oscilloscope. A pseudo resonance at the low frequency side is also detected. Since the last sampled data is transmitted to ENC, only *Fl* is detected. The data 1.25 V is translated to be 5.00 kHz using reference frequency levels Cl_1, Cl_2, Cl_3, and Cl_4 as shown in Fig. 75; this observed frequency *Fl* is very close to the calculated value, 5.01 kHz.

IV-2 Results of Space Environmental Test

2.1 Thermal test in vacuum environments

Operational characteristics of the electrical circuits in space environments largely depends upon the equipment temperature, which varies owing to (i) radiation energy input to the spacecraft due to solar radiation, planetary albedo and infra-red radiation from the earth [*20–23*]; (ii) radiative heat output through the spacecraft surface to the outer space [*24, 25*]; and (iii) heating of the environment due to

TABLE 4. 6 modes of the thermal vacuum test. α/ε is the ratio of solar absorptance to thermal emittance, θ_s sunlit angle, i.e. angle of the spacecraft axis with respect to the direction of the sun, δ the ratio of sunlit time to one period.

Mode	α/ε	θ_s	δ
A	0.730	90°	67%
B	〃	60°	〃
C	〃	45°	〃
D	〃	90°	100%
E	〃	60°	〃
F	0.846	90°	75%
G	〃	90°	67%

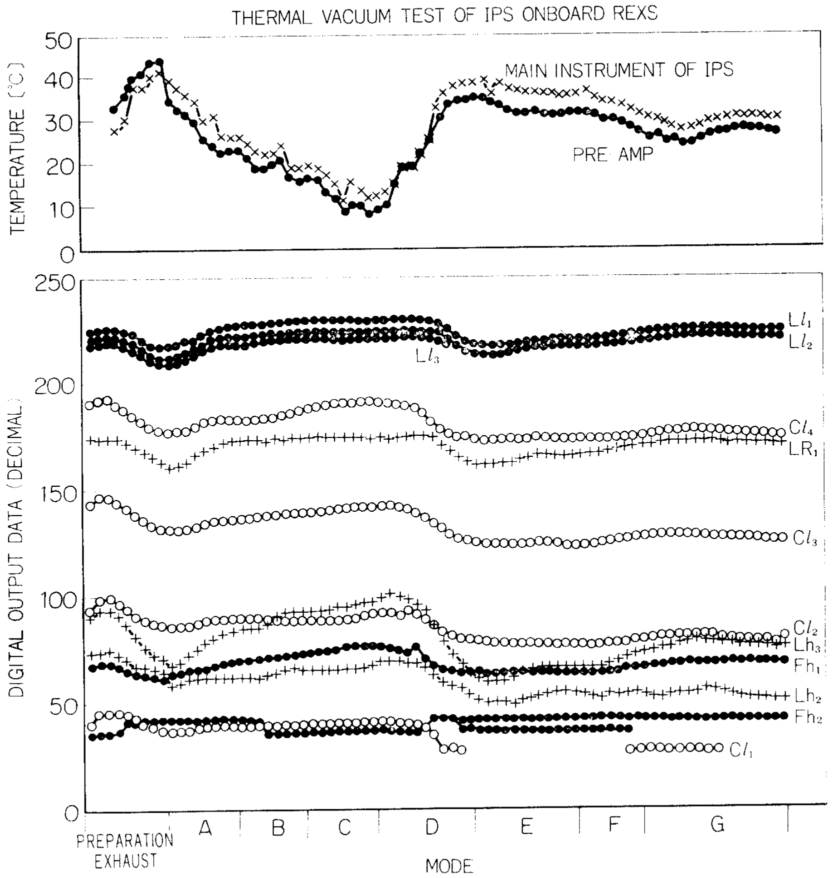

FIG. 76. Results of thermal vacuum test; conditions, modes A~G, are listed in Table 4.

energy from its own components, such as resisters, transistors and operational amplifiers. Thermal parameters of each part of the spacecraft [*20, 26*], such as heat capacity and heat transfer coefficients associated with the thermal contact

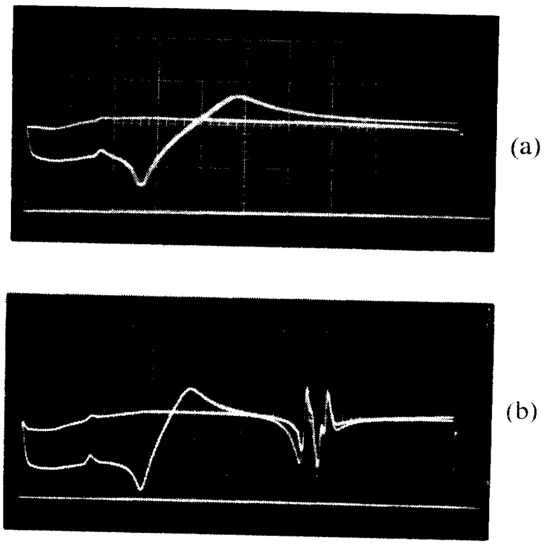

FIG. 77. Monitor output of IPH (Horizontal; 125 ms/10 div, vertical; 1 V/div.) (a) mode C (temperature of 8.5° C). (b) mode E (temperature of 30°C). Antenna is replaced by dummy electrical circuit i.e., series circuit of 6.2 kΩ∥100 pF and 5.6 μH∥4.7 kΩ∥30 pF, and calibration level (100 pF) is superimposed.

resistance and the radiation heat exchange of two surfaces are also important thermal controlling factors.

The analytical prediction of the spacecraft and equipment temperatures is impossible because of the number of unknown variables. Thermal measurement is thus carried out using one of space environmental simulation facilities; a vacuum chamber with liquid nitrogen cooled shroud which can adequately simulate the space environment pertaining to measure of thermal balance characteristics in the spacecraft [27]. Electrical heaters are attached to the spacecraft panels instead of solar simulators to simulate the radiation input energy.

The testing conditions are given as shown in Table 4. These conditions are produced to cover the maximum and also the minimum solar radiation input, considering the parameters of the spacecraft aspect on the presumed orbits as well as the parameters of the solar panel on spacecraft surface. The amount of input heat to the panels has been calculated for various geometrical relations between the spacecraft and the sun; cyclic heating and cooling are applied according to the computed sunrise and sunset times at the spacecraft position in orbit. This experiment required 216 hours (the experiment was carried out from June 19 to 29, 1972). Thermo-couples are located in both the pre-amplifier and the main IPS instrument. Temperature values of pre-amplifier are detected by the house keeping instrument (HK) and are transmitted through the telemetry system. To check the operational characteristics of IPS instrument, the simulation electrical circuit is used being replaced by the antenna in a plasma.

Results of this test are shown in Fig. 76. Fig. 77 is indicating the monitor output

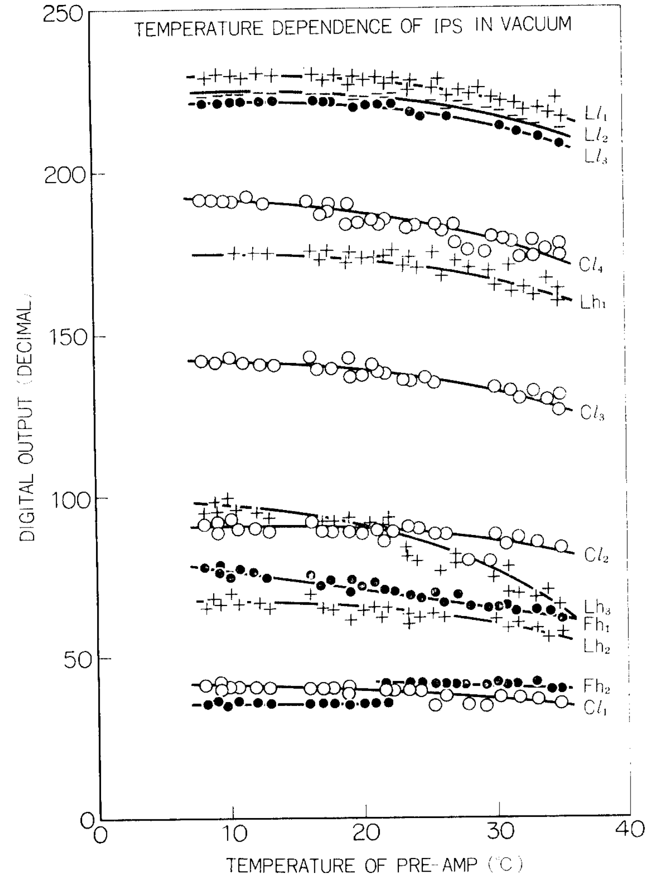

FIG. 78. Temperature dependence of gyro-plasma probe characteristics in vacuum.

of IPH. The temperature of the pre-amplifier is about 35°C at the beginning of mode A and gradually decreases to about 8°C at the end of mode C. Since mode D corresponds to a period of 100% sunlight, the equipment temperature increases again. As is obvious from Fig. 77, swept range of the high frequency is affected and Lh_1 (admittance level at 300 kHz) is misdetected below about 10°C. When the spacecraft was in orbit, the temperature was measured at a point in the pre-amplifier. The calibration curve of each measuring value versus temperature at the pre-amplifier was thus obtained by this thermal test. In Fig. 78, measured values versus temperatures at the pre-amplifier are summarized. The temperature calibration data for the value of Fl (Lower hybrid resonance frequency) are not obtained because the simulator of antenna is selected to have the high frequency resonance during this test. Calibration for Fl can, however, be deduced from the data $Cl_1 \sim Cl_4$.

2.2 Simulation experiment in plasma

The test of the gyro-plasma probe operation in a plasma was carried out by using the space plasma simulation chamber to examine output data relating to several parameters of the test plasma such as electron density, temperature, ion species

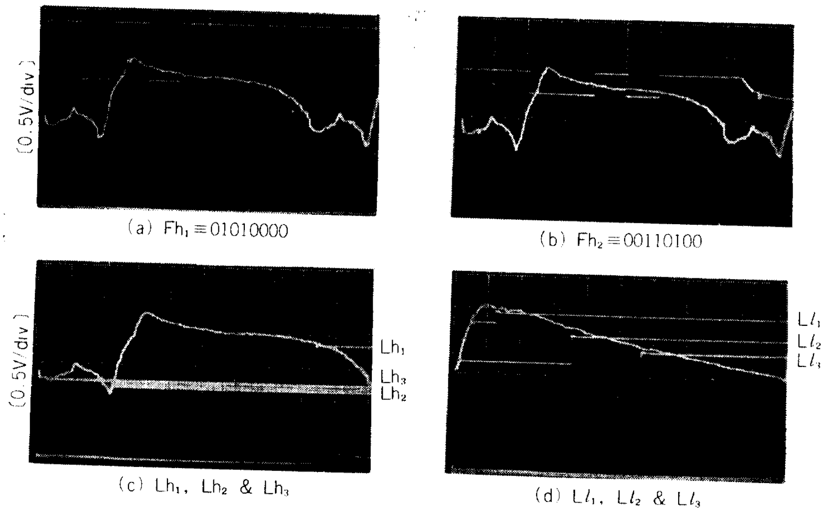

(a) $Fh_1 \equiv 01010000$ (b) $Fh_2 \equiv 00110100$

(c) Lh_1, Lh_2 & Lh_3 (d) Ll_1, Ll_2 & Ll_3

FIG. 79. A set of output data obtained in the space chamber experiment.

and magnetic field intensity. The plasma chamber test of the operational performance of the instrument was also made. Results of the plasma measurement were examined and compared with measurements of the Langmuir Probe method.

The chamber is a cylindrical vessel with 2000 mm in diameter and 3000 mm in length, and designed for simulation of the ionospheric and magnetospheric plasmas [*28*]. A set of Helmholz-coil is equipped to produce a homogeneous static magnetic field (about 0.4 gauss to 100 gauss) in the direction parallel to the axis of the vessel. The vessel is made of non-magnetic materials (stainless steel), not to be contaminated the applied magnetic field in the plasma. A residual gas back pressure of 10^{-9} torr. is attained, using two 36-inch oil diffusion pumps, a titanium sublination pump and a small sputter ion pump.

Installed in a frame of the spacecraft, instruments of IPS, CIE, PWP and TEL with a set of antennas are set in the vessel. The antenna of IPS is 1300 mm in length and located at the middle of the vessel. The capacitance bridges of IPH and IPL are balanced to eliminate the stray capacity of cabling and instrumentation in the condition of setup for the space simulation chamber experiment. The Langmuir probe is fixed to the scanning arm which can move mechanically to any desired position. Selected pure gases such as helium, neon and argon can be injected through the variable needle valve to high vacuum vessel with an arbitrary gas pressure in a range from 10^{-3} torr. to 10^{-6} torr. A pair of hot cathode coated by BaO are used to be back diffusion type plasma sources for a plasma with a low electron density less than 10^{7} cm^{-3} and electron temperature of 500°K to 4000°K.

Results of IPH and IPL Examples of output data obtained in the space chamber experiment are illustrated in Fig. 79(a)~(d). The high frequency gyro-plasma probe (IPH) and the low frequency gyro-plasma probe (IPL) were functioned well to measure the frequency characteristics of antenna impedance. Results are described as follows: The binary counter output for Fh_1 (UHR) is 01010000 (MSB) which is equal to 80 of decimal count and translated to be 4.063 MHz. Since the magnetic field strength is 0.42 gauss (corresponding electron gyro-resonance frequency is 1.17 MHz), the electron plasma frequency is 3.853 MHz, from which the electron density is calculated to be 1.88×10^5 cm^{-3}. The output for Fh_2 (SHR) is 00110100 (MSB) which is equal to 54 of decimal count and translated to be 2.742 MHz. These resonance frequencies coincide well with the obtained resonance frequencies from analog data calibrated by the standard signal generator. Output voltages of Lh_1 (0.3 MHz), Lh_2 (f_{UHR}) and Lh_3 (13 MHz) are 1.8 V, 1.1 V and 1.2 V corresponding to the equivalent capacitances of 68 pF, 14 pF and 21 pF, respectively. The calculated capacitance value of an antenna (1300 mm in length and 10 mm in diameter) in free space is 22 pF which coincides well with the measured value of Lh_3. The value of Lh_2 represents the equivalent Q (Quality Factor) of the upper hybrid resonance curve. As an electron-neutral collision frequency increases, the value of Q decreases and also the value of Lh_2 increased. This change of the value of Q is related not only to the collision frequency of electron neutral particles, but also to the complicated mechanism of an electrostatic wave excitation near the upper hybrid resonance [*29*]. The value of Lh_1 represents the sheath capacitance of an antenna. As an electron temperature increases and an electron density remains constant, the value of Lh_1 decreases, because of increasing of the sheath radius which is controlled by the Debye length.

The output voltages of Ll_1 (1.25 kHz), Ll_2 (3.80 kHz) and Ll_3 (6.65 kHz) are 2.4 V, 2.1 V and 1.86 V. These are translated to equivalent capacitances of 4300 pF, 950 pF and 480 pF, respectively, after the correction of characteristics of the sampling-hold circuit (HOLD-2) as shown in Fig. 53. The calibration curves of $L_{1\sim3}$ has been shown in Fig. 72.

The lower hybrid resonance frequency f_{LHR} is expressed as [*30*],

$$f_{LHR}=\left(\frac{1}{{f_{Hi}}^2+{f_{ei}}^2}+\frac{1}{f_{Hi}f_{He}}\right)^{-1/2}$$
$$=f_{He}\left\{\frac{m_p}{m_e}M_{eff}\left(1+\frac{f_{He}}{f_{pe}}\right)\right\}^{-1/2}$$

where f_{pe}, f_{pi}, f_{He} and f_{Hi} are electron plasma, ion plasma, electron gyro- and ion gyro-resonance frequencies, and m_p/m_e and M_{eff} are a mass ratio of proton to electron and effective ion mass, respectively. In this experiment, an argon plasma ($M_{eff}=39.948$) is used; the electron plasma and electron gyro-resonance frequencies are 3.89 MHz and 1.17 MHz. The lower hybrid resonance frequency is, then, calculated to be 4.15 kHz. The lower hybrid resonance (Fl) is not detected as has been seen in the analog data given in Fig. 79(d). This can be attributed to the high collisional frequency due to a partially ionized plasma state; the ionization rate is approximately 10^{-6}. The collision frequency is thought to be larger than the ion plasma and ion gyro-resonance frequencies; i.e., the impedance in the

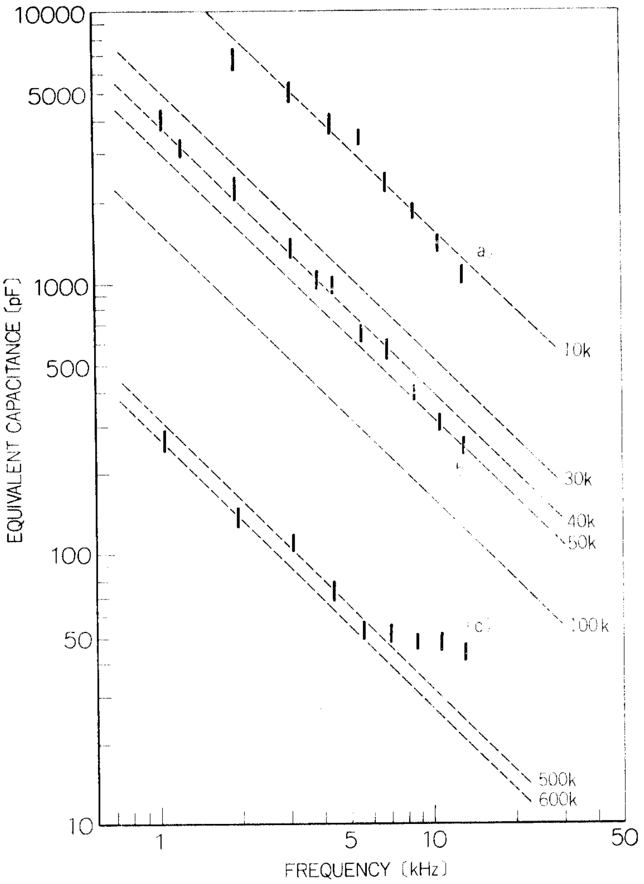

FIG. 80. Equivalent capacitance characteristics obtained in the space chamber experiment. Dashed lines show the frequency characteristics of equivalent capacitance corresponding to indicated resistances.

frequency range of 1 kHz to 15 kHz is predominated by the resistance of the sheath region surrounding the antenna in a plasma. The lower hybrid resonance is presumably able to be detected in the magnetosphere where the plasma in fully ionized to make collision frequency is less than the ion plasma and ion gyro-resonance frequencies.

Impedance at VLF Range As is shown in Fig. 79(d), the equivalent capacitance value in the frequency range of 1 kHz to 15 kHz decreases as the frequency increases. Three examples of experiments are summarized in Fig. 80, corresponding to experimental conditions listed in Table 5. In this frequency range, the impedance can be expressed as a parallel circuits consists of resistance and capacitance for each arm. This impedance is mainly controlled by the sheath surrounding the antenna, because the impedance of a plasma becomes very low. Therefore, the equivalent capacitance C_{eq} can be written as

$$C_{eq}=\sqrt{1+\omega^2C^2R^2}/R\omega \qquad (4.2)$$

where ω is an operating angular frequency. If the equivalent capacitance due to

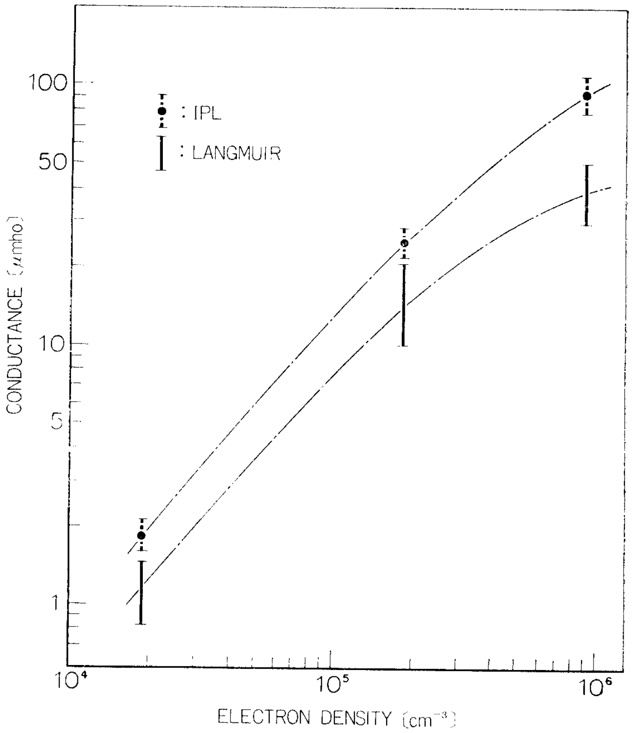

FIG. 81. Probe conductance versus electron density value. The values obtained simultaneously by Langmuir probe method are indicated.

the resistance is larger than the value of the capacitance C, that is, $(R\omega)^{-1} \gg C$, a lnC_{eq} value is expressed by a linear function of $ln\omega$. The values of the resistance can be deduced from Fig. 80; values are about 10 kΩ, 40 kΩ and 550 kΩ corresponding to the conditions (a), (b) and (c). These values decrease as the electron density increases, as is shown in Fig. 81. The conductance of sheath can be deduced from the current-voltage characteristics of the Langmuir probe in the vicinity of floating potential [31]. Namely, the conductance G is calculated as,

$$\begin{aligned} G &= \frac{\partial}{\partial V}\{I_{i0} - I_{e0}\exp(V/V_e)\}|_{V=V_0} \\ &\fallingdotseq I_e/V_e \end{aligned} \tag{4.3}$$

where I_{i0} and I_{e0}, V_0 and V_e are ion saturation current, electron saturation current, floating potential and electron thermal energy in volt, respectively. Results of the resistance calculated from Langmuir probe characteristics are plotted in Fig. 81, which are indicating a good coincidence with the values deduced from the low frequency gyro-plasma probe. In the case of (c), the equivalent capacitance at the higher frequency range in VLF range shows a constant value of the capacitance of sheath, because the resistance value is satisfying the condition that $(R\omega)^{-1} < C$; the constant capacitance value is about 50 pF that coincides with the value of 47 pF deduced from Lh_1 (1.65 V) within a measurement error.

TABLE. 5. Experimental conditions of the plasma in the space chamber.

		(a)	(b)	(c)
Gas		*Ar*	*Ar*	*N*
Pressure	P mmHg	—	6.8×10^{-5}	2.9×10^{-5}
Electron Density	N_e cm^{-3}	9.1×10^{5}	1.9×10^{5}	1.9×10^{4}
Electron Temperature	T_e °K	(1500)		1000
Debye Length	λ_D cm	0.28	0.62	1.6
Upper Hybrid Frequency	f_{UHR} MHz	8.64	4.06	1.71
Electron Plasma Frequency	f_{pe}	8.56	3.89	1.25
Electron Gyro-frequency	f_{He}	1.17		
Lower Hybrid Frequency	f_{He} MHz	4.27	4.15	5.32
Ion Plasma Frequency	f_{pi} kHz	31.6	14.4	8.36
Ion Larmor Radius	r_{Li} m	5.55		2.68
Sheath Capacity	C_{SH} pF	—	—	47
Sheath Conductance by LP	G μmho	31–52	10–23	0.85–1.5
Sheath Resistance by LP	R kΩ	19–32	44–96	670–1120
Sheath Conductance by IPL	G μmho	100	25	1.8
Sheath Resistance by IPL	R kΩ	10	40	55

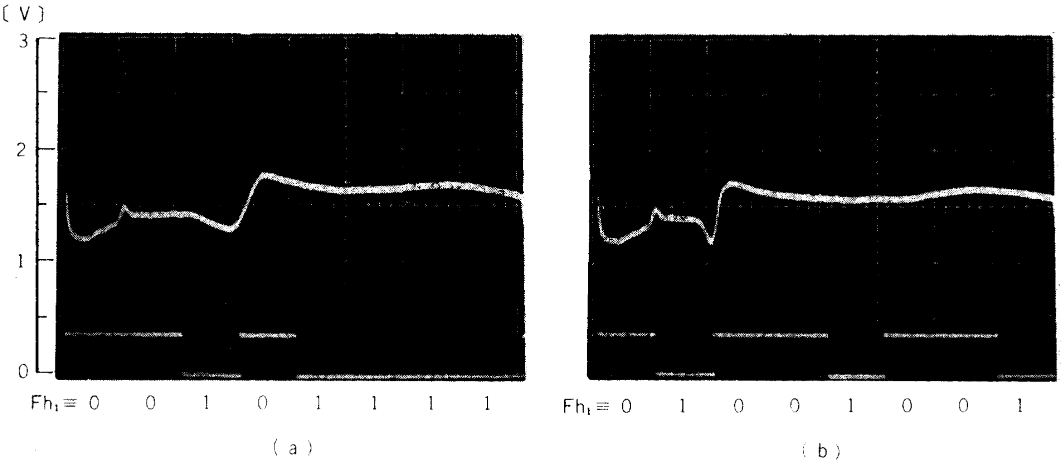

(a) (b)

FIG. 82. Frequency change of upper hybrid resonance due to applied magnetic field; (a) 0.57 gauss, (b) 1.14 gauss.

Results of Applied Magnetic Field The upper hybrid resonance frequency is a function of a magnetic field intensity. To identify the Fh_1 resonance to be the upper hybrid resonance frequency, its frequency change is examined due to vary-

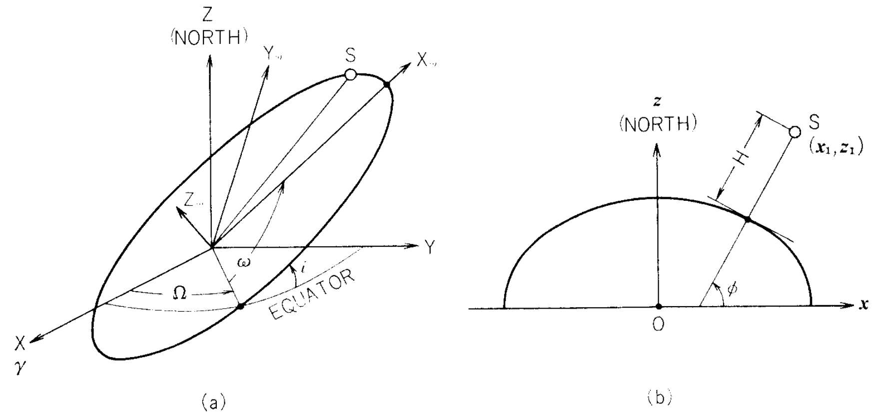

FIG. 83. (a) Orbit plane coodinate system (X_ω, Y_ω, Z_ω) and right ascension-declination coordinate system (X, Y, Z). (b) Geodetic coordinate system.

ing external magnetic field intensity. Two examples of experimental results in the helium plasma with the gas pressure of 1.4×10^{-4} torr., and the electron density of 4.0×10^{4} cm^{-3} are shown in Fig. 82(a) and (b). The produced magnetic field intensities are 0.57 gauss and 1.14 gauss; outputs of the binary counter Fh_1 corresponding these magnetic field intensities are 2.386 MHz and 3.707 MHz, respectively. Calculated values of the upper hybrid resonance frequencies using the observed electron density and the magnetic field strength are 2.41 MHz and 3.66 MHz, which agree well with the observed data of Fh_1 again, within the measurement error.

V. COMPUTER SYSTEM FOR DATA ANALYSIS

V-1 Data Processing and Analysis System

The large volume of data transmitted from the satellite should be analysed with precise orbit data to fix the time-space of each datum point. For this purpose a systematic usage of a computer system is necessary.

The data are transmitted to the ground station through the telemetry system. The received signals, on the ground, are demodulated to obtain the differential phase shift keying (DPSK) codes. DPSK codes are decoded to obtain digital binary codes. These binary codes are stored in the tape recorder with the frame counter code given in the special portion of telemeter frame that is here called F and F_0 counter. These data are edited by the computer that can be controlled by the FORTRAN IV language, adding the starting time (UT) of the data frame. Messages that consist of the satellite code number, the revolution number, the receiving data and time, the frame period, the data block number, and counter numbers of F and F_0, are also put into the computer with the observation data.

The position of the spacecraft is computed using six elements of the satellite orbit and its secular variations, and the time when data were obtained [*31*]. Data in binary code on the magnetic tape rearranged, calibrated, and converted to physical quantities such as electron density, impedance value of an antenna in orbit and so on. The geomagnetic field is also computed using a geomagnetic reference field. Finally, these data associated with its positions are graphically displayed with a computer controlled X-Y plotter (HITAC 5020F and CALCOMP 502), in order to obtain electron density profiles versus altitude, geomagnetic latitude, local time, and other parameters.

Orbital Aanalysis The methods to calculate the satellite orbit in an arbitrarily coordinate system have been presented by many workers (see P. R. Escobal [*33*] as a review). A brief summary is given to show the calculation procedure. In the present calculation, following orbital elements at epoch time T_0 are given; semi-major axis a [km], eccentricity e, inclination of the orbital plane i [degree], right ascension of ascending node Ω [degree], argument of perigee ω [degree], mean motion n [degree/min], mean anomaly M [degree], and their secular variations due to the perturbation around the Keplerian orbit. The eccentric anomaly E is determined from Kepler's equation,

$$E-M=e\sin E. \qquad (5.1)$$

In Fig. 83(a), the geometrical relation between the orbit plane coordinate system $(X_\omega, Y_\omega, Z_\omega)$ and the right ascension-declination coordinate system (X, Y, Z) is indicated. The vector γ (see Fig. 83(a)) shows the direction of the mean vernal equinox and Z is the earth's rotation axis. The orthogonal components of the satellite position are obtained as functions of the eccentric anomaly angle E, as

$$\begin{aligned} X_\omega &= a(\cos E-e), \\ Y_\omega &= a\sqrt{1-e^2}\sin E, \\ Z_\omega &= 0, \end{aligned} \qquad (5.2)$$

and these components are transformed into X, Y, and Z components by,

$$\begin{bmatrix} X \\ Y \\ Z \end{bmatrix} = (T)\cdot\begin{bmatrix} X_\omega \\ Y_\omega \\ Z_\omega \end{bmatrix}, \qquad (5.3)$$

where

$$(T)=\begin{bmatrix} \cos\omega\cos\Omega-\sin\omega\sin\Omega\cos i, & -\sin\omega\cos\Omega-\cos\omega\sin\Omega\cos i, & \sin\Omega\sin i \\ \cos\omega\sin\Omega+\sin\omega\cos\Omega\cos i, & -\sin\omega\sin\Omega+\cos\omega\cos\Omega\cos i, & -\cos\Omega\sin i \\ \sin\omega\sin i\quad, & \cos\omega\sin i\quad, & \cos i \end{bmatrix}. \qquad (5.4)$$

The position (R, θ, λ_E) in the geocentric cooodinate systems is determined from the relations, as

$$R=\sqrt{X^2+Y^2+Z^2}$$

$$\theta=\tan^{-1}(Z/\sqrt{X^2+Y^2}), \qquad (5.5)$$

and

$$\lambda_E=\mathrm{mod}\,(360^\circ+\lambda-\lambda_g,\ 360^\circ).$$

where λ_E is the angle measured eastward in the equatorial plane between the inertial X-axis (direction of a mean vernal equinox) and the observer's meridian, and λ_g is the Greenwich angle, that is, the angle between the inertial X-axis and the Greenwich prime meridian. The practical calculation of Greenwich sidereal time at 0 hour U.T. can be accomplished by means of the following formula [*33*],

$$\lambda_{g0}=99.6909833+36000.7689\ Tu+0.00038708\ Tu^2 \qquad (5.6)$$

where the time is measured in centuries as

$$Tu=\frac{JD-2415020.0}{36525} \qquad (5.7)$$

and JD is the Julian Date which is a continuing count of each day elapsed since January 1, 4313 B.C. The Greenwich angle λ_g at any time Δt of day can be obtained if it is known that there is one extra sidereal day for every tropical year, i.e.,

$$\begin{aligned}\frac{d\lambda}{dt}&=1+\frac{1}{365.24219879}\ [\text{revolutions/day}]\\&=0.2506844773\qquad [\text{degrees/minute}]\end{aligned} \qquad (5.8)$$

then

$$\lambda_g=\lambda_{g0}+\Delta t\cdot d\lambda/dt \qquad (5.9)$$

The position (H, ϕ, λ_E) in the geodetic coodinate system (see Fig. 83 (b)) is determined for the height H from the earth' surface and the geodetic latitude ϕ, as

$$H=\sqrt{(x_0-x_1)^2+(z_0-z_1)^2}, \qquad (5.10)$$

and

$$\phi=\tan^{-1}\left(\frac{z_0-z_1}{x_0-x_1}\right),$$

where

$$x_1=R\cos\theta,$$

$$z_1=R\sin\theta,$$

$$z_0=z_1x_0(1-e_0{}^2)/(x_1-e_0{}^2x_0),$$

and x_0 is one of the roots of the following quartic,

$$x^4+a_1x^3+a_1x^2+a_3x+a_4=0,$$

with

$$a_1=-2x_1/e_E^2,$$

$$a_2=-a_E^2+x_1^2/e_E^4+(1-e_E^2)y_1^2/e_E^4, \qquad (5.11)$$

$$a_3=2a_E^2x_1/e_E^2,$$

and

$$a_4=-a_E^2x_1^2/e_E^4.$$

In these equations a_E is the equatorial radius of the earth (6378.160 km) and e_E the eccentricity of the earth (0.08182). The transformation from the geocentric coordinates to the geodetic coordinates adapted here is to solve the quartic by Newton's method and to determine one of the roots that is located in the same quadrant as the position in the geocentric coordinate system. In this computation, the convergence limit to obtain the root is set to be 0.1 km which is an adequate resolution for the data sampling of the present observation.

The geomagnetic coordinate system (θ_m λ_{Em}) are used extensively in physics of geomagnetic phenomena [*34*]. The northern and southern points where the axis of the centered dipole, that is set to give the best approximation to the earth's main magnetic field, intersects the surface of the earth are called geomagnetic north and south poles, respectively. The geomagnetic north pole is near Thule, Greenland, at 290.239°E geographic longitude and approximately 11.435° from the geographic north pole on this meridian. Thus, the geomagnetic dipole latitude θ_m and dipole longitude λ_{Em} can be easily obtained from geocentric latitude and longitude as follows.

$$\begin{aligned} \sin\theta_m &= \sin\theta\cos 11.435^\circ + \cos\theta\sin 11.435^\circ\cos(\lambda_E - 290.239) \\ \sin\lambda_{Em} &= \cos\theta\sin(\lambda_E - 290.239^\circ)/\cos\theta_m \end{aligned} \tag{5.12}$$

Geomagnetic Field Intensity As noted in Appendix A, the gyro-resonance frequency can be deduced from the geomagnetic field intensity. The geomagnetic reference field is expressed by a series of spherical harmonics in geocentric spherical coordinates with the geomagnetic potential V and intensity components given by

$$\begin{aligned} V &= a_0 \sum_{n=1}^{10} \sum_{m=0}^{n} \left(\frac{a_0}{r}\right)^{n+1} \cdot F_{nm}(\lambda_E)\cdot P_n^m(x), \\ X &= \frac{1}{r}\frac{\partial V}{\partial\theta'} = -\sin\theta' \sum_{n=1}^{10}\left(\frac{a_0}{r}\right)^{n+2} \sum_{m=0}^{n} F_{nm}(\lambda_E) DP_n^m(x), \\ Y &= \frac{-1}{r\sin\theta'}\frac{\partial V}{\partial\lambda_E} = \frac{1}{\sin\theta'} \sum_{n=1}^{10}\left(\frac{a_0}{r}\right)^{n+2} \sum_{m=0}^{n} m\cdot G_{nm}(\lambda_E) P_n^m(x), \\ Z &= \frac{\partial V}{\partial r} = -\sum_{n=1}^{10}(n+1)\left(\frac{a_0}{r}\right)^{n+2} \sum_{m=0}^{n} F_{nm}(\lambda_E) P_n^m(x), \\ & F_{nm}(\lambda_E) = g_n^m \cos m\lambda_E + h_n^m \sin m\lambda_E, \\ & G_n^m(\lambda_E) = g_n^m \sin m\lambda_E - h_n^m \cos m\lambda_E, \\ & DP_n^m(x) = dP_n^m(x)/dx. \end{aligned} \tag{5.13}$$

In the above expressions, $P_n^m(x)$ is the associated Legendre function of degree n and order m and of the Schmidt quasi-normalized type defined by

$$P_n^m(x) = \frac{1}{2^n n!}\left[\frac{\varepsilon_m(n-m)!(1-x^2)^m}{(n+m)!}\right]^{1/2} \frac{d^{m+n}(x^2-1)^n}{dx^{m+n}}, \tag{5.14}$$

with

$$\varepsilon_m = \begin{cases} 1 & \text{for } m=0 \\ 2 & \text{for } m \geq 1, \end{cases}$$

and $x = \cos\theta'$ where θ' is a geocentric colatitude measured from the north pole. X, Y, and Z are the northward, the eastward and the downward components of the magnetic field vector. g_n^m and h_n^m are the spherical harmonic Gaussian coefficients, and the values proposed by J. C. Cain and R. E. Sweeney [*35*] are employed in this calculation. The total scalar intensity F and the gyro-resonance frequency f_H are obtained as

$$F = \sqrt{X^2 + Y^2 + Z^2},$$

and

$$f_H = 2.7992048 \times F \quad [\text{MHz};\ F \text{ in Gauss}].$$

In computing $P_n^m(x)$ and $dP_n^m(x)/dx$, the following recurrence formulas are introduced from eq. (5.14), as,

$$P_n^m(x) = \begin{cases} \dfrac{1}{\sqrt{n^2 - m^2}} [(2n-1)x \cdot P_{n-1}^m(x) - \sqrt{(n-1)^2 - m^2} \cdot P_{n-2}^m(x)] \\ \hfill \text{for } 0 \leq m \leq n-2, \\ \dfrac{1}{\sqrt{(n+m)(n-m+1)}} \cdot [2(m-1) \cdot x/y \cdot P_n^{m-1}(x) - \sqrt{(n+m-1)(n-m+2)} \\ \quad \times P_n^{m-2}(x)] \hfill \text{for } 2 \leq m \leq n \end{cases} \tag{5.16}$$

and

$$\frac{dP_n^m(x)}{dx} = -\frac{\sqrt{(n+1)^2 - m^2}}{y^2} P_{n+1}^m(x) + \frac{(n+1)x}{y^2} P_n^m(x). \tag{5.17}$$

Local Time The electron density in the ionosphere depends largely on the local time, that is, the solar zenith angle at the observed position. Using the universal time UT [hours] and the east longitude λ_E [degrees], the local time LT [hours] at the observed position is approximately calculated by

$$LT = \text{mod}\,(UT + \lambda_E/15^\circ, 24) \tag{5.18}$$

The electron density profiles along the spacecraft orbit are described with the observed position that is expressed on the geocentric, geodetic and geomagnetic coordinate systems with the local time.

V-2 Calibration Methods

The digital data recorded on the magnetic tape at the ground station are re-arranged according to observational items listed in Table 2. After corrections of equipment characteristics due to temperature variation in the satellite environment, the data are transformed to physical values such as frequencies and the admittance values due to the calibrated data by the equipment for each item.

Correction of Thermal Shift As indicated in IV-2, the operation characteristics of instruments onboard spacecraft depend largely on the operating temperature. The temperature of the IPS pre-amplifier is measured with the house keeping instrument (HK). Correction function for the data with respect to temperature T is expressed in a form of the series on $\Delta T = T - 20$ using the standard temperature of 20°C as,

$$N_T = N_0 + \sum_{n=1}^{N} C_n (\Delta T)^{n-1} \tag{5.19}$$

where N_T and N_0 are the data values at T°C (the temperature of pre-amplifier) and 20°C respectively. The coefficients C_n ($n=1, \ldots, N$) are determined to make the best fit to measured result that has been obtained by the thermal vacuum test as shown in Fig. 78.

Upper Hybrid and Sheath Resonance Frequencies Since the gate pulse width of the frequency counter for the Fh_1 and Fh_2 data is 19.692 μsec, the relation between the digital data N_0 and the resonance frequency f is given by

$$f_{UHR} \text{ or } f_{SHR} = N_0 \times 50.782 \text{ [kHz]}. \tag{5.20}$$

Admittance Values at 0.3 MHz, f_{UHR}, and 13 MHz Calibration curves for the admittance values at 0.3 MHz and 13 MHz versus the digital data are deduced from Fig. 68. The calibration function is given by an expression, as

$$Lh_1 \text{ or } Lh_3 = 10{*}{*} \sum_{n=1}^{5} C_n N_0^{n-1} \text{ [pF]}. \tag{5.21}$$

There are technical difficulties to obtain the measured calibration function for Lh_2, because Lh_2 is the admittance value at the upper hybrid resonance frequency. That is, the calibration data for Lh_2 largely depends on the resonance frequency itself. The calibration is then made using a linear interpolation method as

$$Lh_2 = Lh_3' + \frac{13 - f_{UHR}}{13 - 0.3} (Lh_1' - Lh_3') \tag{5.22}$$

where Lh_1' and Lh_3' are the calibrated values, using eq. (5.21) of the raw data corresponding to Lh_2.

Lower Hybrid Resonance Frequency The lower hybrid resonance frequency Fl is deduced from $Cl_{1\sim4}$ which are output values corresponding to frequencies of 1.25, 3.85, 6.65, and 10.10 kHz. The calibration function given as the frequency versus digital data, is given in quadratic equation by least squares using $Cl_{1\sim4}$ which are obtained in the same period of the telemetry frame. The standard digital data corresponding to $Cl_{1\sim4}$ are 42, 93, 142, and 187, respectively. These values are used as alternate data when the misdetections on any $Cl_{1\sim4}$ are revealed in the onboard operations.

Admittance Values at 1.25, 3.80, and 6.65 kHz Admittance values for $Ll_{1\sim3}$ in IPL channel have been obtained after the three steps of corrections. The first is the correction due to the characteristic of the encoder (ENC), that can be carried out using a function as

$$V_1 = \sum_{n=1}^{3} C_n N_0^{n-1}, \tag{5.23}$$

where N_0 is the obtained digital data for $Ll_{1\sim3}$. The second correction is for the gate and hold circuits; the characteristics are given by

$$V_0 = \sum_{n=1}^{3} C_n V_1^{n-1} \tag{5.24}$$

where V_0 and V_1 are input and output voltages. The inputs V_0 versus outputs V_1 characteristics of the gate and hold circuit is given in Fig. 53. The third correction is due to the relation of the output voltage from the logarithmic amplifier and the antenna admittance value that is given in Fig. 72; the function is here expressed by

$$Ll_{1\sim 3} = 10{*}{*} \sum_{n=1}^{5} C_n V_0^{n-1} \,[\text{pF};\ V_0 \text{ in volt}] \tag{5.25}$$

All the coefficients C_n in eqs. (5.19) to (5.25) including the calibration curve

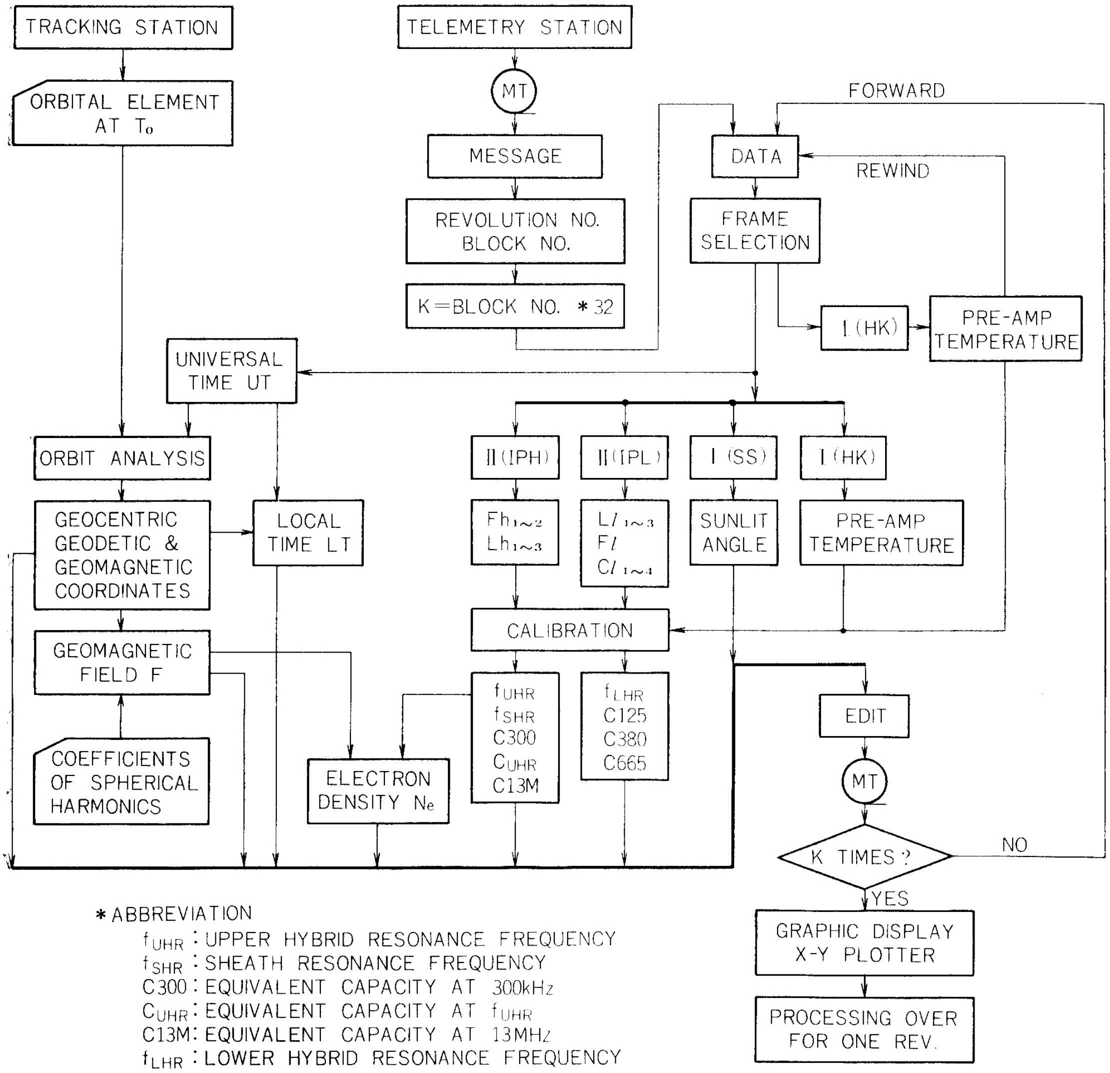

*ABBREVIATION
f_{UHR} : UPPER HYBRID RESONANCE FREQUENCY
f_{SHR} : SHEATH RESONANCE FREQUENCY
C300 : EQUIVALENT CAPACITY AT 300kHz
C_{UHR} : EQUIVALENT CAPACITY AT f_{UHR}
C13M : EQUIVALENT CAPACITY AT 13MHz
f_{LHR} : LOWER HYBRID RESONANCE FREQUENCY
C125 : EQUIVALENT CAPACITY AT 1.25kHz
C380 : EQUIVALENT CAPACITY AT 3.80kHz
C665 : EQUIVALENT CAPACITY AT 6.65kHz

FIG. 84. Flow chart of data analysis system.

for the temperature of pre-amplifier versus decimal values of HK outputs (word number of W_8 in the telemetry frame whose F counter number is 18) are given in Appendix D.

V-3 Computation and Graphical Display

The electron density distribution in global scale are deduced from the measured upper hybrid resonance frequency f_{UHR} with the data of the position where observations were carried out, using eq. (A.6) in which gyro-resonance frequencies f_H were calculated from eq. (5.15). In addition to the upper hybrid resonance frequency, the admittance value at 300 kHz (Lh_1) was also used.

To show electron density profiles as a functions of local time, latitude, and geomagnetic coordinates, the automatic graphical display method is employed using an electronic computer system with a X-Y plotted. The data on spacecraft positions as noted in V-1 and 2 and the observation data are also stored in the corresponding addresses of the common area of the computer core memory to access quickly due to the program demand. The magnetic tapes are prepared by combining and rearranging these data and the parameters, including operational functions for the X-Y plotter. The flow chart of computing systems for these data analysis is illustrated in Fig. 84.

VI. EXPERIMENTAL RESULTS

VI-1 Experimental Performance

Mu 4S-4 Launching Mu 4S-4 rocket was launched from the Kagoshima Space Center (31°15′00″ North, 131°04′45″ East, 0.3302 km Height), Uchinoura, Kagoshima, Japan, at 02:40 UT (11:40 JST), August 19, 1972. At 7 min 8 sec after the lift-off, the fourth stage motor injected the spacecraft REXS into orbit at the altitude of 287 km, with the speed of 8.897 km/sec. The satellite was named by "DENPA (Radio Wave)" which bears the international designation "1972-064A".

Mu 4S-4 is a solid propellant four-stage rocket designed as a vehicle for launching the scientific satellite. Total weight of the vehicle is 43,522 kg, the length is 23.698 m, and the diameter of the first and second stages is 1.41 m. Eight strap-on boosters are attached to the first stage in order to augment the thrust at the lift-off time and are jettisoned at 9.5 seconds after lift-off. The first stage flight is stabilized aerodynamically by cruciform fins. After the burnout and the coasting of 20 seconds, the nose covering is jettisoned at the altitude of 50 km, approximately, and then the first stage motor is separated from the upper stage. Ignition of six spin motors, and deployment of six sheets of flares take place to obtain the spin stabilization in the axial direction of the total spacecraft keeping the spin motion of 2.6 rps. The ignition of the second stage motor takes place in series at the interval of 1 second. The third stage motor burns after the separation of the second stage motor. The altitude control system is located between the third and fourth stage. After jettison of the third stage motor, the spinning motion of the upper stage spacecraft is slowed down by a pair of solid despinning motors. The attitude control system start to operate, then, to direct the vehicle to the local horizontal at the corresponding peak altitude of the rocket trajectory. The hydrogen-peroxide engine for the attitude control (roll, pitch and yaw) consists of four hydrogen-peroxide reservoirs, two nitrogen gas reservoirs and eight-jet nozzles. When the attitude control is finished, a pair of roll jets give a spin of 0.5 rps to the vehicle. A pair of respin motors are operated to raise the vehicle spin up to 2.7 rps to keep the axial stability again. The fourth stage spherical motor is ignited at the peak of the trajectory. The ignition is designed to make by a programmed timer. A radio command system for the ignition is also prepared for the case of the deviating flight from the planned trajectory. The last stage spherical motor provides a velocity increment to achieve orbital velocity. After the burnout of the last stage motor, the main spacecraft is separated by releasing a marman clamp keeping the spin motion for attitude stabilization. Three retromotors are fired to decelerate the burnout motor to give a safety distance between the main spacecraft.

Detailed descriptions and preliminary results about the launching phase of the Mu 4S-4 has been reported by the rocket launching group [*36*].

Performance and Trajectory of REXS The instruments in REXS operated satisfactory following the planned programme in the launching phase and the orbital injection phase. The first step of monopole antenna was deployed by the pre-set timer, and the second and third steps were extended by the radio command at the first and sixth of the satellite revolutions, respectively. At the Kagoshima Space Center, all the real-time mode telemetry data as well as the onboard tape-recorder playback mode data were received from August 19 to 22. On August 22, 09:07

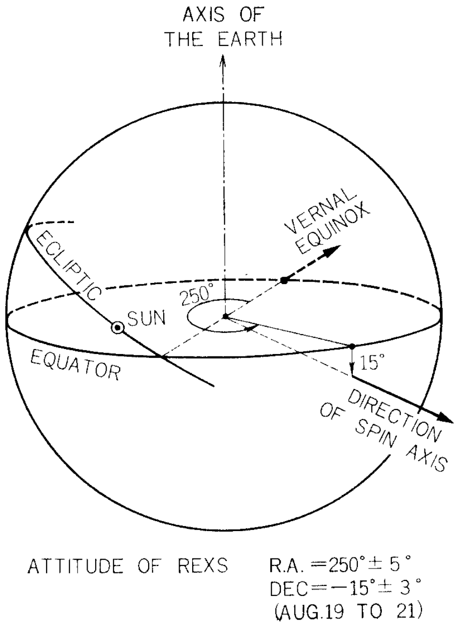

FIG. 85. Attituce of the spacecraft in right ascension-declination coordinate system.

JST when the high tension electrical circuit of the electron flux analyser (EBA) was switched on at the first time after the launch, a fatal accident took place. The power supplies of the spacecraft fell in some abnormal condition, and the telemetry encoder ceased to operate normally so that no further meaningful data could be transmitted afterwards. Therefore, the data during the first to 26th revolutions around the earth were available to manipulate.

The attitude of the spacecraft was measured by the fluxgate magnetometer (MGS) [*37*]. This gives the direction of the spin axis in the right ascension of $250^\circ \pm 5^\circ$, declination of $-15^\circ \pm 3^\circ$, with the corning angle of less than 5°. The angle between the spacecraft spin axis and the direction of the sun is estimated to be 108°. The attitude of the spacecraft in the right ascension-declination coordinate system is illustrated in Fig. 85. The spin rate was 2.99 rps at the time of injection, decreasing gradually with time at rate of -0.01 rps/100 revolutions.

The post-launching radio tracking was made by the collaboration of Japanese network, NASA, and CNES tracking stations. The routine radio tracking has been conducted by Orbit Computation Center (Tsukuba) of National Space Development Agency (NASDA), using the data of tracking stations at Katsuura, Okinawa and Uchinoura (KSC). The spacecraft has been injected into an elliptic orbit and the result of orbital elements of REXS on August 21 reported by NASDA are;

Epoch Time		1972, 8, 21.00.00.00 UT	
Semi-major Axis	a	[km]	9784.453
Semi-major Axis Dot	$\dot{a}$	[km/day]	0.0
Eccentricity	e		0.3233
Inclination	i	[deg]	31.002
R.A. of Ascending Node	Ω	[deg]	41.392
Motion of Ascending Node	$\dot{\Omega}$	[deg/day]	-2.383
Argument of Perigee	ω	[deg]	127.878
Motion of Perigee	$\dot{\omega}$	[deg/day]	3.717
Mean Motion	n	[deg/min]	2.244
Mean Motion Dot	$\dot{n}$	[deg/min/day]	0.0
Mean Anomaly	M	[deg]	319.170
Anomalistic Period	T_p	[min]	160.533
Period Dot	$\dot{T}_p$	[min/day]	0.0
Height of Perigee	h_p	[km]	242.983
Height of Apogee	h_a	[km]	6569.593

These parameters were used to calculate the spacecraft position where the observation was carried out. The orbit of the spacecraft REXS projected on the earth's surface is illustrated in Fig. 86. Since the anomalistic period of this spacecraft was about 24 hours/9, the orbits of revolution numbers of n and $n+9$ are approximately the same. And, the deviation of the local times at the same phases of the spacecraft positions in orbit is approximately equal to the motion of ascending node which is turned out to be very small. Fortunately, these facts are very convenient to investigate the physical conditions of the electron density profiles

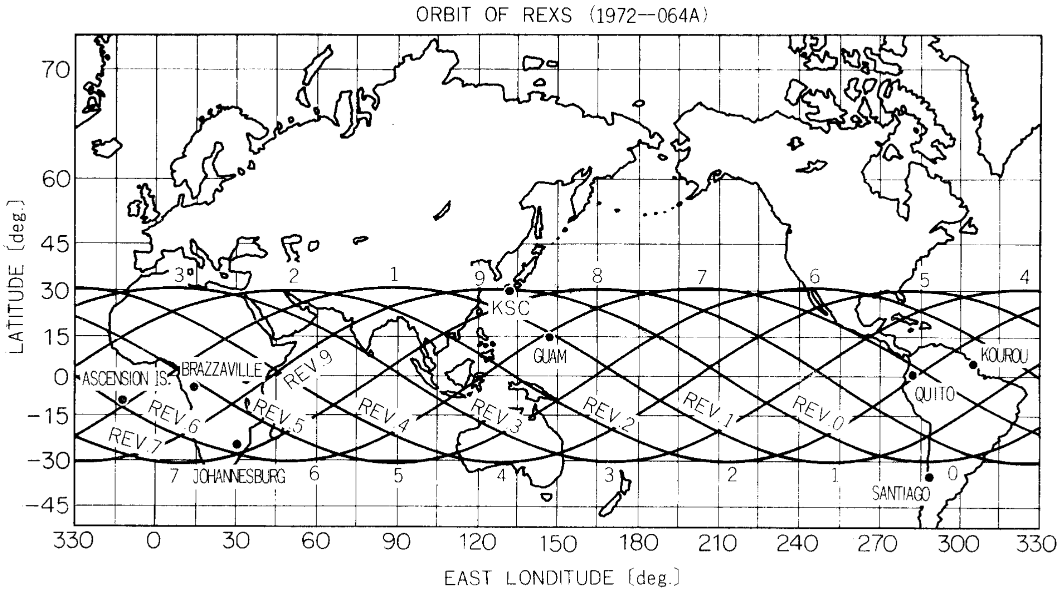

FIG. 86. Orbit of REXS satellite.

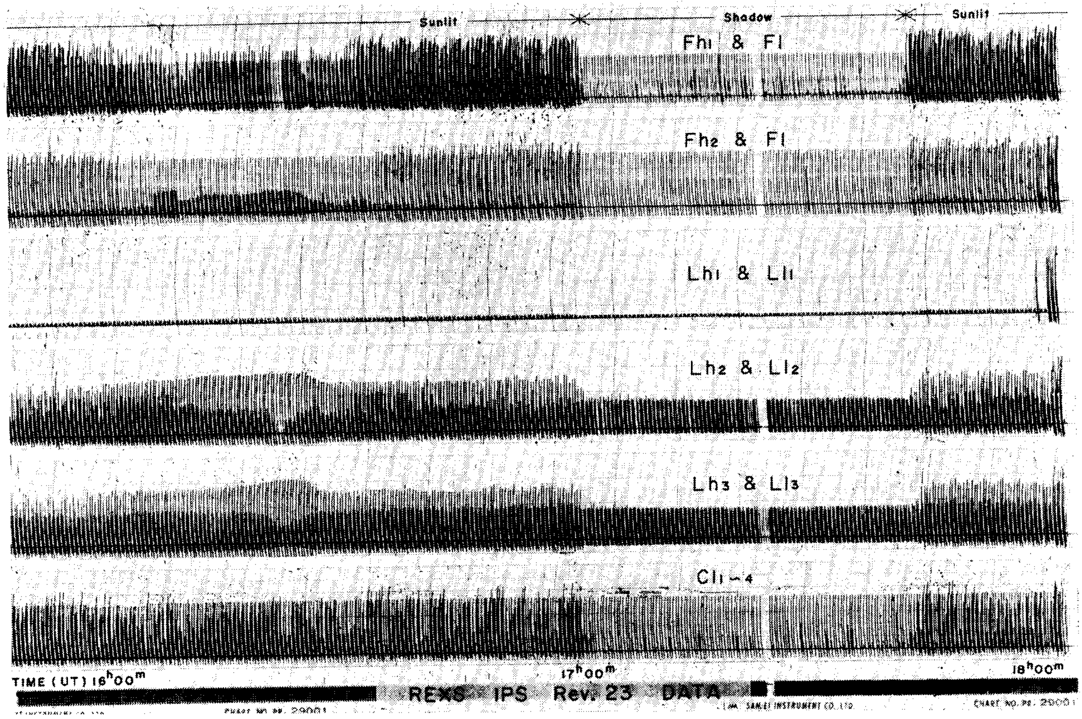

FIG. 87. Records of IPS quick-look (rev. No. 23, Aug. 21, 1972).

in the ionosphere.

VI-2 Observed IPS Data

The IPS instrument onboard the spacecraft REXS has been successfully functioned and the measured values of all the observational items have been transmitted. The real-time telemetry data were recorded on the paper tapes, and the onboard tape-recorder playback data were stored on the magnetic tapes. Both these data

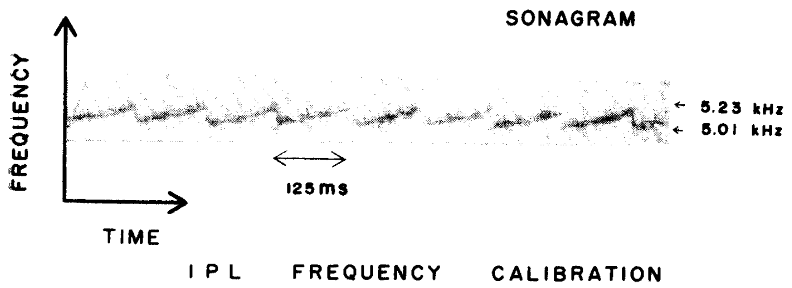

FIG. 88. Record of IPL frequency calibration.

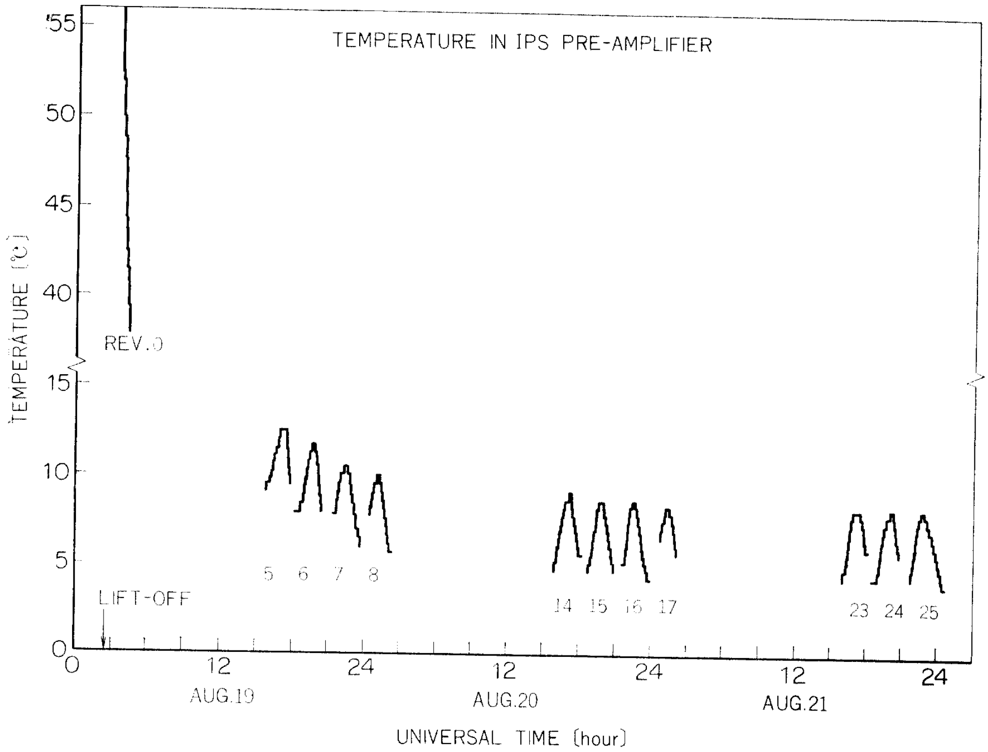

FIG. 89. Temperature in IPS pre-amplifier obtained with house keeping equipment.

signals were, also, sent to the main quick-look equipment and converted to analog forms that were displayed by the pen-recorders. The IPS quick-look sorted these time-serial data of mode II_1 and II_2 into six parallel channels that include two items each as Fh_1 and Fl in #1, Fh_2 and Fl in #2, Lh_1 and Fl_1 in #3, Lh_2 and Ll_2 in #4, Lh_3 and Ll_3 in #5, and $Cl_{1\sim 4}$ in #6. In Fig. 87, an example of the data displayed by the quick look system is shown for the case of revolution #23, on Aug. 21, 1972. An overall profile of the measured values of each observational item during one revolution period of the satellite observation can be clearly seen from this chart. The upper hybrid and sheath resonance frequencies (Fh_1 and Fh_3) show the maximum values at the height of about 390 km which corresponds to the height of F2 layer. Above this altitude, the values are gradually decreasing. The admittance value at f_{UHR} (Lh_2) is inversely correlated to the values of Fh_1 and Fh_2. The value of Lh_3 shows the admittance value of the antenna in free space, and slightly decreases as Fh_1 increases. Admittance values at VLF range (Ll) are abruptly changed when the spacecraft passed through the shadow line due to the earth. The detailed features of the observed data will be given later.

To check the instrument condition, the command signal "IP CAL ON" was transmitted at the revolution #17. The transmitted subcarrier data for the frequency monitor of the crystal controlled oscillator for the high frequency gyro-plasma probe was 5.59 kHz. The swept frequency of the low frequency gyro-plasma probe was from 5.01 kHz to 5.23 kHz, as shown in Fig. 88. These calibration data showed quite normal values as noted in section III-6.

The temperature in the pre-amplifier was monitored, the data from the revolution #0 to #25 being plotted in Fig. 89. The temperature was about 56°C at the beginning phase of the orbiting. As the spacecraft passed through the sunlit and the shadow regions periodically, the temperature oscillated with an amplitude of about 4°C, except for the case of the initial revolution that showed a rapid decrease in temperature. These data are used for the correction of observed data corresponding to the operational temperature of the equipment.

Examples of the observed data for each observational item as the function of local time are illustrated in Figs. 90 to 98, being converted from the binary counts to the corresponding frequencies and the equivalent capacitance values through the calibration method (see V-2).

Upper Hybrid Resonance Frequency, Fh_1 Figure 90 shows the typical variation of the upper hybrid resonance frequency during one revolution (Rev. #6). Even though scattering of data points is appreciable, the lower boundary of the detected frequency values is indicating a continuous profile versus altitude. The scattering of data can be attributed to noise that may be impressed on the antenna. The noise frequency could be in audio frequency range. The impressed noises on the r.f. signal at the antenna can be detected like resonance points even the frequency is completely different from the UHR resonance frequency. When the spacecraft were passing through the shadow region, the data scattering was disappeared. When the spacecraft is in the sunlit region, the solar cells and the electrical circuits in the spacecraft are connected through the diodes in the power supply circuits, while the diodes are cutoff in the shadow region. This suggests that the noise came from the electrical circuits in the spacecraft itself through the solar cells into the surrounding plasma medium. The noise levels at the antenna can be estimated to be 1–4 mV/m inferred from the scattering of the admittance values (see Figs. 92–94 and 96–98).

Once the minimum point is detected, the automatic detection of the resonance point is stopped during the swept-frequency period. This means that UHR resonance is to be the lowest possible frequency of the automatic detection under the supper imposed severe noise disturbances.

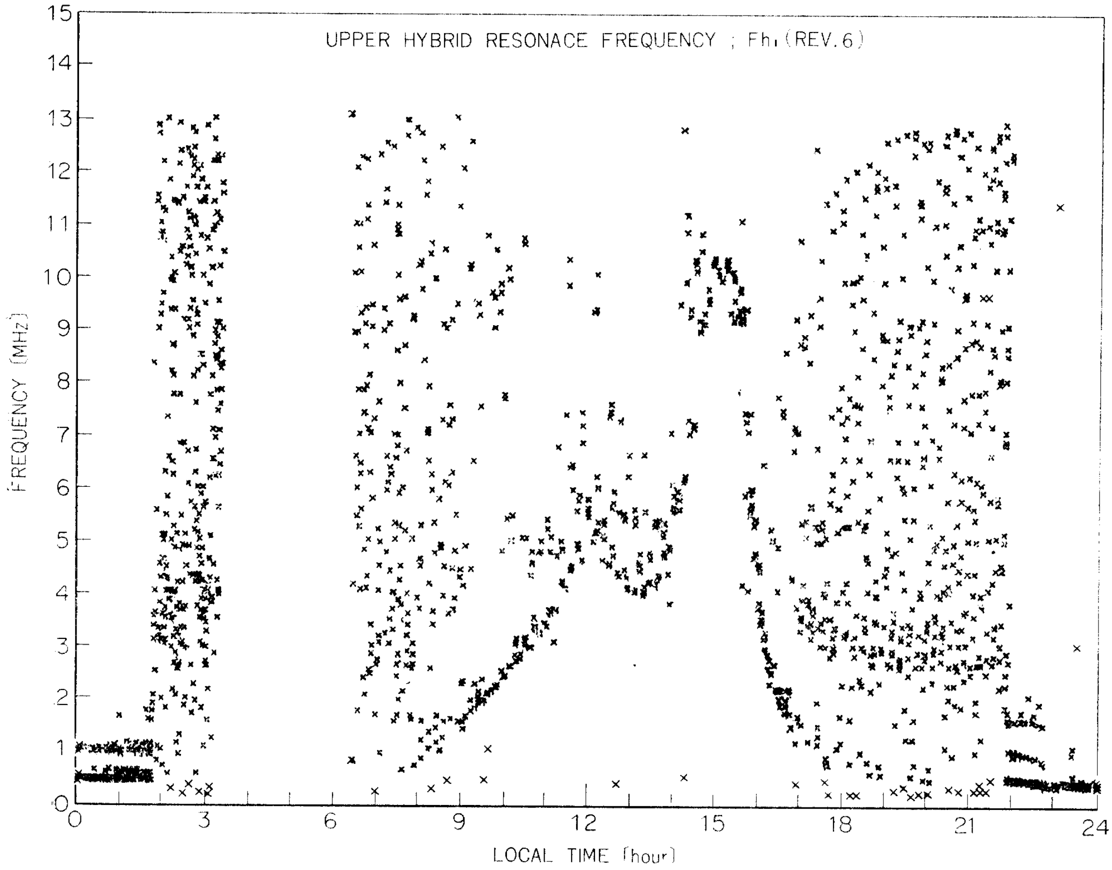

FIG. 90. Upper hybrid resonance frequency (Fh_1); rev. #6.

The electron density values can be deduced from observed UHR frequencies. The perigee point of the spacecraft orbit is at 13:35 L.T. and its altitude is 247 km. Before arriving and after passing this point, two maxima of the upper hybrid resonance frequencies were appeared. The altitude and the values of these peaks are corresponding to those of F2 peaks.

Sheath Resonance Frequency, Fh_2 Figure 91 shows the measured sheath resonance frequencies at the revolution #6. The admittance value of the the antenna near the sheath resonance frequency is high; the S/N ratio is therefore very high to avoid the misdetection of the resonance due to noise. In addition to the usual sheath resonance, the second and higher harmonics of the sheath resonance have been observed, as was the case for rocket borne gyro-plasma probe experiments. Assuming the magnetic field is perpedicular to the antenna surface, the sheath resonance frequency f_{UHR} is expressed as

$$f_{SHR}=\left(f_H^2+\frac{f_p^2}{1+C_s}\right)^{1/2} \tag{6.1}$$

where f_H and f_p are electron gyro-resonance and plasma frequencies. C_s is a sheath capacitance normalized by the antenna capacitance in free space. As is

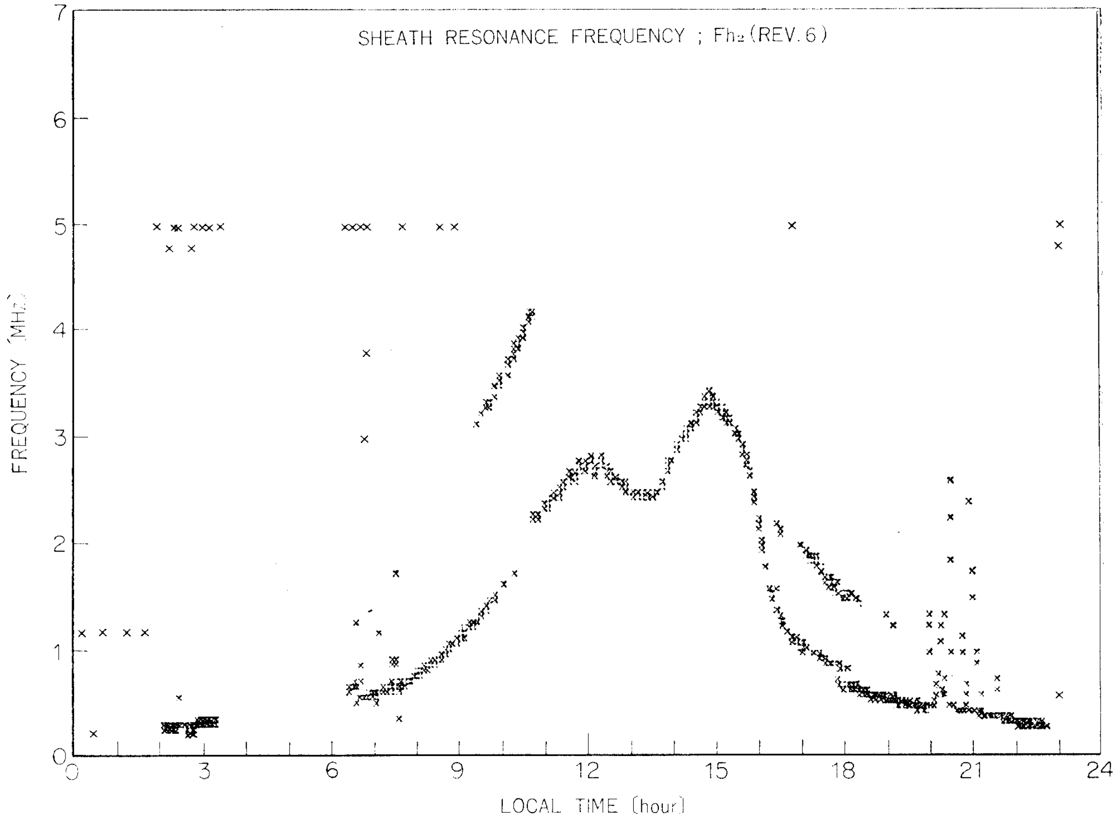

FIG. 91. Sheath resonance frequency (Fh_2); rev. ♯6.

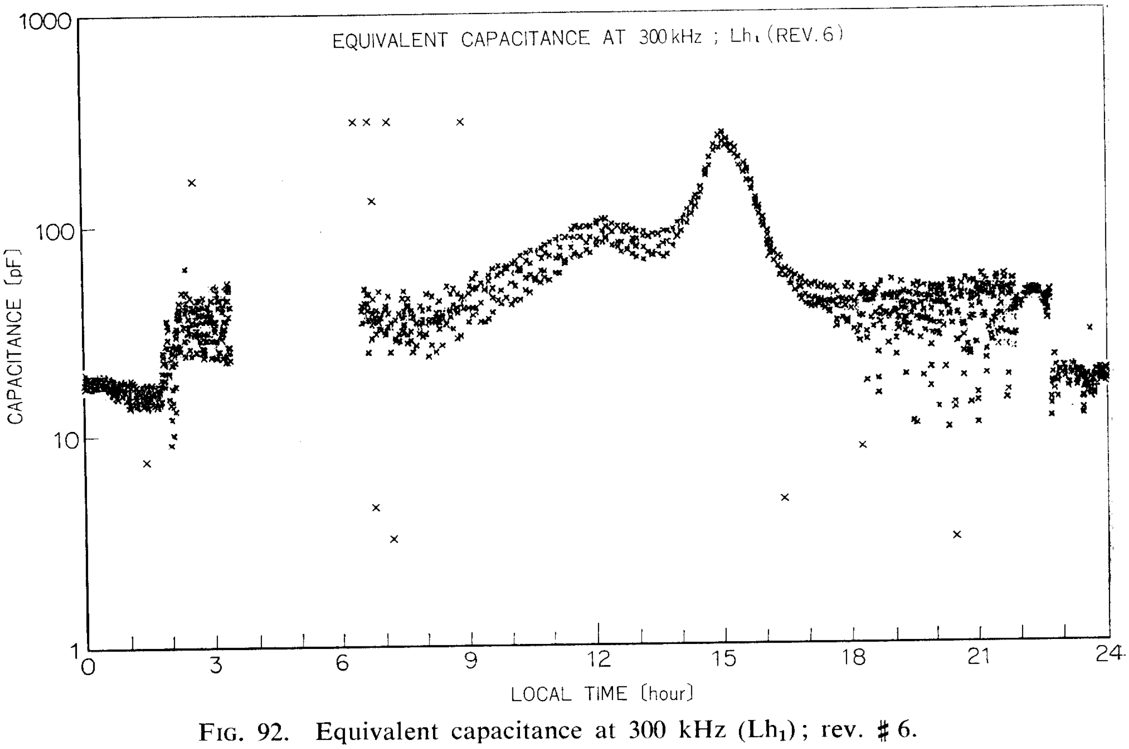

FIG. 92. Equivalent capacitance at 300 kHz (Lh_1); rev. ♯6.

obvious from this equation, the sheath resonance frequency increases as the gyro-resonance and the plasma frequencies increase. Namely, the sheath resonance frequency is correlated with the upper hybrid resonance frequency as has been shown in Fig. 91. Since the sheath capacitance C_s depends largely on the electron temperature, the electron temperature can be deduced from the observed sheath rsonance frequency using the known electron density and the strength of the geomagnetic field. But more accurate calculation for the sheath resonance frequency as a function of the electron density, temperature, the shape of an antenna, etc. should be required.

Admittance Value at 300 kHz, Lh_1 Figure 92 shows the variatoin of admittance values at 300 kHz during the revolution #6. When the upper hybrid resonance frequency is much larger than 300 kHz, this admittance value represents the admittance of the ion-sheath which surrounds the antenna in a plasma. The formation of the ion-sheath is largely controlled by the difference of the thermal velocities between electrons and ions. Therefore, this admittance value that relates to the ion-sheath thickness depends on the electron temperature. The sheath resonance frequency is also the function of the sheath thickness; we can see, then, a relation between f_{SHR} and the admittance value of the sheath. This can be checked using the measured data. For an example, $f_{SHR}=3.305$ MHz, $f_{UHR}=$ 9.090–9.293 MHz at $14^h\ 41^m\ 15.25^s$ (L.T.), and then the sheath capacitance deduced from the sheath resonance frequency using eq. (6.1) is 183–192 pF, while value at 300 kHz is 185±7 pF.

When the upper hybrid resonance frequency is close to 300 kHz, to measure the admittance value at 300 kHz is much the same as a fixed frequency impedance probe. The minimum and maximum points of the values may be identified as the upper hybrid and the sheath resonances, respectively. The equivalent capacitance value can be used to deduce the electron density. In the case of the revolution #6 this minimum point was appeared at the altitude of 5955 km where the geomagnetic field intensity was 0.068 gauss, and then the electron density at that position was calculated to be $8.29\times10^2\,\mathrm{cm}^{-3}$.

The admittance value were abruptly changed when the spacecraft passed through the sun's shadow line due to the earth. This phenomena were also found clearly in the low frequency side ($Ll_{1\sim3}$). This is considered to be due to the antenna potential change with respect to the space potential. In the sunlit region, photo-emissions from the antenna surface reduces the accumulation of the excess electron even for the difference of the thermal valocities between electrons and ions. This effect lifts the antenna potential close to the space potential. The admittance value of the sheath increases as a result of the decrease of the sheath radius. The spacecraft or the antenna potential is largely controlled by the photo-emission effect as indicated by this result. This suggests that the electron density measurement with any static potential analyser should be carefully planned to avoid the potential change due to this photoemission effect in the very tenuous plasma region.

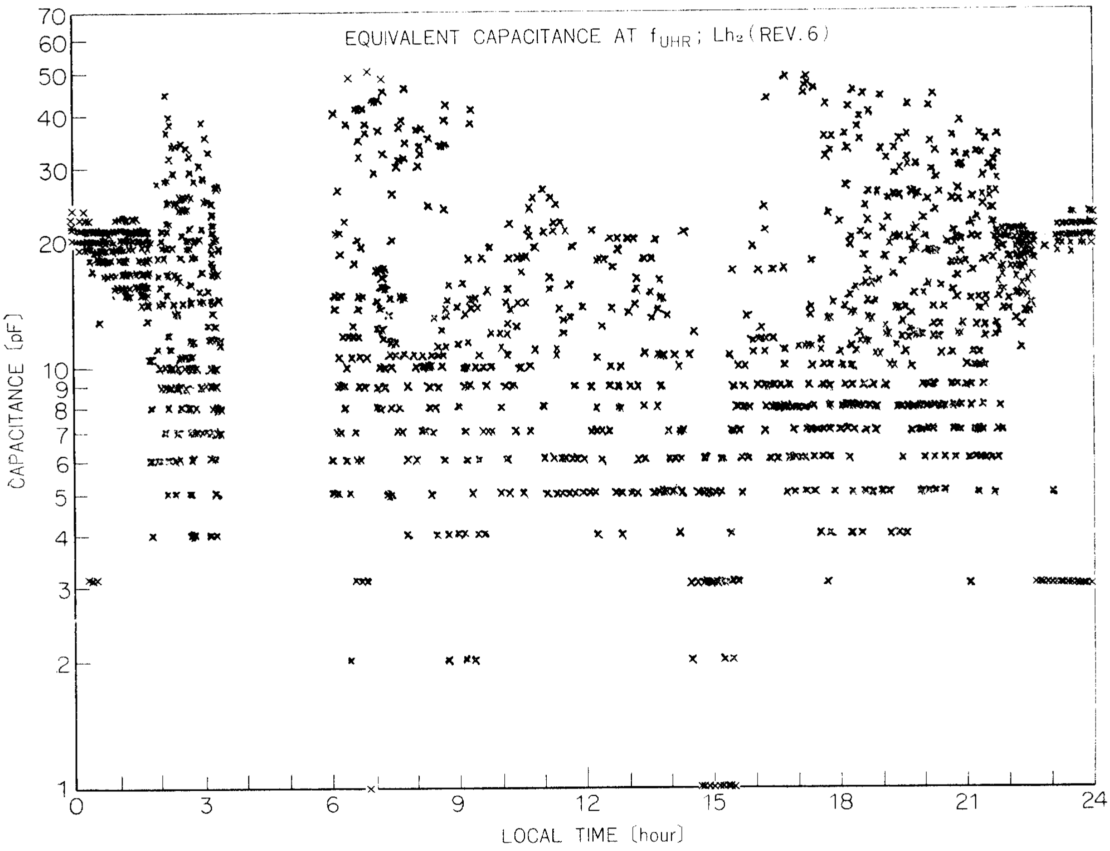

FIG. 93. Equivalent capacitance at f_{UHR} (Lh$_2$); rev. #6.

Admittanbe Value at f_{UHR}, Lh_2 Figure 93 shows the measured admittance at the upper hybrid resonance frequency. This admittance value is related to the Q value of resonance, that is, the values decrease as the Q value increase. The admittance value at the resonance is so small as to be masked by aforementioned noises in the sunlit region. It is obvious that the values decreased when the spacecraft passed through the F2 layer where the electron density increased. While the collision frequency becomes very low above the F2 layer, the Q value of the resonance decreased. This indicates that the some dissipative mechanisms besides the collision may occur in a collision-free plasma [38].

Admittance Value at 13 MHz, Lh_3 Figure 94 shows the variation of admittance values at 13 MHz during the revolution #6. This is a monitoring output of the capacitance of an antenna in free space. The measured admittance is 26 pF in average that coincides with the antenna capacitance measured in the pre-flight operation test. When the upper hybrid resonance frequency was close to 13 MHz in the F2 layer, the admittance values were affected by the effect of plasma resonance.

Lower Hybrid Resonance Frequency, Fl Figure 95 shows the measured lower hybrid resonance frequency during the revolution #8. Since the admittance in the lower frequency region can be expressed by the parallel combination of the sheath

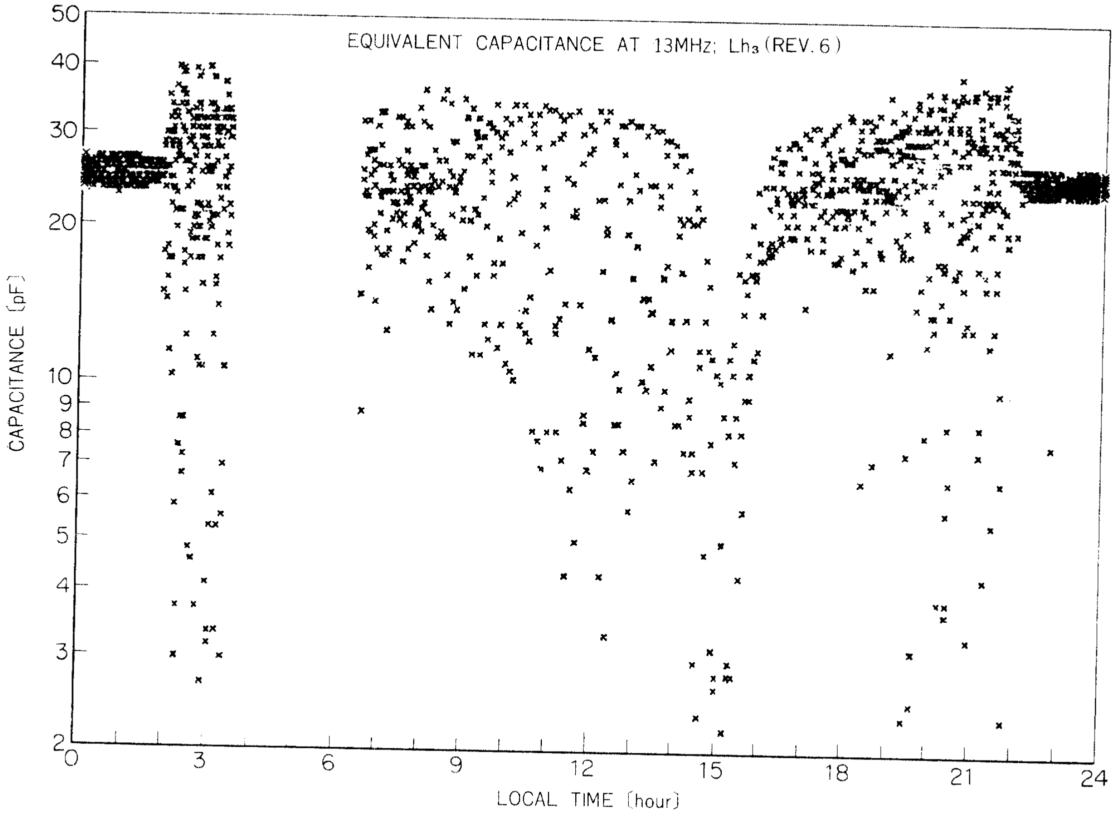

FIG. 94. Equivalent capacitance at 13 MHz (Lh_3); rev. # 6.

capacitance and resistance, the admittance value decreases as the frequency increases. As is mentioned before, the pseudo-resonances (noises) trigger the automatic resonance detection circuit for the lower hybrid resonance and this noises are logarithmically enhanced in the lower admittance values. Therefore, the lower boundary of the obtained data are considered to be the lower hybrid resonance frequency. This resonance detection did not operate in the lower altitude (<1000 km) due to the increased collisional effect and in the shadow region due to the increased potential drop. Using these data and eq. (4.1), the effective ion mass in the altitude range from 1000 km to 6500 km was computed. Assuming that the effective ion mass M_{eff} is equal to 2.0 along the ascending path (1000 km–4000 km) and equal to 1.0 along the descending path (6400 km–3000 km), the lower hybrid resonance frequencies are computed using the measured electron densities and the calculated geomagnetic field intensities along the spacecraft trajectory, being indicated in Fig. 95 by dotted lines. This result suggests that the heavy ions such as He^+ exist in the equatorial region up to 4000 km.

Admittance Values at 1.25 kHz, 3.80 kHz, and 6.65 kHz, Ll_1, Ll_2, and Ll_3 Figures 96, 97, and 98 show the admittance values at 1.25 kHz, 3.80 kHz, and 6.65 kHz measured by the low frequency gyro-plasma probe. As noted in IV-2.2,

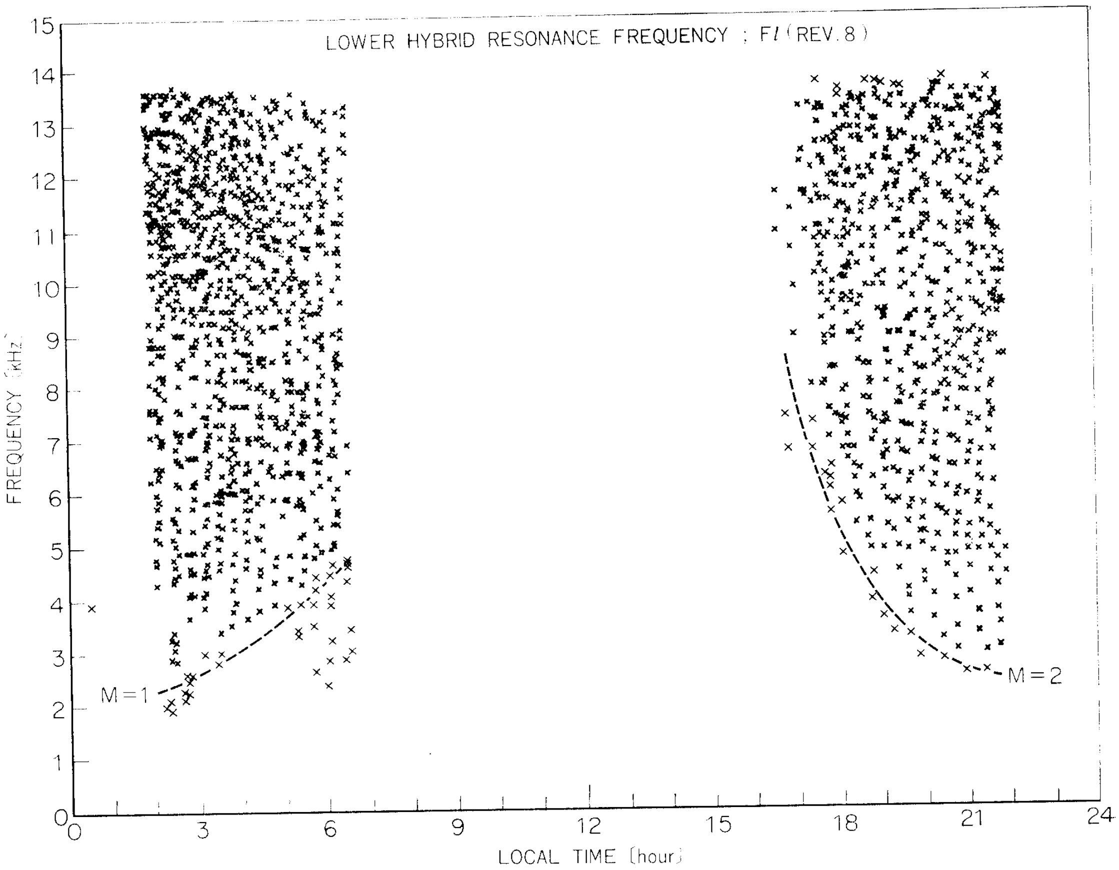

FIG. 95. Lower hybrid resonance frequency (F*l*); rev. #8.

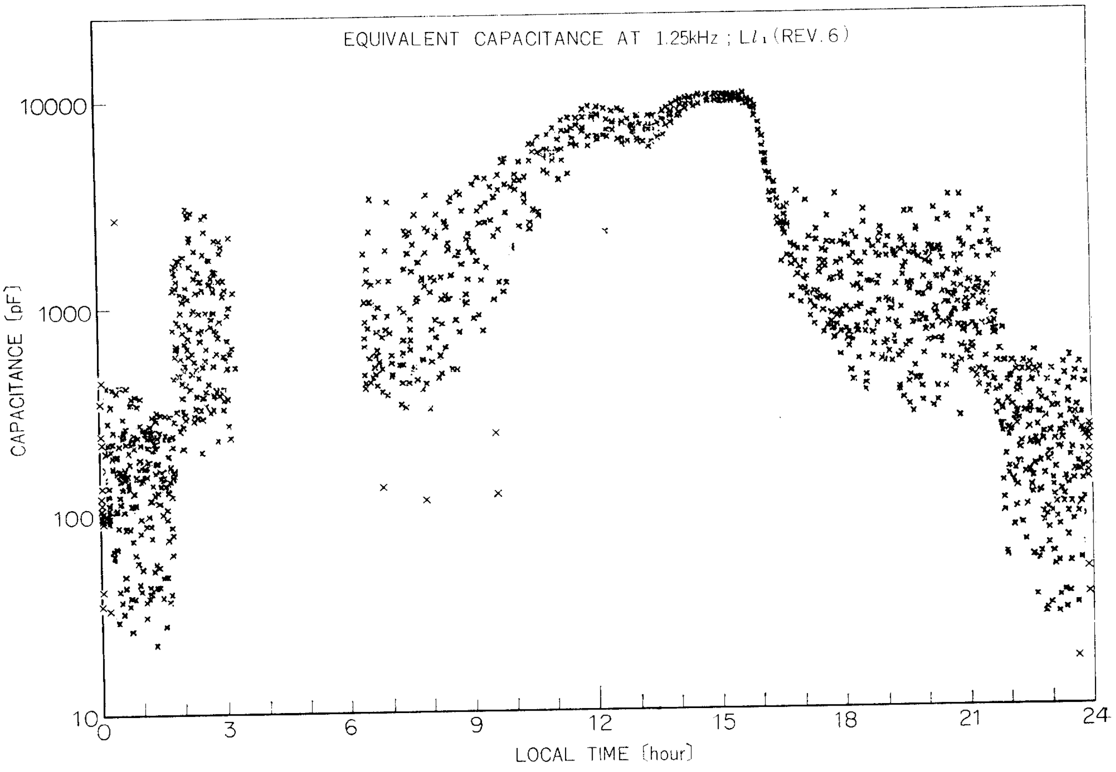

FIG. 96. Equivalent capacitance at 1.25 kHz; rev. #6.

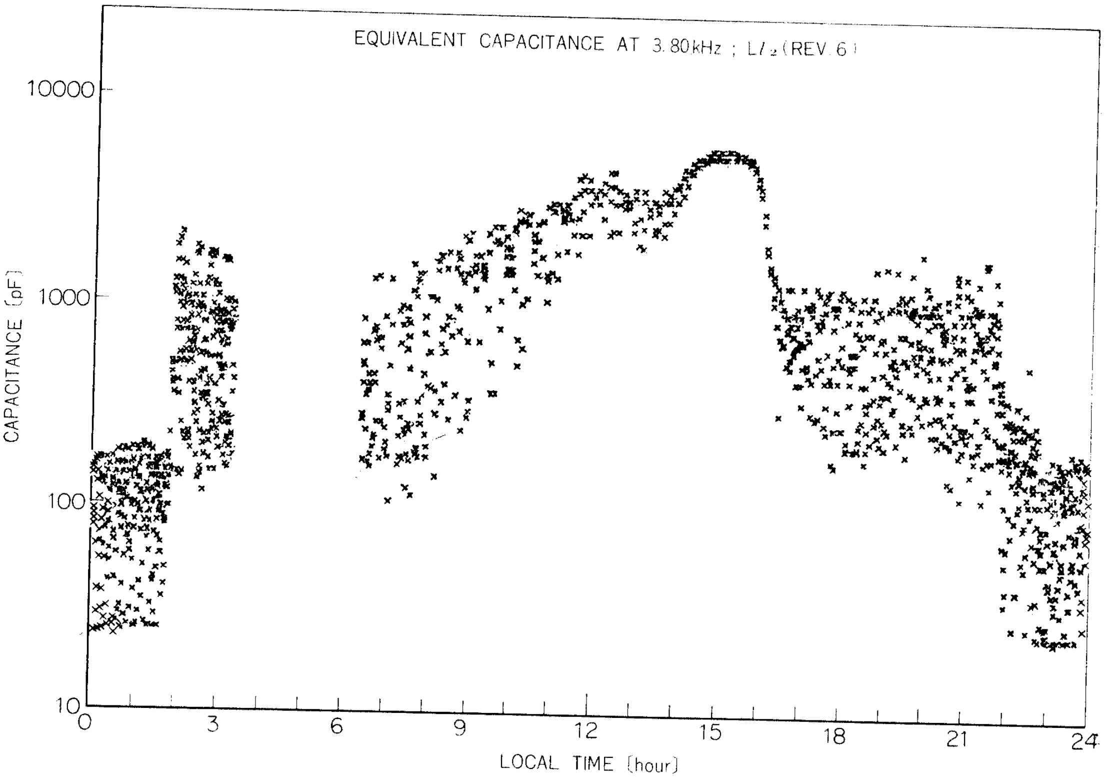

FIG. 97. Equivalent capacitance at 3.80 kHz ; rev. #6.

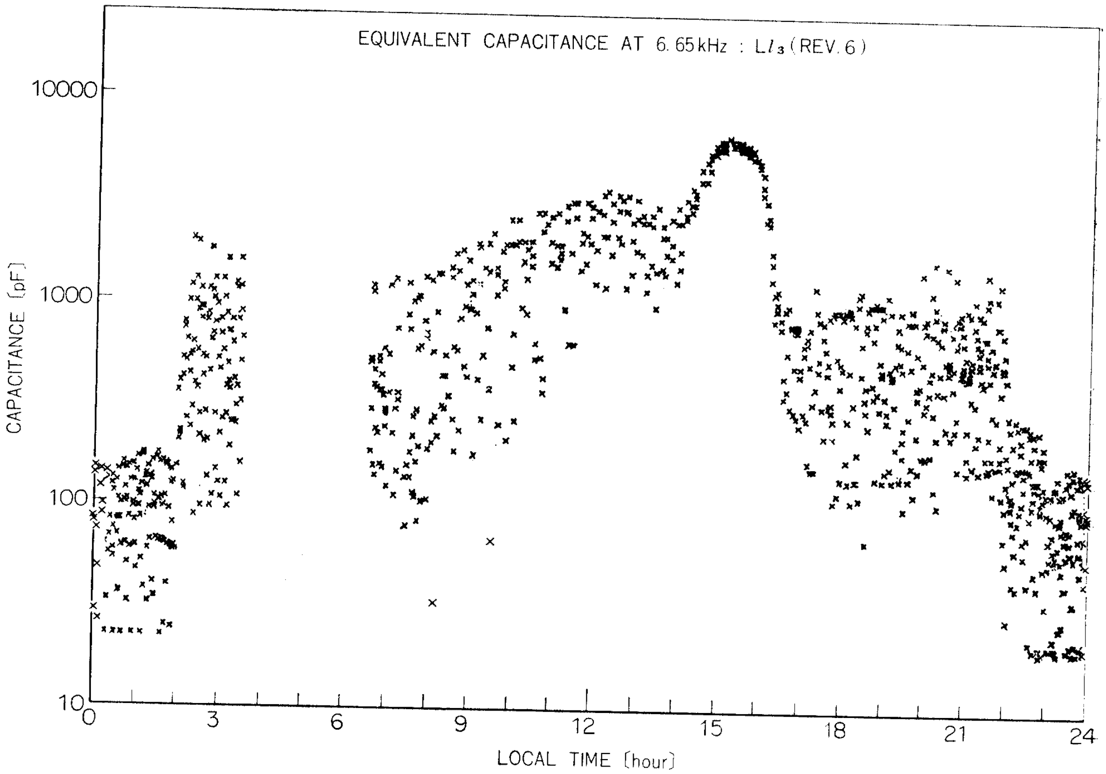

FIG. 98. Equivalent capacitance at 6.65 kHz ; rev. #5.

the admittance value in this frequency range increases as the sheath resistance decreases. The sheath resistance and capacitance are deduced from eq. (4.2). For example, the admittance values were 8103.5 pF at 1.25 kHz, 3557 pF at 3.80 kHz, and 2678.5 pF at 6.65 kHz at the altitude of 595 km where the electron density was 2.7×10^5 cm^{-3}. Using these values and eq. (4.3), the sheath resistance and capacitance are calculated, i.e., $R=600\ \Omega$–$680\ \Omega$ and $C=2100$ pF–2500 pF, and the condition $(\omega R)^{-1}>C$ is satisfied. The reason for the very low value of the sheath resistance is considered that the photoemission from the antenna metal surface acts to increase the conductivity in the sheath region. In the shadow region where the photoemission is cutoff, the sheath resistance abruptly increased to be of several hundred kilo-ohms and the sheath capacitance also decreased to be several tens pico-farads. As for the antenna potential with respect to the space potential in the case of the above example, the value of about −0.05 volts is calculated from eq. (4.3) if the electron temperature of 1500–2000°K is assumed. In this case, the computed floating potential of the antenna is about −0.5 volts. This difference of the antenna potential was also caused by the photoemission effect.

All observations were successfully carried out in the IPS experiment onboard the REXS. Operations of the automatic detection system were satisfactorily performed. The data for resonance frequencies and admittance values of an antenna in a magnetospheric plasma were obtained. Especially the detection of the lower hybrid resonance by the impedance measurement method has been made for the fist time. From these data, global electron density profiles and the ion effective mass can be obtained. The admittance values as a function of the electron density, the electron temperature and the antenna potential have been discussed. The photoemission effect on the antenna potential and its relation to the admittance values in a wide frequency range (1 kHz to 13 MHz) have been revealed. The noises from the spacecraft itself disturbed the signals to be detected, but the signals could be clearly discriminated from these noises.

VI-3 Electron Density Profiles in the Ionosphere

3.1 Topside region

From the measured upper hybrid resonance frequency, the electron density can be deduced, using the gyro-resonance frequency that is computed from the measured local geomagnetic field intensity at the satellite position. Figure 99 shows the calculated geomagnetic reference field intensities along the REXS orbit (solid lines) and the measured values with the flux-gate magnetometer (MGS [37]) onboard the spacecraft at the revolution #6. The geomagnetic field changes its intensity from about 0.039 gauss to 0.43 gauss. Since calculated values are good approximation of measured values, the geomagnetic reference field was employed to compute the gyro-resonance frequency. Assuming all the detected values (as have been shown in Fig. 90) to be the upper hybrid resonance frequency, the

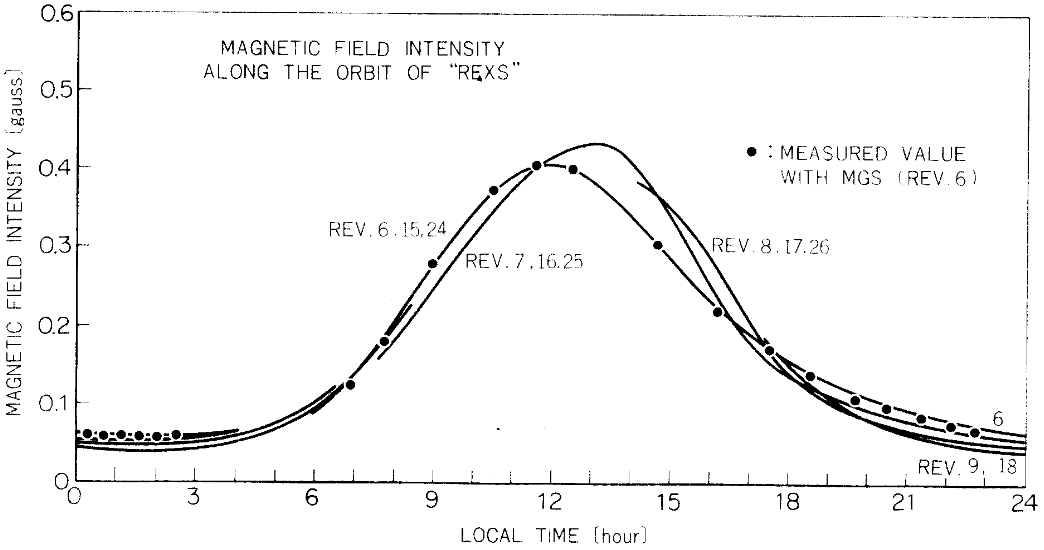

FIG. 99. Geomagnetic field intensity along the orbit of "REXS". The dots indicated on the curve are measured values with MGS.

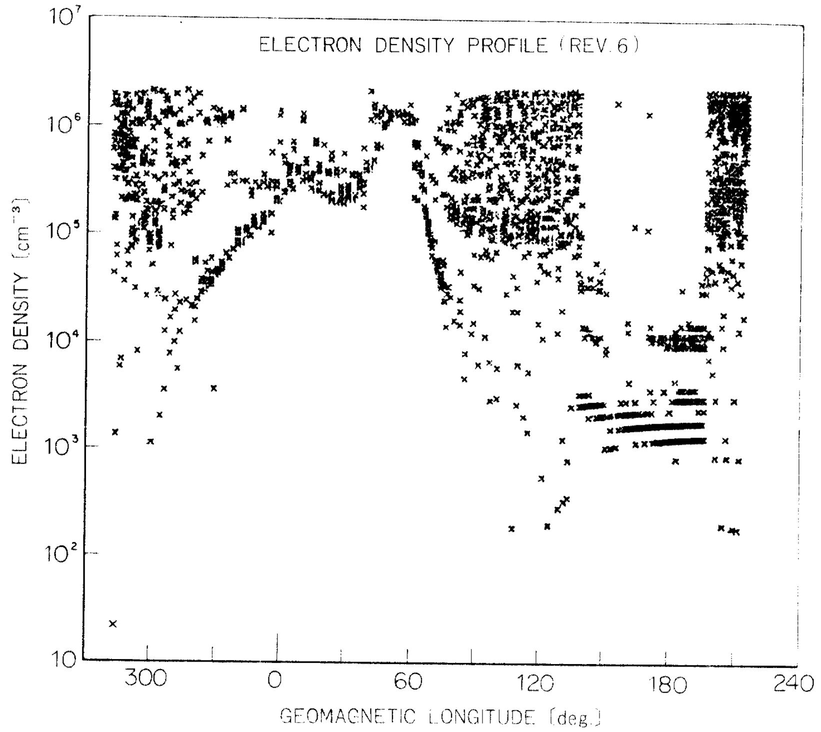

FIG. 100. Electron density profile deduced from measured values of f_{UHR} (see Fig. 90) during revolution #6.

electron density values versus the geomagnetic longitude are calculated and one example of the revolution #6 is illustrated in Fig. 100.

Figure 101 (a) and (b) show the altitude distributions of these values along the ascending and descending paths. As demonstrated in the previous section,

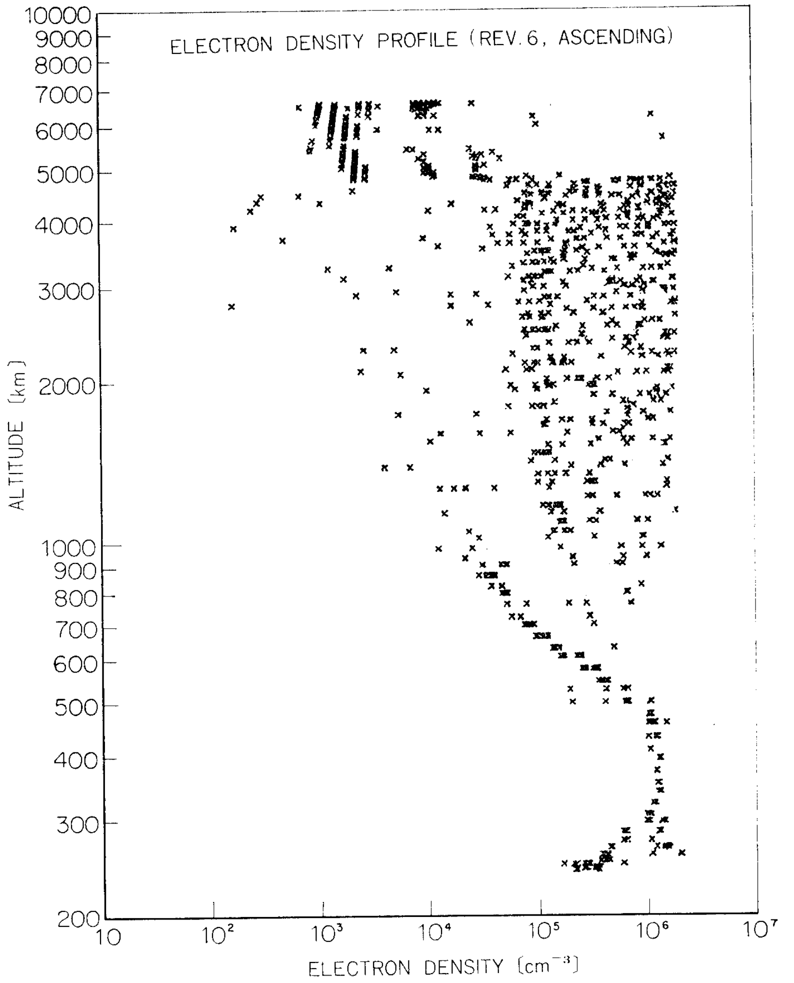

FIG. 101 (a). Electron density profile versus altitude; ascending path (rev. ♯6).

the lower boundary of these measured points show the electron density profile along the spacecraft orbit. All measured electron density profiles in the altitude range from 240 km to 6500 km are shown in Fig. 102(a) and (b), corresponding to the ascending paths and the descending paths, respectively. Since the spacecraft trajectories of the revolution numbers of n and $n+9$ (n; integer) take approximately the same condition with respect to the solar coordinate, the groupings of the same orbit (for example, the revolution numbers #6, #15 and #24) are made in these figures. Local times at the spacecraft positions when the measurements were carried out are computed and shown in the figures. From the resonance frequencies revealed by fixed frequency admittance values at 300 kHz, electron densities at the altitude of about 6000 km were deduced and shown in the figure by the dotted circles, from which the solid lines are drawn in accordance with R^{-3} and R^{-4} power law models, where R is the radius vector along a geomagnetic field line.

As for the distribution of electrons and ions along the geomagnetic field line, J. J. Angerami and J. O. Thimas [*39*] gave the theoretical consideration about its diffusive equilibrium, taking into account the effect of the electric field that arises

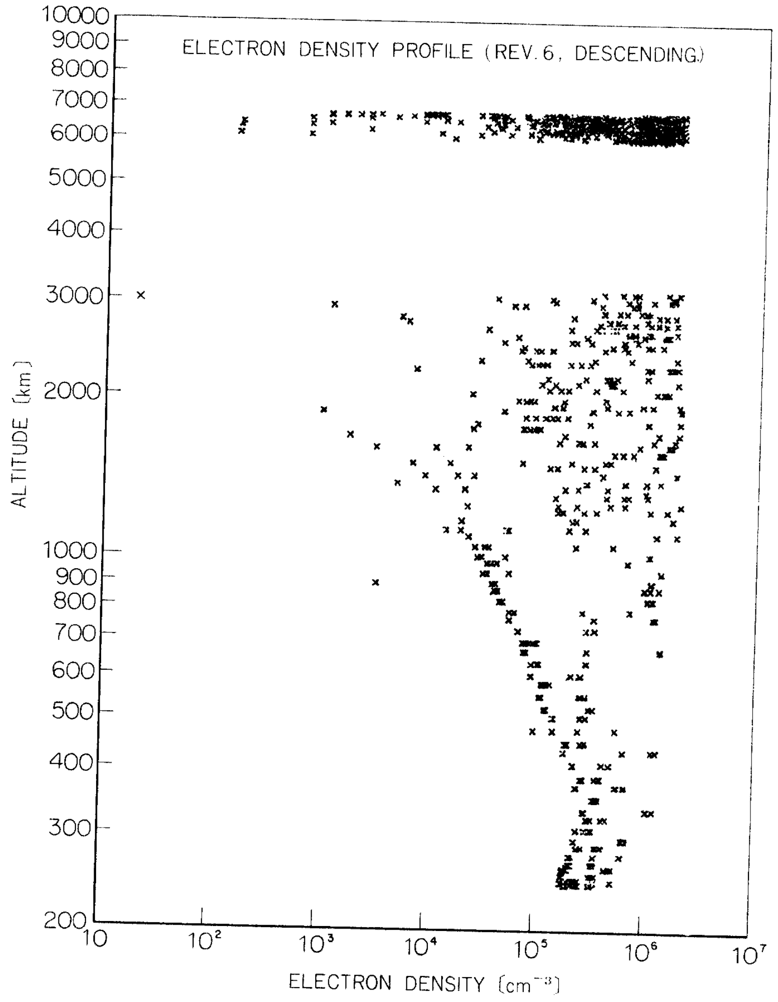

FIG. 101 (b). Electron density profile versus altitude; descending path (rev. ♯6).

from charge separation, the centrifugal force arising from the rotation of the earth, and the effect of the gravitational field. Figure 103 illustrates the relative electron and ion densities along a line of force as a function of the temperature-modified geopotential height z and the vertical altitude scale h for a constant temperature of 1500°K. Electrons and ions are assumed to be at the same temperature, and the ionic composition at the base level is given by $\eta_2=6.3\times10^{-3}$, and $\eta_3=1.6\times10^{-4}$ where η_2 and η_3 are the density ratios of He^+ and H^+ ions with respect to O^+ ion. The vertical electron distribution up to about 2000 km has been obtained by the gyro-plasma probes in the Lambda 3H-2, 5 and 6 sounding rocket experiments [*4*, *19*], and the theory of the diffusive equilibrium has been verified to be a good approximation of the observed electron density distribution. This theory is also applicable to the electron density profiles as shown in Fig. 102.

Following Bauer [*40*] and Eviatar et al. [*41*], the electron density profile of a collisionless or ion-exosphere model distribution is given by

$$N(R)=N_M \exp\left[-\frac{R'}{H}\right]\cdot\left\{1-\left(1-\frac{B}{B_M}\right)^{1/2}\exp\left[-\frac{R'B}{H(B_M-B)}\right]\right\} \quad (6.2)$$

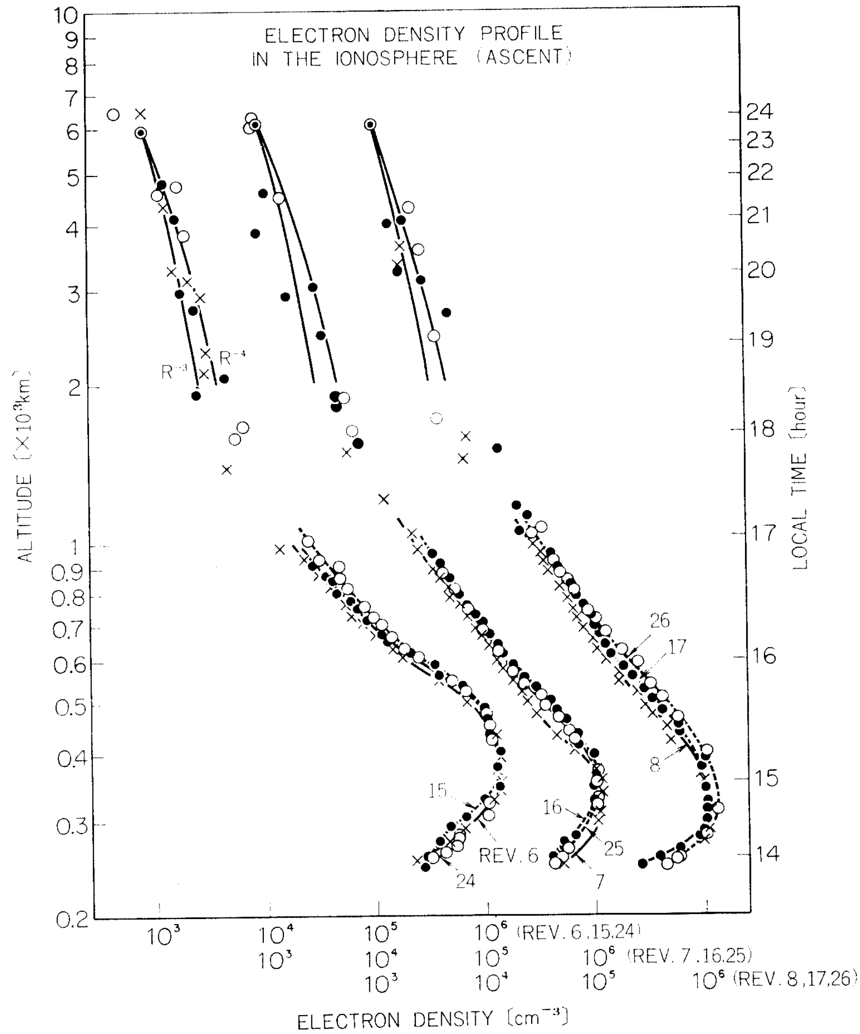

FIG. 102 (a). Electron density profiles versus altitude; ascending paths. The curves labelled by R^{-3} and R^{-4} are electron density distributions of the power law model of R^{-3} and R^{-4} where R is a geocentric distance along the geomagnetic field line. The dotted circles indicate the electron density value deduced from the resonances of Lh_1.

where B is the field strength of the magnetic field at the appropriate level, H is the scale height, R' is a geopotential length parameter, and the subscript M refers to a reference level below which a Maxwellian distribution is valid. This type of distribution is one which corresponds to a diffusive equilibrium (first term) [39], weighted by a function dependent on the intensity of the geomagnetic field (in curly brackets). Experimental data from knee whistlers [42, 43] are in good agreement with the empirical model of R^{-4} plasma density distribution from the high altitude towards the boundary of the plasmasphere; an R^{-3} power law approximates eq. (6.2) at great distances. In this experiment, the distributions of the measured electron density values above about 2000 km fit with the power law

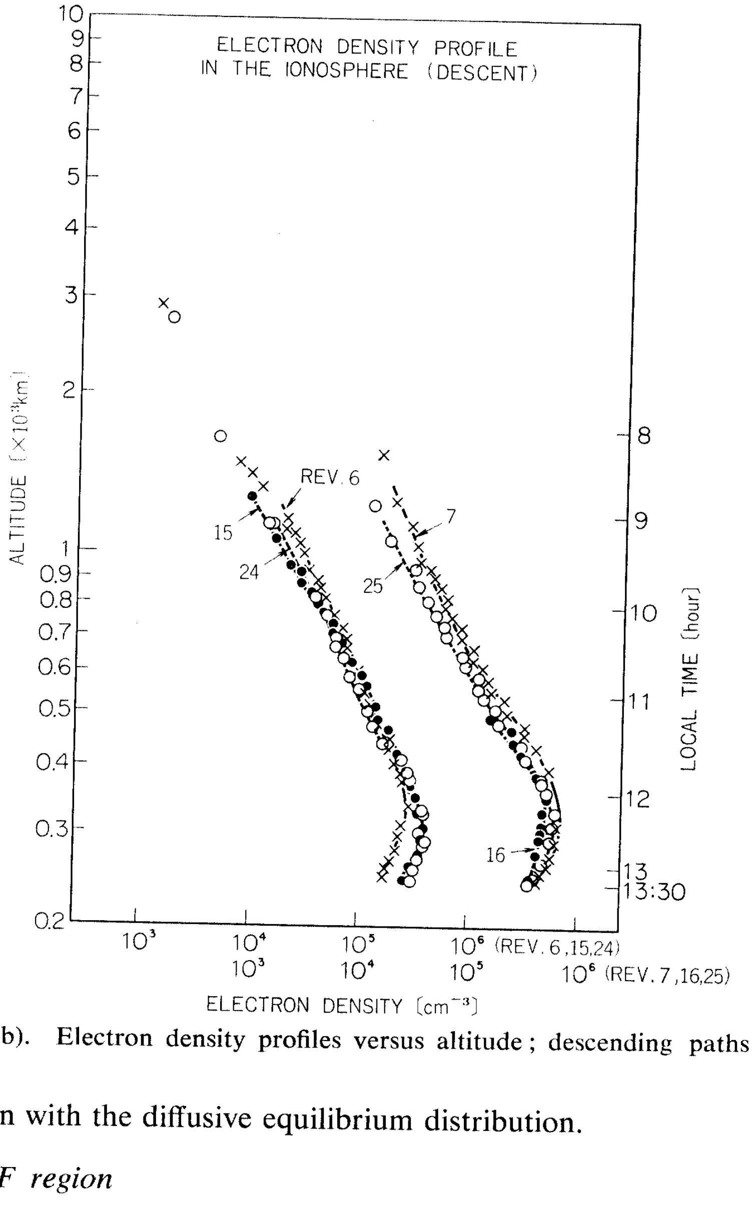

FIG. 102 (b). Electron density profiles versus altitude; descending paths.

models rather than with the diffusive equilibrium distribution.

3.2 Equatorial F region

As for the electron density profile in the region near the F layer, T. Yonezawa and H. Takahashi [*44*] gave theoretical considerations to the electron density distribution in the upper part of the F2 region and showed that the extended Chapman's distribution with a constant scale height gradient cannot be representative to the actual electron density distribution in the higher region above F2 peak. S. Chandra [*45*] developed a modified Chapman function with a variable scale height gradient, i.e.,

$$N(h)=N_m \exp\frac{1}{2}\left[1-\int_{h_m}^{h}\frac{dz}{H}-\exp\left\{-\int_{h_m}^{h}\frac{dz}{H}\right\}\right] \qquad (6.3)$$

where $N(h)$ is the electron density at height h and h_m is the height of the maximum electron density, N_m. The scale height H, here, varies as a function of the height; when the H value takes to be constant, eq. (6.3) is equivalent to the simple Chap-

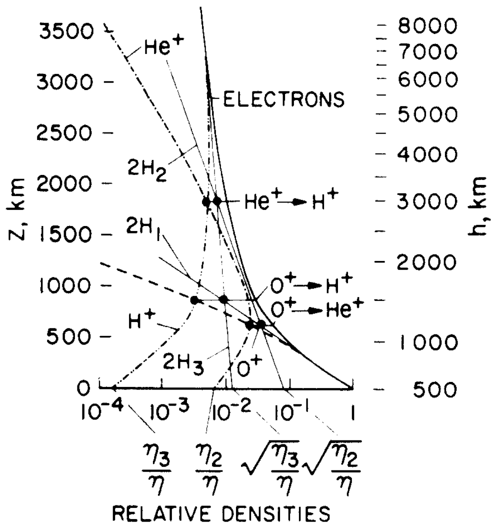

FIG. 103. Relative electron and ion densities along a line of force as a function of the temperature-modified geopotential height z and the vertical altitude scale h. η_1, η_2, and η_3 are the density ratios of the electrons, the He^+, and H^+ ions with respect to the O^+ ions. (after J. J. Angerami and J. O. Thomas [36]).

man function. To give the analytical form for the variable scale height, a modified Chapman function has been found to be in good agreement with the electron distribution obtained experimentally within the height range from about 100 km below the F2 peak to an altitude of about 700 km. In this experiment, the five different groups of electron density profiles near the F2 layer in the day-time were obtained. Although the little differences can be found within one group that includes three sets of observations along the same orbital phase, these distributions mainly controlled by the geomagnetic latitudes. Figure 104 shows the average distribution of the electron density profiles versus the altitude. During three-days observation, the geomagnetic and solar activities were much the same and were slightly disturbed conditions; the sum of Kp indices (Kp is a geomagnetic planetary three-hour-range index) are 22^+, 23^-, and 24^-, the relative sunspot numbers, Rz, are 54, 48, and 60, and the daily solar flux at 2800 MHz are 116.2, 117.9, and 119.5 ($\times 10^{-22}$ Wm^{-2} Hz^{-1}), corresponding to August 19, 20, and 21, respectively [*46*]. To refer to the variations due to the geomagnetic latitude, the geomagnetic latitudes at the altitude of 350 km are listed in Figure 104; the value of the group *a* is 23.7° north and that of the group *d* is 41.2°. Figure 105(a) and (b) show the geomagnetic latitude dependences of the heights of F2 peak and the maximum electron density values of F2 layer. As is evident from the figures, the maximum electron density and the height of F2 peak increase with the decrease of the geomagnetic latitude. The local time dependence of these values is considered to be negligible because the times when the spacecraft passed through the F2 peak are much the same; at 14:40 to 15:07 (L.T.) in the ascending phases and at 12:10

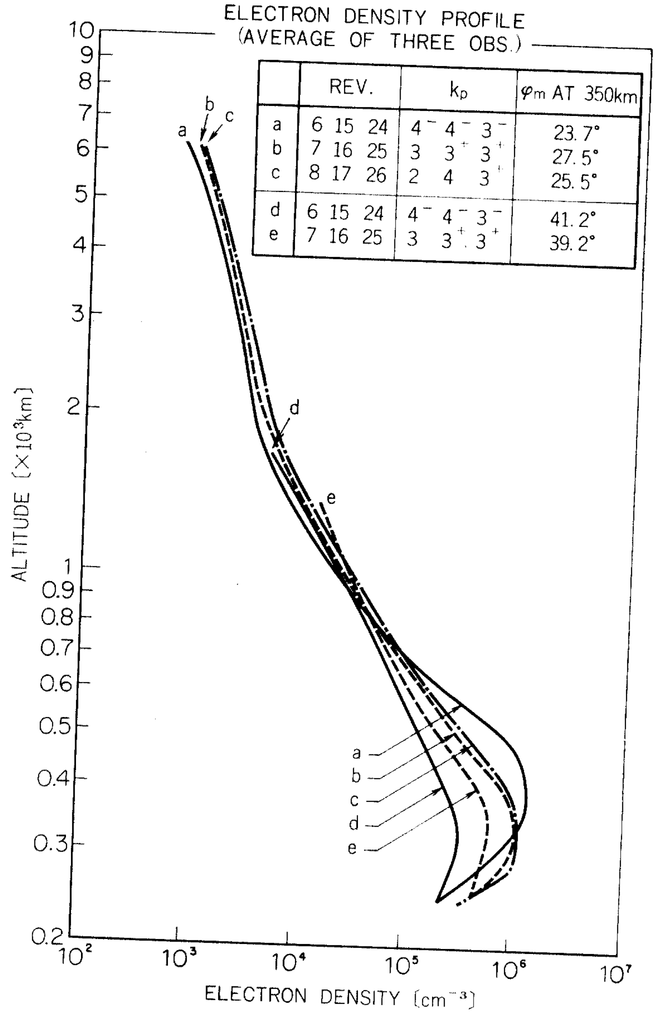

	REV.	k_p	φ_m AT 350km
a	6 15 24	4^- 4^- 3^-	23.7°
b	7 16 25	3 3^+ 3^+	27.5°
c	8 17 26	2 4 3^+	25.5°
d	6 15 24	4^- 4^- 3^-	41.2°
e	7 16 25	3 3^+ 3^+	39.2°

FIG. 104. Average electron density profiles of three sets of observation along the same orbital phase.

to 12:38 (L.T.) in the descending phases. Consequently, these changes in the electron density and the height of F2 peak are considered to be due to the geomagnetic control.

Figure 106 shows the latitudinal variation of electron density at the altitude from 250 km to 900 km, in terms of electron densities at the constant altitude versus geomagnetic north latitude. Figure 107 represents the contour map of the constant electron density in the altitude-latitude domain. The local time along the spacecraft orbit as given in the same figure, varies from about 10:00 to 13:00 in the descending phase and from about 14:00 to 17:00 in the ascending phase. Since there is no large difference of the local time in the obtained data around the low latitude, enhancements of electron density in the middle latitude towards the equatorial region are due to the well-known equatorial anomaly (A. J. Lyon and L. Thomas [*47*], G. E. K. Lockwood and G. L. Nelms [*48*], J. W. King et al. [*49*], Chan [*50*], and Jackson [*51*]). In the high latitude, the electron density in the F2 region

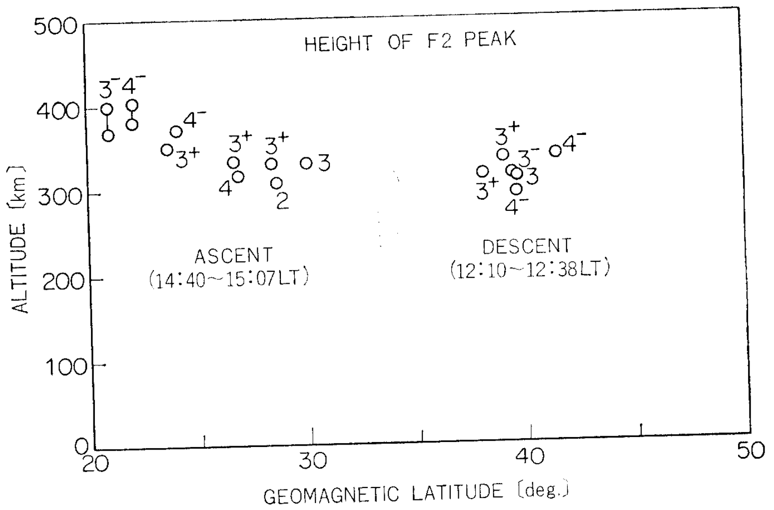

FIG. 105 (a). Geomagnetic latitude dependence of F2 peak; height of F2 peak.

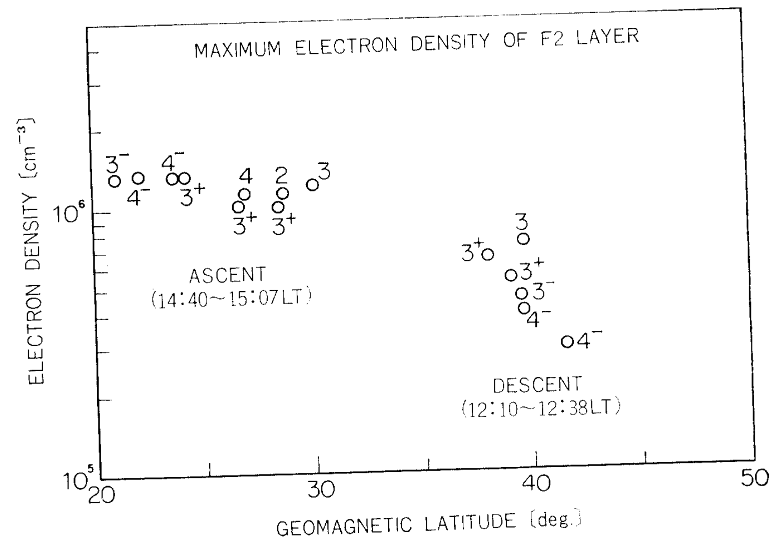

FIG. 105 (b). Geomagnetic latitude dependence of F2 peak; maximum electron density of F2 layer.

decreases; the high density region exists in the mid-latitude around the magnetic dipole latitude of 20° to 30° (see Fig. 107).

Assuming diffusive equilibrium along field lines, that altitudinal and latitudinal gradients of ion temperature *Ti* and electron temperature *Te* are negligible, and that the geomagnetic field can be represented by a dipole field, the scale height along the field lines *Hs* may be written (S. Chandra and R. A. Goldberg [52]) as

$$\frac{1}{H_s} = -\frac{1}{N}\frac{\partial N}{\partial r} + \frac{\cot\lambda}{2Nr}\frac{\partial N}{\partial \lambda} \tag{6.4}$$

and

$$H_s = \frac{\kappa(T_e + T_i)}{M_{ig}}$$

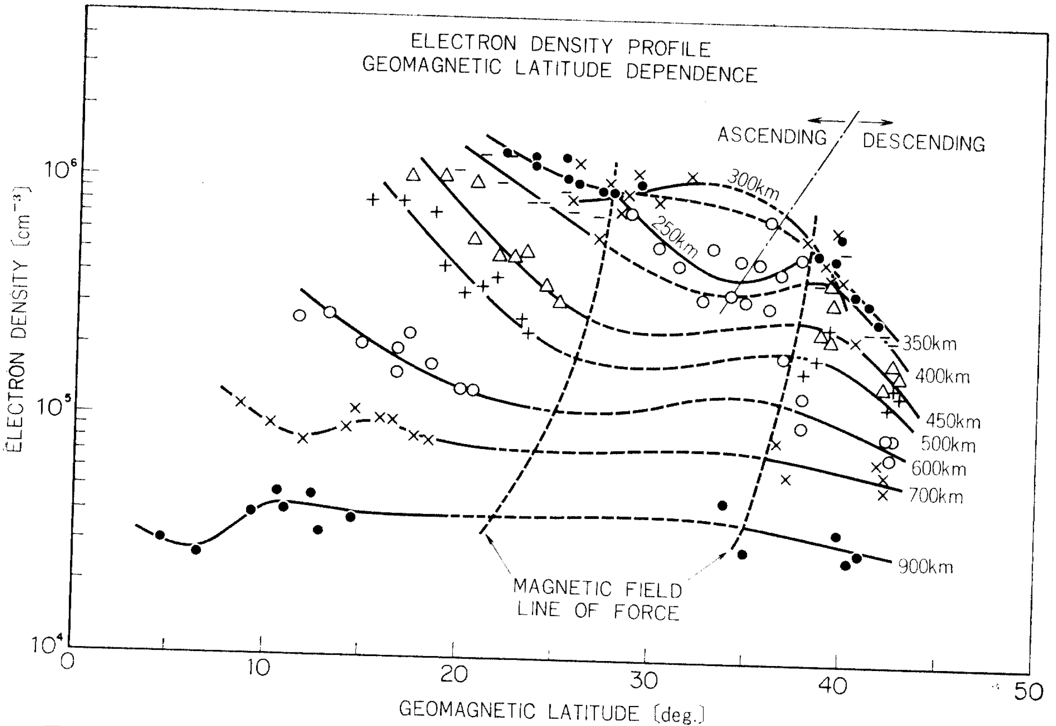

FIG. 106. Electron density profile; constant height versus geomagnetic latitude.

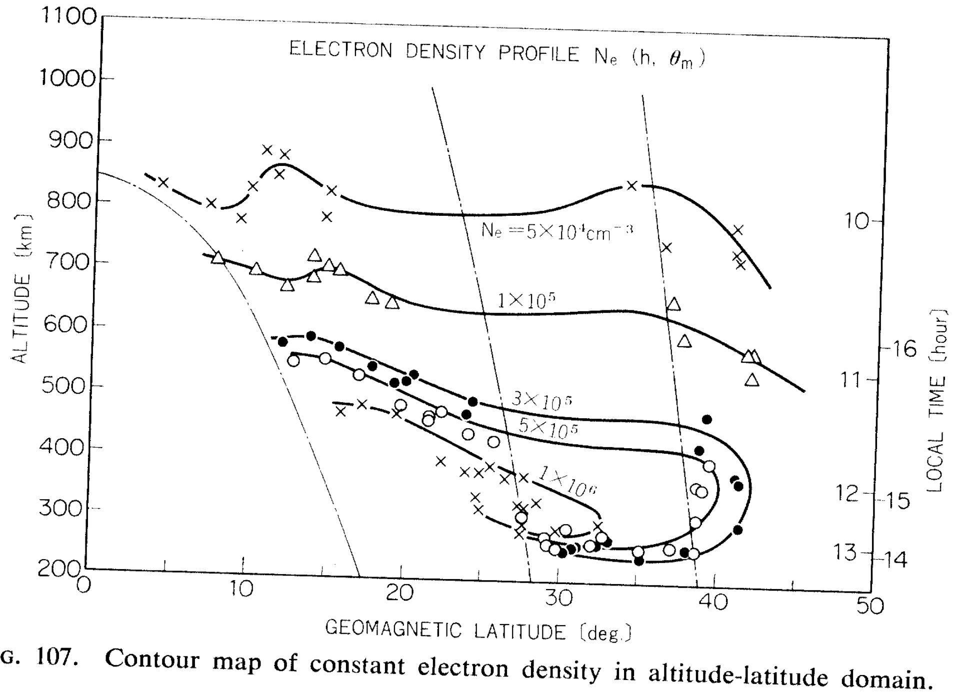

FIG. 107. Contour map of constant electron density in altitude-latitude domain.

where r is geocentric distance, λ geomagnetic dip latitude, M_i mean ionic mass, and g gravitational constant. Using above equations, the scale height H_s can be deduced from the measured global electron density distribution. Figure 108 shows the contour map of the field aligned scale height H_s in the altitude-dip latitude

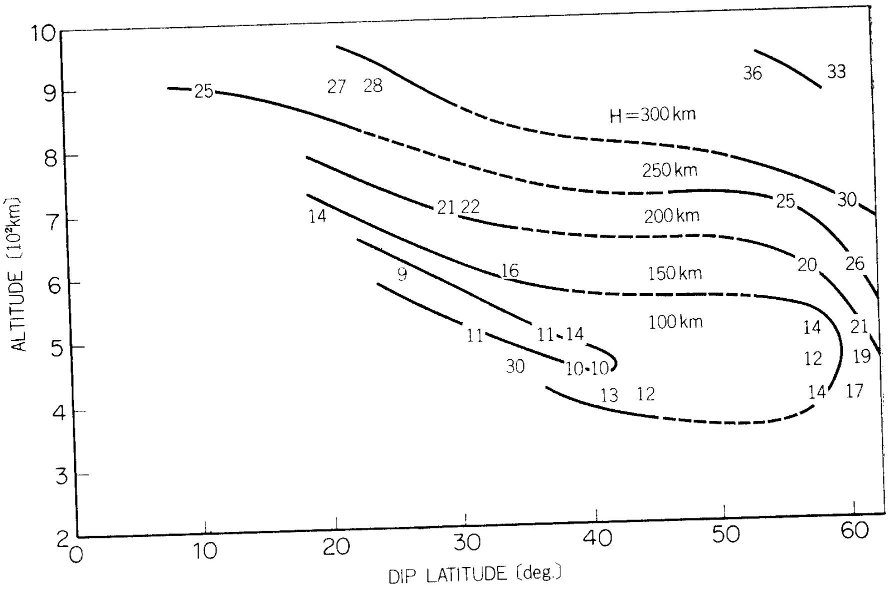

FIG. 108. Contour map of field aligned scale height.

domain. The effective ion mass can be obtained from the scale height *Hs* if the ion and electron temperatures may be deduced from the measured admittance values or the sheath resonance frequency.

Although the data were available in only northern hemisphere, it can be concluded that the electron distribution is clearly controlled by the geomagnetic field.

VII. DISCUSSION AND CONCLUDING REMARKS

The gyro-plasma probe onboard the Radio Exploration Satellite REXS launched on August 19, 1972, was performed successfully its designed mission in orbit, and gave the observational data of the upper hybrid resonance, the sheath resonance and the lower hybrid resonance frequencies with the admittance values, at given frequencies, of the antenna in the magnetospheric plasma. The electron density and the ion effective mass have been deduced from these data.

In Chapter II, a brief review on the gyro-plasma probe has been given mainly concerning the rocket borne experiments. The probe is characterized by high accuracy measurement of the elecvtron density that can be provided from the upper hybrid resonance; the artificial shift of resonance frequency due to the stray capacity has been eliminated by using the bridge circuit.

In Chapter III, the instrumentation of the gyro-plasma probe has been described in detail. To meet the time-sharing PCM telemetry system, onboard data processing circuits and the automatic resonance detection system were required. The gyro-plasma probe system onboard the REXS was divided into two channels; one is the channel of the high frequency gyro-plasma probe (the swept frequency range 0.2~15 MHz) to obtain the upper hybrid and sheath resonance frequencies, and the admittance values at 0.3 MHz f_{UHR}, and 13 MHz, and the other is low-frequency gyro-plasma probe (the swept frequency range 0.3~15 kHz) to obtain the lower hybrid resonance frequency and the admittance values at 1.25 kHz, 3.80 kHz, and 6.65 kHz. To perform stabilized detection of the resonance frequencies, the inhibit circuits to eliminate pseudo-resonance signals were appropriately installed. The estimated relative error of this electrical circuit system for measuring the electron density value was a few percent. Due to automatic operation of these circuits, the admittance values and the resonance frequencies were able to transmit with the low bit rate PCM telemetry system.

In Chapter IV, results of the pre-flight test of the operational characteristics were given. An instrument onboard the spacecraft should be subjected to pre-flight tests of the electrical and mechanical performances under various phase of the spacecraft missions. The thermal test in vacuum environments were carried out, adjusting the input heating and cooling conditions to simulate the estimated sunrise and sunset times, and the directional angle of the spin axis with respect to the sun. The laboratory experiment of the instrument in a plasma was carried out, using the space plasma simulation chamber, to check overall operation of the system in the plasma. The calibration data on operational performance of the instrument under the various conditions were acquired by these tests. The data were used for the correction of the real flight case for each observational item.

In Chapter V, the data processing and analysis systems aided by the digital computer were described. The established process are; (i) to give the formula for the computation of the spacecraft positions where the observations were carried out, (ii) to give the calculation of geomagnetic reference field, (iii) to calibrate the raw data using thermal data, and (iv) to convert the transmitted PCM data to the physical quantities corresponding to observational items.

In Chapter VI, preliminary experimental results are summarized. The performance of the rocket launching and the spacecraft, including the orbit of the spacecraft were given. The IPS instrument was successfully operated and all the measured values were acquired. The upper hybrid, the sheath, the lower hybrid resonance frequencies, and the admittance values in HF and VLF ranges exhibited the local time variations, the geomagnetic latitude dependence, and the changes due to altitude.

The photoemission effect on the admittance value of an antenna in a teneous plasma has been clarified, and it is concluded that the admittance of an antenna changes its value in accordance with the potential change due to the photoemission from the metalic antenna surface. The resonance frequencies were clearly discriminated from the detected pseudo-resonances by the inhibit circuits. The noise signals were enhanced when the spacecraft were in the sunlight. It is considered that noises came from the electrical circuits in the spacecraft itself through the solar cells into the surrounding plasma medium, and that the antenna received these signals. The characteristics of the noise, however, could not be identified clearly. The relation of sheath resonance frequency with respect to the admittance value at the lower frequency was examined. The second harmonic of the sheath resonance was also detected, which has been revealed by the rocket and the laboratory plasma experiments. The lower hybrid resonance frequency was detected, and the effective ion mass of about 2 along the ascending path (1000 km–4000 km) and of about 1 along the descending path (6400 km–3000 km) were obtained at the revolution #8. This LHR resonance detection did not operate in the lower altitude (<1000 km) and in the shadow region.

The electron density was deduced from the measured upper hybrid resonance frequency. The distributions of the electron density from the altitude of 240 km to 6570 km were obtained, and compared with the diffusive equilibrium distribution. The distribution of measured values above 2000 km were fitted to the power law model of the electron density distribution. The geomagnetic latitudinal dependence of the electron density distribution in the F layer has been confirmed, and the field aligned scale height were also deduced from the distributions of the electron density.

ACKNOWLEDGEMENTS

The IPS experiment has been carried out as a part of the REXS-satellite development and observation program; the authors wish to express their sincere thanks to Profs. Toru Ogawa and Iwane Kimura, for their integration efforts of the satellite equipment and regulation on the program operations. The development of the total satellite systems including the telemetry system have been done by the technological team of the Institute of Space and Aeronautical Science, University of Tokyo; the authors also thanks to Profs. Tamiya Nomura, Tomonao Hayashi, and Akio Ushirokawa, for their supports on this technological field. Helpful scientific discussions and comments have been obtained from Profs. Kunio Hirao, Susumu Kato and Dr. Atsuhiro Nishida; the authors also would like to express their thanks.

It should also be acknowledged that the successful operation of this satellite was due to the cooperative studies and work of the many scientists and engineers who have participated in this Mu 4S-4 experiment and the Radio Exploration Satellite "REXS" project, which have been supported by the Institute of Space and Aeronautical Science, University of Tokyo. The orbital data for this satellite were made available through the courtesy of the National Space Development Agency of Japan.

The authors are also grateful to their colleagues at the Institute of Space and Aeronautical Science, University of Tokyo; the Ionosphere Research Laboratory, Kyoto University; and the Meguro Laboratory, Meisei Electric Co.; especially Messrs. Osamu Furuta, Nobuyoshi Yokobori, and Makoto Abe for their contributions on the computer programming, experiments, and manufacturing works. The pre-flight simulation test of this system in plasma was carried out at the Space Plasma Chamber under supervision of the Space Plasma Committee, and the data

processing and analysis were performed on a digital computer (model HITAC 5020F) at the Computer Center, ISAS, University of Tokyo.

Department of Space Science
Institute of Space and Aeronautical Science
University of Tokyo
May 25, 1973

APPENDICES

A. Accuracy of Gyro-plasma Probe

As noted before, the gyro-plasma probe is designed to measure the antenna impedance in vector form, namely with amplitude and phase over a wide frequency range, and a capacitance bridge is employed in its sensor network in order to eliminate the disturbance due to stray capacity. The detailed circuit of the sensor network circuit is shown in Fig. A–1, in which the capacitance bridge with the antenna comprises the four capacitor arms of C_0, C_0, Ct and Cr including the variable capacitor MC 601Y ($C_0=C_s$ in eq. (1.1)).

The reduction of eq. (1.1) is made for the assumption that the gains of differential amplifier are equal. When the gains G_1 and G_2 of these channel is not equal, in general, the amplitude of the output potential e_0 of the differential amplifier is calculated as

$$e_0=\frac{C_s|C^*+C|}{(C_s+C_t+C)(C_s+C_r)}G_2e_i \tag{A.1}$$

where

$$C^*=(1-\beta)C_s+C_t-C_r,$$
$$C=C(\omega)$$
$$\beta=G_1/G_2$$

G_1 and G_2 are the voltage gains of the input FET amplifiers, and e_i is the amplitude of the input potential to the capacitance bridge. The capacitance bridge should be balanced by adjusting the variable capacitor MC 601Y, the gains of the input FET amplifiers to be $G_1=G_2$, and the input impedance of the differential amplifier to obtain eq. (1.1) and (1.3). The admittance A given in eq. (1.2) can be expressed by

$$A=\frac{A_aA_{sh}}{A_a+A_{sh}} \tag{A.2}$$

where A_{sh} is the admittance of the ion sheath, as given in eq. (1) of the previously published paper [14]. The admittance in the homogeneous region of the plasma A_a is given using the Balmain's expression as has been given in eq. (3) of the paper [14]. That is,

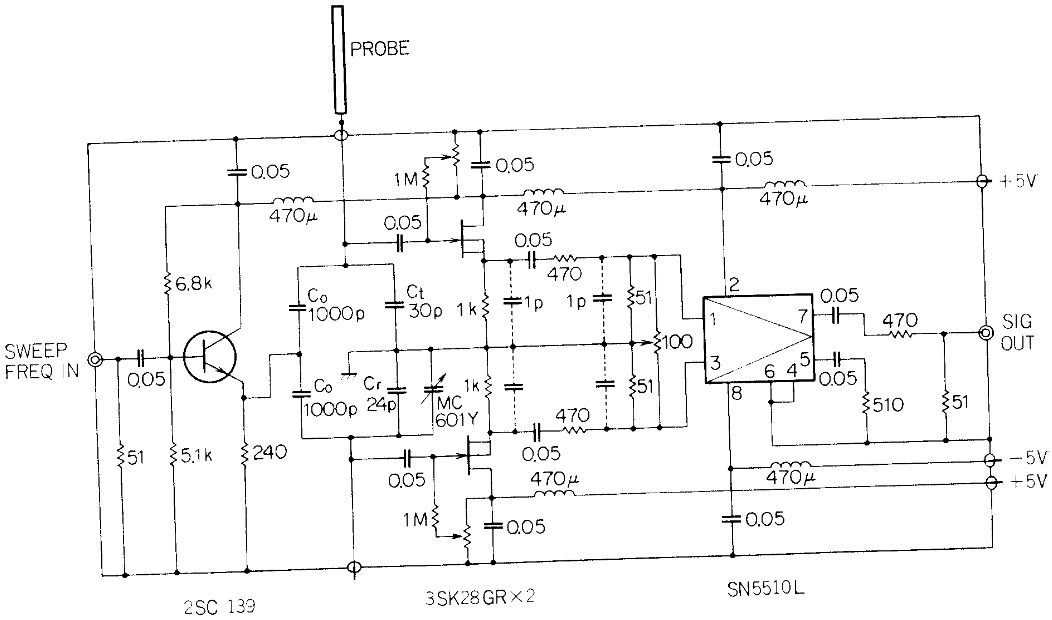

FIG. A-1. Sensor network circuit of gyro-plasma probe.

$$A_a = 2\pi j\omega\varepsilon_0 L\alpha^{-1}K_1\sqrt{F^*}\Big/\left[ln\frac{L}{r_{sh}} - 1 - ln\frac{\sqrt{F^*}+\sqrt{K_1}}{2F^*}\right] \tag{A.3}$$

where $F^* = K_1\sin^2\phi + K_3\cos^2\phi$, $K_1 = 1-\omega_p^2/(\omega^2-\omega_H^2)$, $K_3 = 1-\omega_p^2/\omega^2$ and $\alpha^{-2} = K_1/K_3$. In this equation, L and r_{sh} are the length of the cylindrical probe and radius of the ion sheath region respectively; ϕ is the angle between the cylinder axis and the geomagnetic field line. ω_p and ω_H are the plasma resonance and the gyro-resonance frequencies. The minimum values of the admittance appear at

$$\omega = \sqrt{\omega_p^2 + \omega_H^2} \tag{A.4}$$

and

$$\omega_{MPR} = \left\{\frac{(\omega_H^2+\omega_p^2) + \sqrt{\omega_p^4 + 2\omega_p^2\omega_H^2\cos\phi + \omega_H^4}}{2}\right\}^{1/2} \tag{A.5}$$

The value given by eq. (A.4) is the upper hybrid resonance and the value given by eq. (A.5) is the modified plasma resonance [*14*, *15*]. From the measured upper hybrid resonance f_{UHR} [MHz], then, the plasma frequency (i.e. the electron density N_e [cm^{-3}]) is determined using the computed gyro-frequency f_H [MHz] based on the magnetic field [*34*]

$$N_e = 1.24\times10^4(f_{UHR}^2 - f_H^2)$$

Bridge Unbalance and the Gain Unbalance The balancing of the capacitance bridge should be carefully adjusted to that C^* in eq. (A.1) becomes zero. But, if

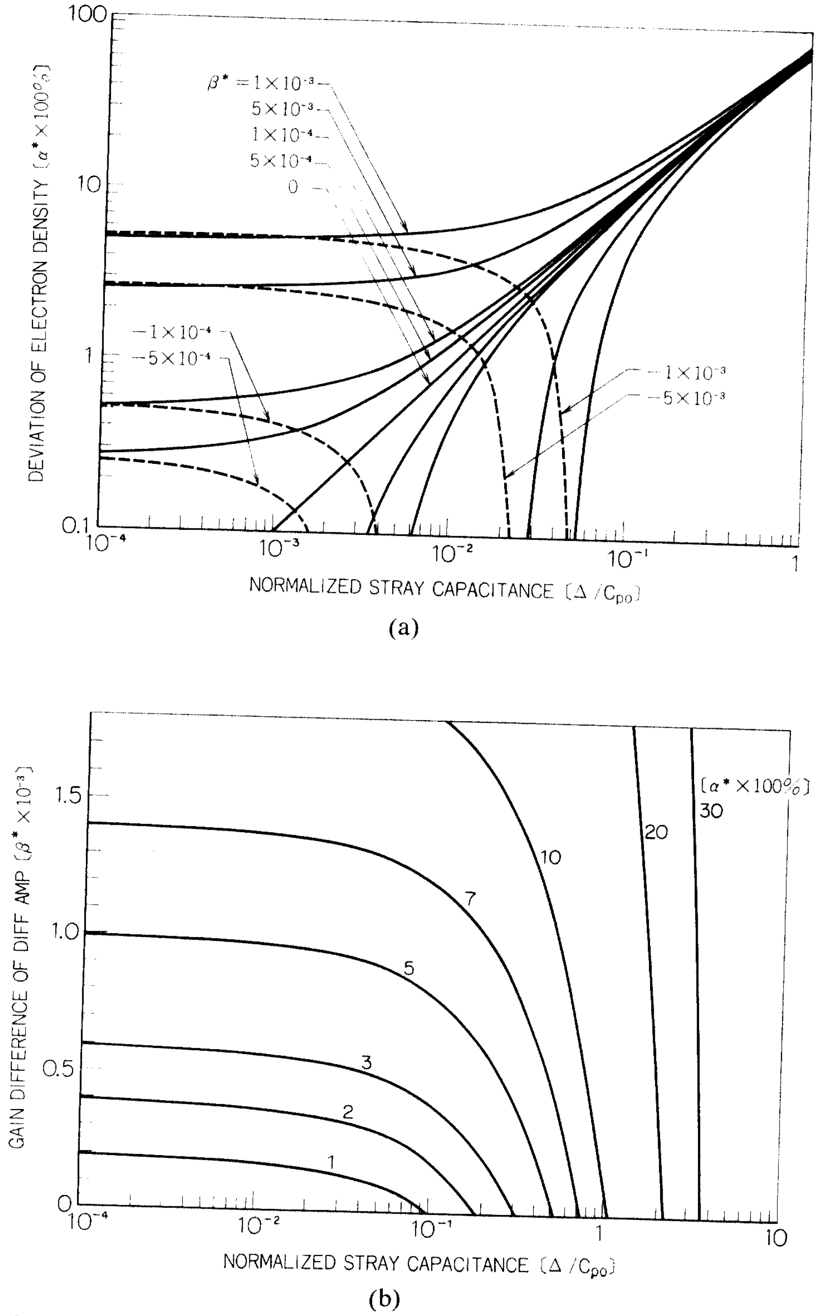

(a)

(b)

FIG. A-2. Deviation of electron density (α^*) due to gain difference of two FET amplifiers (β^*) and normalized stray capacitance (Δ/C_{p0}).

an unbalanced quantity still remains, the resonance frequency is shifted and the calculated electron density must be corrected. When ω^* is a root of the equation $e_0=0$ in the collisionless approximation, the deviation of the electron density is obtained from eqs. (7), and (10), as

$$N_e=(1+\alpha^*)N_e^* \qquad (A.7)$$

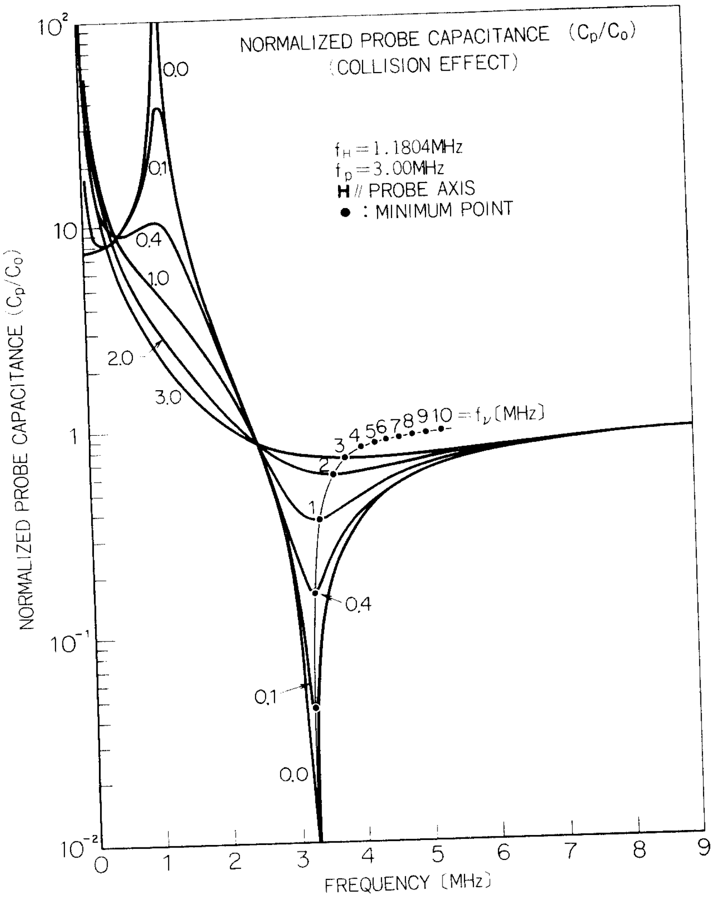

FIG. A-3. Normalized probe capacitance as function of frequency. Dots indicated on the curve show minimum values of probe capacitance corresponding to collision frequencies.

and

$$\alpha^* = \frac{C_{sh}}{C_{p0}} \cdot \frac{\Delta + \beta^*(C_s + C_r)}{\Delta + \beta^*(C_s + C_r) + C_{sh}} \qquad \text{(A.8)}$$

where $\Delta = C_t - C_r$; stray capacity

$\beta^* = 1 - \beta$; gain differencial ratio between two *FET* amplifiers

C_{p0}; antenna capacitance in free space

$C_{sh} \fallingdotseq 2\pi\varepsilon_0 L / ln(r_s/\rho - \rho/r_s)$, r_s: sheath radius

N_e^* is the estimated electron density assuming ω^* to be ω_{UHR}. Fig. A-2 (a) and (b) show the correction term α^* which is computed as a function of the normalized stray capacitance, Δ/C_{p0}, and the gain difference of two input *FET* differencial amplifiers, β^*. The parameters are chosen as $C_s/C_{p0} = 50$, $C_r/C_{p0} = 30$ and C_{sh}/C_{p0} 2.5. These results are indicating that the accuracy of $\pm 1\%$ can be achieved by eliminating the normalized stray capacitance to be 10^{-2} (-40 dB) and taking the gain difference of two input FET differencial amplifiers to be 2×10^{-4} (-74 dB).

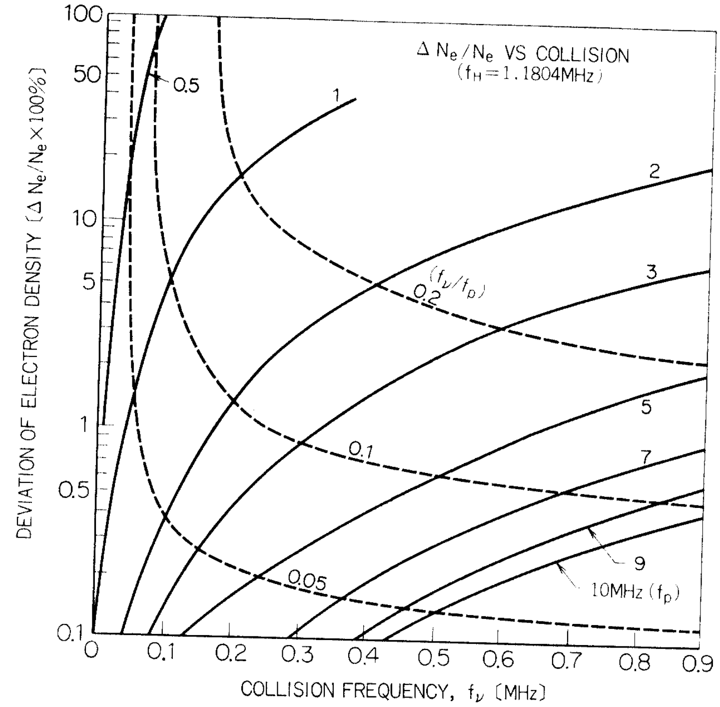

FIG. A-4. α-value versus collision frequency. Solid line shows constant plasma frequency and dashed line shows constant ratio of collision frequency to plasma frequency.

Resonance Frequency Shift due to Collision If the collision frequency is not negligible compared with the gyro-frequency and the plasma frequency, the parallel resonance frequency is shifted from the upper hybrid resonance frequency. Consequently, the electron density values deduced from the UHR resonance frequency should be corrected introducting the effects due to collision, especially in the lower ionosphere. Fig. A–3 shows the probe capacitance normalized by the capacitance in free space, sheath impedance being neglected. As the collision frequency increases, the frequency to give the minimum value of the probe capacitance also increases and the resonance curves are gradually flatten out. The deviation rate α of the electron density from that deduced for the collisionless case is defined as

$$\alpha \equiv \frac{\Delta N_e}{N_e} = \frac{\omega^{*2} - \omega_{UHR}{}^2}{\omega_p^2} \tag{A.9}$$

where ω^* is the angular frequency to give the minimum value of the antenna capacitance and $\omega_{UHR} = \sqrt{\omega_p^2 + \omega_H^2}$; the α value versus the collision is shown in Fig. A.4. If the gyro-frequency is less than the plasma frequency or the collision frequency, the asymptotic solution of this value can be obtained as

$$\alpha = \frac{\sqrt{1+2p^2} - 1}{2} \tag{A.10}$$

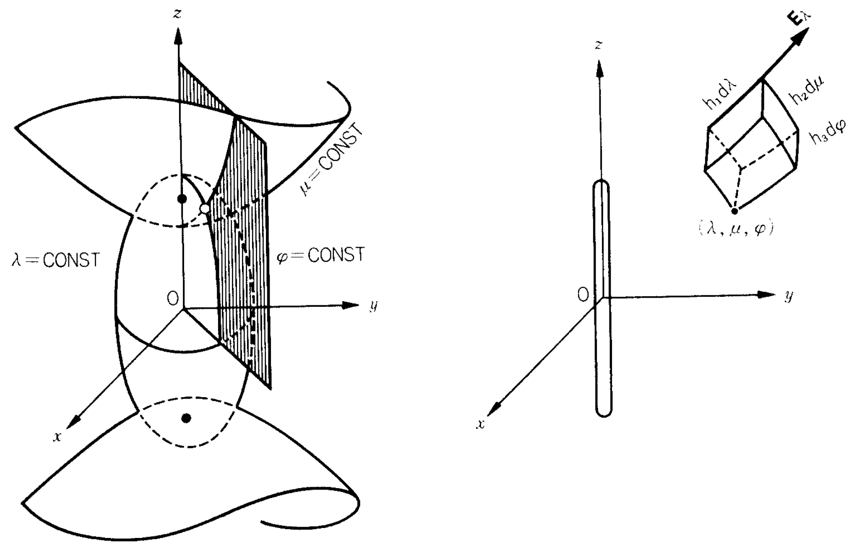

FIG. A-5. Prolate spherical coordinate system (λ, μ, ϕ).

where $$p=\nu/\omega_p.$$

The electron density N_e is equal to $(1+\alpha)^{-1}N_e^*$, where N_e^* is deduced assuming the resonance frequency to be ω_{UHR}. However, this correction factor is very small ($p \ll 1$) except in the lower ionosphere below about 100 km.

Resonance Frequency Drift due to Density Inhomogeneity The antenna in the space is considered to be immersed in the homogeneous plasma. It is practical, however, to examine the behavior of the antenna impedance in an inhomogeneous plasma because the ion sheath around the vehicle covers some part of the antenna when the vehicle's body acquires a negative charge. On the other hand, the error of the electron density measurement with r.f. probes due to the density gradient is serious problem in the laboratory plasma experiments.

The plasma frequency, here, is assumed to be a function of position and that the electrostatic field is expressed in the prolate spherical coordinate system (λ, μ, Ψ) as shown in Fig. A-5. The cylindrical antenna (length L and radius a) is approximately represented in this coordinate system as

$$\lambda_0=(L/2)/c \tag{A.11}$$

where $$c=\sqrt{(L/2)^2-a^2}.$$

The total admittance of an antenna is obtained by integrating the specific admittance over all space outside the antenna, then,

$$Y=\left[\frac{1}{j\omega 2c}\int_{\lambda_0}^{\infty}\frac{d\lambda}{\displaystyle\int_0^{2\pi}\int_0^1 \varepsilon(\lambda, \mu, \Psi)(\lambda^2-1)d\mu d\Psi}\right]^{-1} \tag{A.12}$$

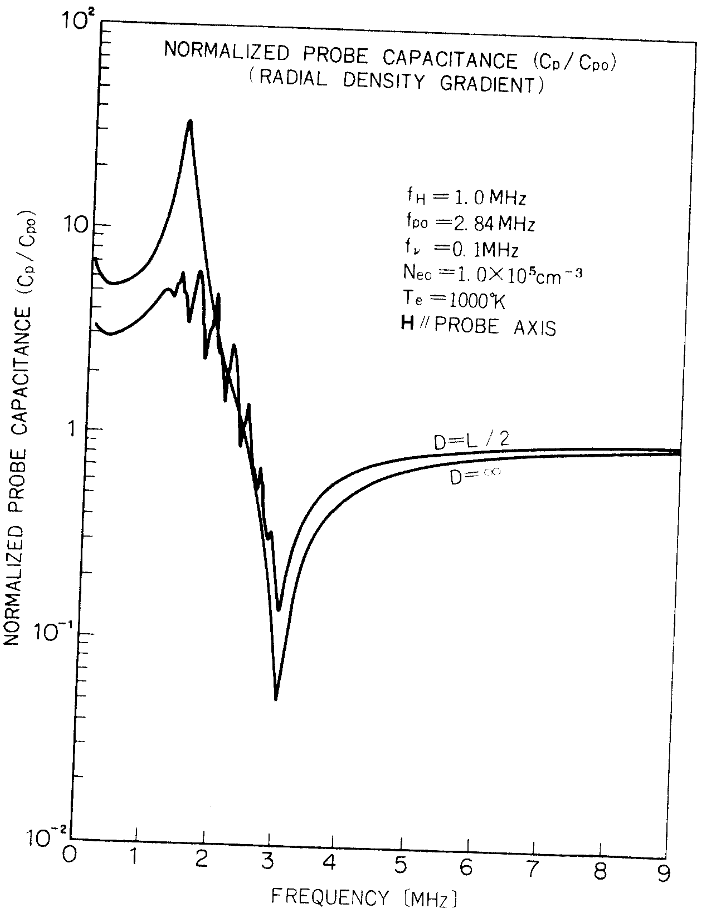

FIG. A-6. Normalized capacitance of a probe in an inhomogeneous plasma. Electron density gradient is assumed to be given by eq. (A.16).

where $\varepsilon(\lambda, \mu, \Psi)$ is a dielectric constant.

When homogeneity of the plasma such as the density gradient or the gradient of the static magnetic field exists in μ and Ψ directions, the above formulation is not an exact solution. To estimate the effect of the density gradient in measuring the electron density from the parallel resonance frequency of antenna impedance, it is, however, useful to compute the frequency response of the admittance given in eq. (A.12). Figure A-6 shows the admittance of a cylindrical antenna ($L=$ 2000 mm and $a=5$ mm) in a plasma, in which the radial gradient of the electron density distribution function is assumed as

$$N_e = \begin{cases} 0, & \lambda_0 < \lambda < \lambda_s \\ N_{e0} \exp\{(\lambda_s - \lambda)/D\}, & \lambda_s < \lambda \end{cases} \qquad \text{(A.13)}$$

where the sharp boundary sheath model is employed and λ_s is the distance of the sheath boundary from the antenna surface, and D is the e-hold distance of electron density gradient. The parallel resonance is just coincide with the upper hybrid resonance corresponding to the maximum electron density. When the density gradient in μ direction is assumed, the electron density deduced from the parallel

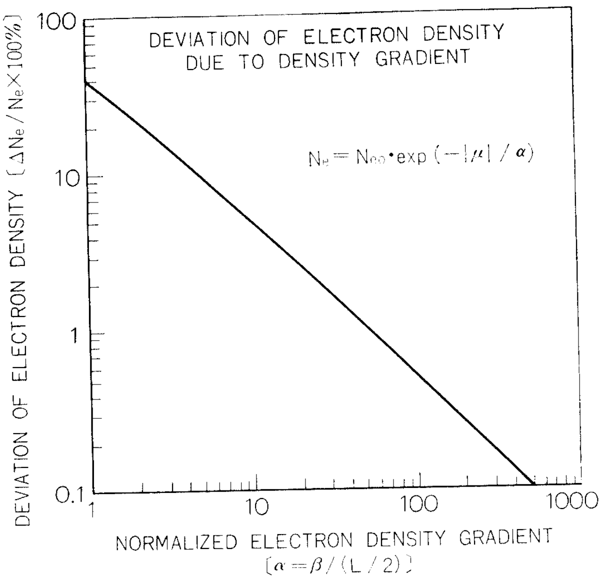

FIG. A-7. Deviation of electron density due to density gradient in μ-direction.

resonance is not a maximum electron density but an average value of the distribution function. In this case, the deviations of the measured electron density from the maximum value N_{e0} are calculated and the results are shown in Fig. A-7, assuming an $\exp(-|\mu|/\alpha)$ type of the electron density gradient, where α is the e-hold distance of the normalized electron density gradient, i.e., $\alpha=\beta/(L/2)$.

B. *Standard Pre-flight Test Conditions*

I. The standard test conditions of the each instrument

(1) Thermal Test:

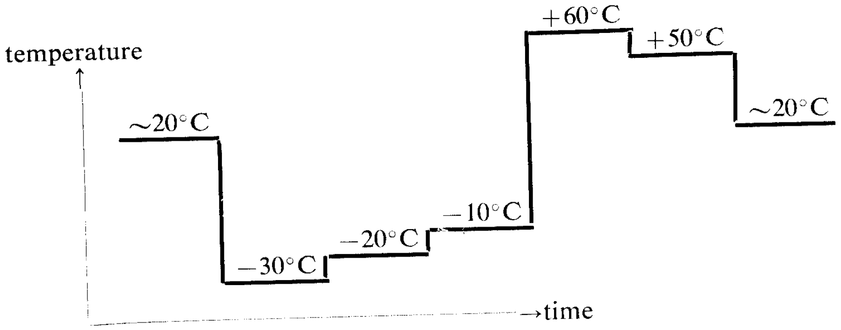

time interval of 6 hour at each stage of temperature

(2) Vibration Test:

Frequency	Axial	Lateral	Time
5~35 Hz	±15 mmp	±0.5 mmp	3 min
35~200 Hz	7.5 mmp	2.5 Gp	〃
200~2000 Hz	15.0 Gp	5.0 Gp	〃

(3) Acceleration Test:

Axial	+	30 G	3 min
	−	2 G	//
Lateral	±	5 G	//

(4) Shock Test:

Axial	+	25 G, 10 msec	half-wave sinusoidal, twice
Lateral	±	5 G, 10 msec	sinusoidal, twice

(5) Vacuum Test:

The pressure is below 10^{-3} mmHg for 6 hours at room temperature

II. The standard test condition of the spacecraft

(1) Thermal Test:

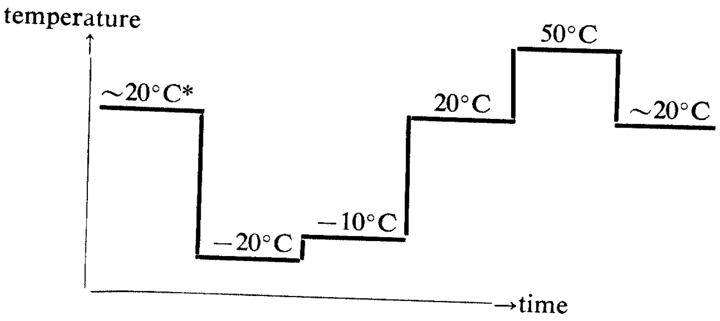

time interval of 6 hours at each stage of temperature

* about 40°C for exclusion of humidity.

(2) Vibration Test:

Frequency	Axial	Lateral	Time
5~35 Hz	0.4 mmp	0.13 mmp	3 min
35~100 Hz	2.0 Gp	0.67 Gp	//
100~400 Hz	2.5 Gp	0.83 Gp	//
200~2000 Hz	5.0 Gp	1.7 Gp	//

(3) Shock Test:

Axial	+	25 G, 8 msec	half-wave sinusoidal, twice

(4) Mechanical Construction (interface) of each part

(5) Electrical Interference Test
(6) Thermal Vacuum Test (see IV-2.1)
(7) Dynamical Balance Test
(8) Moment of Inertia Test
(9) Adjustment between Spacecraft and Launching Vehicle
(10) Magnetic Moment Test

C. *Computation of the Reliability of IPS*

Parts	λ_i	n_i	$n_i\lambda_i$
Transistor (low power)	20	145	2900
〃 (〃)	100	4	400
〃 (high power)	45	1	45
FET	100	14	1400
IC (analog)	50	17	850
〃 (〃)	250	2	500
〃 (logarithmic)	250	2	500
〃 (digital)	25	31	775
〃 (〃)	150	6	900
Diode (low power)	3	76	228
〃 (zener)	10	11	110
Resistor (constant)	2	594	1188
〃 (variable)	200	46	9200
Condensor (tantalum)	10	72	720
〃 (ceramic)	10	213	2130
〃 (mica)	10	109	1090
〃 (variable)	150	4	600
Coil	10	24	240
Transformer (signal)	10	51	510
Relay (latching)	70	2	140
Crystal	150	3	450
DEM connector (pin)	1	127	127
SMB connector	2	10	20
Soldering point	0.5	3969	1984.5
TOTAL	—	5407	27007.5

(1) λ (failure rate) of each element is estimated under the condition that the derating ratio is 0.25 at 30°C and the confidence level is 60%.

(2) In the case of the spacecraft REXS, each observational instrument should be designed to have its reliability more than 0.948, in order to keep the reliability of the whole spacecraft system more than 0.9.

D. Calibration Coefficients

All the values used here are expressed by the floating points data of FORTRAN IV language; E indicates the single precision exponential.

(I) The temperature of pre-amplfier is measured with the house keeping instrument (HK), and the temperature (T°C) versus the output decimal value (N_0) is given in Fig. D-1. This calibration characteristics can be approximated by a following polynomial function selecting C_n values to make the best fit to the measured function as

$$T=\sum_{n-1}^{6} C_n N^{n-1}$$

where

$$\begin{aligned} C_1 &= -0.3907810E+02,\\ C_2 &= +0.4135541E+00,\\ C_3 &= +0.7335699E-03,\\ C_4 &= +0.7939580E-05,\\ C_5 &= +0.3150700E-07,\\ C_6 &= +0.3742000E-10. \end{aligned}$$

and

(II) The coefficients C_n for the temperature correction of Fh_1, Lh_1, and Lh_3 that are given in eq. (5.19), are:

	Fh_1	Lh_2	Lh_3
C_1	0.5611062E+00	−0.8008370E+00	0.1700000E−02
C_2	−0.5955836E+00	−0.4531361E+00	−0.1022510E+01
C_3	−0.2533402E−03	−0.3754487E−01	−0.4787000E−01
C_4	0.6972036E−03	0.3764375E−04	−0.2730000E−03
C_5			0.7875000E−04

As for the temperature correction of Fh_2, the following step function is used.

$$N_T=\begin{cases} N_0 & \text{for } T<21^\circ \\ N_0+6.0 & \text{for } T\geq 21^\circ \end{cases}$$

(III) The coefficients C_n for the calibration of Lh_1 and Lh_3 in eq. (5.21), are:

	Lh_1	Lh_3
C_1	0.48436849E+00	−0.13788950E+01
C_2	0.31760218E−02	0.53816587E−01
C_3	0.66991901E−04	−0.39311962E−03
C_4	−0.31419130E−06	0.14225626E−05
C_5	0.71353541E−09	−0.17612791E−08

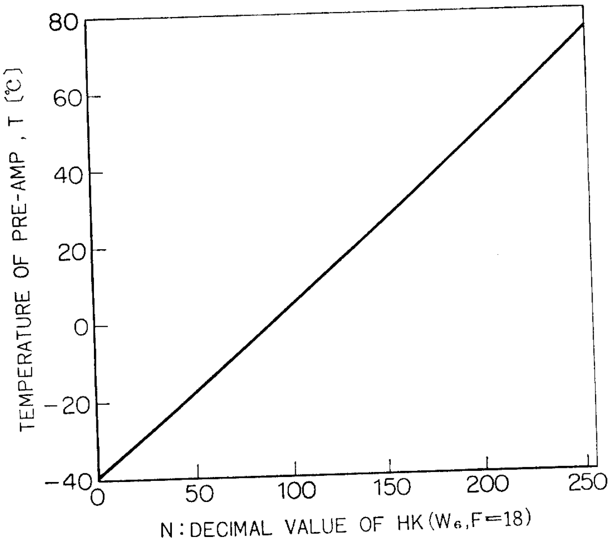

FIG. D-1. Output decimal values versus temperature in pre-amplifier of IPS.

(IV) The coefficients C_n for the calibration of $Ll_{1\sim 3}$ in eq. (5.25), are:

	Ll_1	Ll_2	Ll_3
C_1	0.79018545E+00	0.11921958E+01	0.11488734E+01
C_2	0.27178132E+01	0.87813898E+00	0.10426516E+01
C_3	−0.21166261E+01	−0.21107455E+00	−0.43391613E+00
C_4	0.90672745E+00	0.84797601E−01	0.18222577E+00
C_5	−0.12740256E+00	−0.37502374E−02	−0.16249358E−01

(V) The coefficients C_n for the V_0 and V_1 in eq. (5.24), and V_1 and N_0 in eq. (5.23), are:

	V_0 and V_1	V_1 and N_0
C_1	−0.13509059E−01	−0.6711605E−01
C_2	0.10659802E+01	0.1201142E−01
C_3	0.47236235E−02	0.3793714E−06

REFERENCES

[*1*] Oya, H: *Small Rocket Instrumentation Techniques,* North-Holland Pub. Co. Amsterdam, 36 (1969).

[*2*] Oya, H. and T. Obayashi: Space Research VII, Vol. I, North-Holland, Amsterdam, 180 (1967).

[*3*] Miyazaki, S., K. Hirao, Y. Aono, K. Takayama, H. Ikegami and T. Ichimiya: Rept. Ionos. Space Res. Japan, **19**, 243 (1965).

[*4*] Oya, H. and T. Obayashi: Rept. Ionos. Space Res. Japan, **21**, No. 1/2, 1 (1967).

[*5*] Oya, H. and T. Obayashi: Rept. Ionos. Space Res. Japan, **21**, No. 1/2, 9 (1967).

[*6*] Oya, H.: J. Geomag Geoele., **19**, No. 4, 267 (1967).

[*7*] Harp, R. S. and F. W. Crawford: Microwave Lb. Tech. Rept., Stanford Univ., Stanford, Calif., No. AF 33 (616)-8121 (1964).

[*8*] Uramoto, J., H. Ikegami, and K. Takayama: Res. Rept. Inst. Plasma Phys., Nagoya Univ., Japan, No. IPPJ-15 (1963).

[*9*] Dote, T. and T. Ichimiya: Proc. IEEE, **51**, 480 (1963).

[*10*] Fejer, J. A.: Radio Sci., **68D**, 1171 (1964).

[*11*] Oya, H.: Rept. Ionos. Space Res. Japan, **19**, No. 3, 243 (1965).

[*12*] Balmain, K. G.: IEEE Trans. AP-12, 605 (1964).

[*13*] Oya, H.: Planet. Space Sci., **18**, 793 (1970).

[*14*] Oya, H. Rept. Ionos. Space Res. Japan, **22**, No. 1/2, 119 (1968).

[*15*] Ejiri, M., H. Oya, and T. Obayashi: Rept Ionos. Space Res. Japan, **22**, No. 3, 201 (1968).

[*16*] Oya, H. and T. Obayashi: Space Research VIII, North-Holland, Amsterdam, 332 (1968).

[*17*] Simon, A.: Phys. Fluis, **6**, 382 (1963).

[*18*] Tsuda, T., T. Sato, and K-I. Maeda: Radio Sci., **1**, 212 (1966).

[*19*] Obayashi, T. and M. Ejiri: Space Research XI, Akademie Verlag, Berlin, 1067 (1971).

[*20*] Heller, G. B.: ed., *Thermosphysics and temperature control of spacecraft and entry vehicles,* Academic Press, N.Y. (1966).

[*21*] Hrycak, P.: Astro. Aero. Eng., 44 (1963).

[*22*] Hammerdinger, L. H.: J. Spacecraft, **1**, 477 (1964).

[*23*] Millard, J. P. and C. B. Neel: AIAA Journal, **3**, 1317 (1963).

[*24*] Gordon, G. D.: Rev. Sci. Inst., **31**, 1204 (1960).

[*25*] Hoke, M. G.: AIAA Journal, **3**, 947 (1965).

[*26*] Charnes, A. and S. Raynor: ARS Journal, 479 (1960).

[*27*] John, J. E. A. and W. F. Hardgrove: J. Spacecraft, **3**, 427 (1966).

[*28*] Tominaga, G., K. Hirao, T. Ito and C. Hayashi: Le Vide, **132**, 355 (1967).

[*29*] Oya, H.: GSFC X-615-69-272 (1969).

[*30*] Smith, R. L. and N. Brice: J. Geophys. Res., **69**, No. 23, 5029 (1964).

[*31*] Miodnosky, R. F. and O. K. Garriott: Proc. of the International Conference on the Ionosphere, Inst. Phys. and Phys. Soc., London, 484 (1962).

[*32*] Kozai, Y.: Astronomical J., **64**, No. 9, 367 (1959).

[*33*] Escobal, P. R.: *Methods of Orbit Determination,* John Wiley & Sons Inc., N.Y. (1965).

[*34*] Matsushita, S., and W. H. Campbell: *Physics of Geomagnetic Phenomena,* Akademic Press, N.Y. (1967).

[*35*] Cain, J. C. and R. E. Sweeney: J. Geophys. Res., **75**, No. 22, 4360 (1970).

[*36*] *Results of Experiment of Mu-4S-4 and Denpa (1972-064A),* Inst Space Aeronaut. Sci., Univ. Tokyo, Oct. (1972).

[*37*] Aoyama, I. and F. Toyama: Private Communication.

[*38*] Oya, H.: GSFC X-615-69-272 (1969).

[*39*] Angerami, J. J. and J. O. Thomas: J. Geophys. Res., **69** No. 21, 4537 (1964).

[*40*] Bauer, S. J.: Proc. IEEE, **57**, No. 6, 1114 (1969).

[*41*] Eviatar, A., A. M. Lenchek, and S. F. Singer: Phys. Fluids, **7**, No. 11, 1775 (1964).

[*42*] Carpenter, D. L.: J. Geophys. Res., **68**, No. 6, 1675 (1963).

[*43*] Angerami, J. J. and D. L. Carpenter: J. Geophys. Res., **71**, No. 3,711 (1966).

[*44*] Yonezawa, T. and H. Takahashi: J. Radio Res. Lab. Japan, **7**, No. 32, 335 (1960).

[*45*] Chandra, S.: J. Geophys. Res., **68**, No. 7, 1973 (1963).

[*46*] Solar-Geophysical Data (Prompt Report) No. 341-PART 1, Published by National Geophys. Solar-Terr. Data Center, Boulder, Colorado, USA (1973).

[*47*] Lyon, A. J. and L. Thomas: J. Atmosph. Terr. Phys., **25**, 373 (1963).

[*48*] Lockwood, G. E. K. and G. L. Nelms: J. Atmosph. Terr. Phys., **26**, No. 5,569 (1964).

[*49*] King, J. W., P. A. Smith, D. Eccles, G. F. Fooks and H. Helm: Proc. Roy. Soc. London, Ser. A*281*, No. 1381, 464 (1964).

[*50*] Chan, K. L.: Radio Sci., **1**, No. 10, 1158 (1966).

[*51*] Jackson, J. E.: Proc. IE, **57**, No. 6, 960 (1969).

[52] Chandra, S. and R. A. Goldberg: J. Geophys. Res., **69**, No. 15, 3187 (1964).